University of Zagreb

FACULTY OF SCIENCE
DEPARTMENT OF PHYSICS

Andreo Crnjac

INFLUENCE OF RADIATION AND HIGH TEMPERATURES ON ELECTRONIC PROPERTIES OF DIAMOND DETECTORS

DOCTORAL THESIS

Zagreb, 2022

University of Zagreb

FACULTY OF SCIENCE
DEPARTMENT OF PHYSICS

Andreo Crnjac

INFLUENCE OF RADIATION AND HIGH TEMPERATURES ON ELECTRONIC PROPERTIES OF DIAMOND DETECTORS

DOCTORAL THESIS

Supervisor: Dr. Milko Jakšić, F. C. A.

Zagreb, 2022

Sveučilište u Zagrebu

PRIRODOSLOVNO - MATEMATIČKI FAKULTET
FIZIČKI ODSJEK

Andreo Crnjac

UTJECAJ ZRAČENJA I VISOKIH TEMPERATURA NA ELEKTRONIČKA SVOJSTVA DIJAMANTNIH DETEKTORA

DOKTORSKI RAD

Mentor: akademik Milko Jakšić

Zagreb, 2022.

About the Supervisor

Milko Jakšić is a senior scientist at the Experimental physics division of the Ruđer Bošković Institute (RBI), Zagreb. During the last twenty five years he is leading the Laboratory for ion beam interactions, that operates accelerator infrastructure based on two electrostatic tandem ion beam accelerators. A wide range of experimental end stations are dedicated to ion beam analysis and ion beam materials modification applications. Currently, these are accessible internationally through different contracts and agreements with IAEA, EU projects and CERIC-ERIC consortium. The main research field of Milko Jakšić is development and applications of ion beam analysis as well as materials modification techniques based on MeV ion beams. He has published more than 250 research papers, cited more than 3000 times. His current specific interests include development of techniques using focussed ion beams, in particular those based on single ions including deterministic ion implantation. Among them it is also an IBIC – ion beam induced charge, technique for detector characterisation, through which applications RBI group became widely recognized. As a conference chair or a co-chair, he organized several most important international conferences in the field of ion beam applications and has also been a leader or associate of many EU and IAEA funded projects. He was mentoring 3 PhD students, more than 10 master students and in a number of occasions he supervised foreign postdocts and IAEA trainees. Since 2016, he is also a member of Croatian Academy of Sciences and Arts.

Acknowledgments

Abstract

Due to its ultra-wide bandgap, diamond is a material that offers a unique combination of excellent electrical, mechanical and thermal properties. Contrary to silicon, the operation of diamond-based radiation detectors should thus be possible under specific harsh conditions. In this work, hardness against temperature and radiation damage was investigated with two custom-designed thermally resilient diamond detectors. High purity single crystal diamond samples were used, with tungsten electrodes deposited on the opposing crystal faces. The operation of diamond as a radiation detector was investigated by exposure to fast ions in the MeV energy range, focused on a micrometer spot with the ion microprobe setup. By changing the ion energy and mass, the penetration depth or ionization density can be modified. These capabilities provide information about the interaction volume between the radiation particles and the device, which was exploited in two experimental scenarios: to probe the electronic properties by inducing ionization in the detector (probing ions), or to deposit the radiation damage by exposure to a higher ion dose (damaging ions). The analysis of the induced signal gives us the possibility to extract important parameters related to both the macroscopic detector performance, and the fundamental semiconductor properties of the diamond material used. Charge transport at elevated temperatures was characterized by measuring charge collection efficiency, mobility-lifetime product and drift time of electrons and holes, using both charge- and current-sensitive pulse-processing electronics. Testing the detector for nuclear spectroscopy operation revealed a highest operating temperature of 720 K, at which the energy resolution and collection efficiency of the detector remained virtually unaffected by thermal effects. It was also found that the radiation hardness, after deposition of the radiation damage with 5 MeV protons, deteriorates with elevating temperature. However, the decrease is stopped at temperatures above 660 K, which can be attributed to the beneficial mechanism of thermally induced detrapping of charge carriers. Analysis of the time evolution of the transient charge signal in the detector provided a framework to extract the energy levels of the responsible deep traps. These results are particularly important for the development and new applications of diamond radiation detectors in high-temperature and high-radiation conditions. Finally, an additional investigation was performed to understand the influence of the space-charge-limited regime on the charge carrier dynamics. It was demonstrated that exposure to elevated temperatures led to depolarization of the detector, whereupon the adverse effects on the charge transport were mitigated and collection efficiency was restored.

Keywords: diamond, detector, charge transport, ion beam, high temperature, radiation damage

Prošireni sažetak

Dijamant je poluvodički materijal koji, zbog ultra-širokog zabranjenog pojasa, nudi jedinstvenu kombinaciju izvrsnih električnih, mehaničkih i termalnih svojstava. Dijamantni kristali visoke čistoće se mogu dobiti procesom umjetne sinteze u laboratorijskim reaktorima, ponajprije procesom kemijskog taloženja iz parne faze (engl. *Chemical Vapour Deposition - CVD*). Tehnološki razvoj ove metode u zadnjih 20 godina je doveo do široke dostupnosti i dobre kontrole kvalitete uzoraka. To je otvorilo vrata za masovniju uporabu dijamanta u elektroničkim uređajima, od kojeg su za ovaj rad zanimljivi dijamantni detektori zračenja.

Dijamant bi trebao zadržati svoja intrinzična elektronička svojstva u specifičnim surovim uvjetima gdje bi korištenje silicija, kao poluvodiča uskog zabranjenog pojasa, bilo nemoguće. U ovom radu je testiran utjecaj visokih temperatura i ionizirajućeg zračenja na dijamant, korištenjem dva detektora s prilagođenim dizajnom razvijenim za toplinsku-otpornost pri radu. Detektori su bazirani na dijamantnim kristalima različite debljine (500 μm i 65 μm) gdje su na suprotne stranice kristala deponirane elektrode od volframa. Na spoju dijamanta i volframa je stvoren omski kontakt koji omogućuje uspostavu napona i očitanje signala kroz električne kontakte. Nakon primjene električnog polja, volumen između elektroda postaje osjetljiv na zračenje. Čestice zračenja ioniziraju dijamant i stvaraju nosioce naboja koji nadalje svojim kretanjem u polju induciraju izlazni signal na elektrodama. Proučavanjem svojstava tog signala mogu se ekstrahirati razni parametri vezani za detekciju zračenja (primjerice energija deponirana prilikom interakcije) kao i fundamentalna poluvodička svojstva samog dijamanta.

Glavnina eksperimentalnih tehnika korištenih u ovom radu je bazirana na ionskim mikrosnopovima MeV-skih energija, koji su prostorno fokusirani magnetskim poljima, uporabom tzv. ionske mikroprobe u akceleratorskom postrojenju Instituta Ruđer Bošković. Korištenje fokusiranog ionskog snopa, zajedno s mogućnošću promjene dubine prodora korištenjem iona različite mase i energije, pruža preciznu informaciju o interakciji iona s poluvodičem na mikrometarskoj skali koja se može kontrolirati prilikom eksperimenta. Ove funkcionalnosti su iskorištene u dva različita scenarija: za karakterizaciju svojstava samog detektora različitim tehnikama analize ionskim snopom, kao i za deponiranje defekata u kristalnu strukturu ozračivanjem velikim dozama iona. U posljednjem slučaju ione ne smatramo česticama za ispitivanje, već za oštećivanje poluvodiča. Detektori su bili izloženi ionskim snopovima i visokim temperaturama u vakumskoj komori ionske mikroprobe, što je zahtijevalo tehničku nadogradnju komore, kao i razvoj specifičnih eksperimentalnih procedura za potrebe ovog rada.

Signal induciran u detektoru je procesiran korištenjem nabojno- i strujno-osjetljive elektronike da bi se iz njegovih svojstava odredili različiti parametri, kao što su: učinkovitost prikupljanja naboja, produkt vremena života i mobilnosti ($\mu\tau$) nosioca naboja, driftno vrijeme itd. Ova svojstva su izmjerena i za elektrone i za šupljine u širokom rasponu povišenih temperatura.

Pokazalo se da mobilnost šupljina opada brže nego za elektrone s porastom temperature. Uzrok pada mobilnosti leži u povećanoj vjerojatnosti raspršenja na kristalnoj rešetci ili defektima u rešetci. Dobiveni rezultati su uspoređeni s ranijim mjerenjima dostupnim u literaturi. Nadalje, izmjerena je ovisnost $\mu\tau$ parametra o temperaturi, te je uočena znatna razlika u ponašanju dvije vrste nosioca. Uzrok ovakvog rezultata nije bilo moguće jednoznačno povezati s jednostavnom fizikalnom zakonitosti, što indicira da je potrebno dublje razumijevanje pozadinskih mehanizama koji određuju svojstva transporta naboja u dijamantu. Ovdje znatnu važnost imaju defekti u kristalnoj strukturi, koji pri skupljanju naboja postaju centri uhvata (zamke) nosioca naboja te utječu na svojstva nabojnog transporta. Čak i umjetni dijamanti visoke kvalitete, kakvi su korišteni u ovom radu, imaju veće razine nečistoća u odnosu na one koje su standardno prisutne u siliciju.

Neželjeni efekt koji nastaje kao posljedica uhvata veće količine nosioca u zamkama je stvaranje prostorne raspodjele naboja između elektroda (polarizacija), koja dovodi do zasjenjenja vanjskog električnog polja i narušavanja svojstava nabojnog transporta. Snažan utjecaj polarizacije je zamijećen pri radu debljeg (500 μm) detektora, gdje, zbog veće udaljenosti među elektrodama, efekti zasjenjenja lakše dolaze do izražaja. Proučavanjem prijelazne (tranzijentne) strukture strujnog signala zaključeno je da se polarizacija javila zbog nakupljanja šupljina, i to uniformno kroz cijeli volumen dijamanta. No, grijanje detektora na blago povišene temperature (oko 370 K) je dovelo do termalno inducirane depolarizacije, što se moglo kvantificirati iz promjena induciranog signala koje su upućivale na oporavak transportnih svojstava šupljina. Također, tranzijentni signali su pokazali da i pri povišenim temperaturama i stvaranju polarizacije, brzina drifta elektrona i šupljina nije znatno narušena i ostaje velika (u usporedbi sa silicijem). Ovo je osobito korisno u primjenama za brzo brojanje ili vremensko razlučivanje u eksperimentima visokog protoka čestica.

Dio mjerenja je izveden s namjerom karakteriziranja parametara bitnih za primjene detektora u eksperimentima nuklearne fizike, kao što su nuklearna spektroskopija. Skupljanje zadovoljavajuće statistike događaja induciranih zračenjem može zahtijevati dugo vrijeme rada detektora. Stoga se za rad detektora koji je izložen povišenim temperaturama treba testirati stabilnost performansi na dužim vremenskim skalama. Protoni energije 2 MeV su korišteni kao ulazne čestice koje se u potpunosti zaustavljaju i deponiraju cjelokupnu energiju unutar detektora. Testirani su parametri učinkovitosti skupljanja naboja kao i energijska razlučivost. Postignuta temperatura od 720 K, do koje su neželjeni termalni efekti na svojstva detekcije ostali gotovo zanemarivi, je bila najviša prijavljena u znanstvenoj literaturi u trenutku pisanja ovog rada. Razlučivost od 2% (40 keV) i učinkovitost sakupljanja naboja od oko 95% se mogu smatrati iznimno dobrim za mnoge primjene. Detektor je također bio izložen zračenju α-česticama (iz kalibriranog α-izvora s tri radionuklida poznatih energija). Mjerenja energi-

jske spektroskopije s alfa česticama na visokim temperaturama su već objavljena u nekoliko radova prethodnih godina pa je dana direktna usporedba s tim rezultatima. Pri usporedbama se pokazalo da je važno uzeti u obzir različitu debljinu korištenog dijamanta, kao i karakteristike tehničkih izvedbi samog detektora koje se znatno razlikuju u različitim radovima. Posebice je zanimljiv rezultat da debljina dijamanta ima znatan utjecaj na svojstva transport naboja, s obzirom da postoji sistematska tendencija da deblji kristali imaju niže maksimalne temperature prije sloma elektroničkih svojstava. Isto je uočeno u ovom radu.

Za testiranje otpornosti na zračenje detektor je prvo izložen velikim dozama protona energije 5 MeV-a, koji u potpunosti penetriraju volumen među elektrodama, i ostavljaju pritom uniformnu raspodjelu primarnih defekata (intersticija i vakancija) u ozračenom dijelu. Svojstva induciranog signala u oštećenim i neoštećenim područjima su direktno uspoređena, iz čega se uočilo da količina sakupljenog naboja u oštećenom dijamantu opada sa temperaturom. Ipak ovaj trend gdje temperatura negativno utječe na otpornost na zračenje je zaustavljen pri oko 660 K, zbog efekta otpuštanja naboja iz zamki. Te zamke su nastale zbog oštećivanja (unosa defekata) ionskim snopom. Nosioci naboja inducirani u područjima ispunjenim tim zamkama će prilikom kretanja prema elektrodama imati veliku vjerojatnost uhvata. Nakon uhvata elektroni ili šupljine mogu biti otpušteni ukoliko prime energiju grijanjem (termalno inducirani otpust nosioca naboja). Stoga će vremenska struktura nabojnog signala znatno ovisiti o temperaturi, posebice za one temperature oko temperature aktivacije zamke. Iz induciranog signala evaluirana je vremenska konstanta koja odgovara prosječnom vremenu uhvata nosioca naboja na različitim temperaturama. Korištenjem Shockley-Read-Hall statistike, iz temperaturne ovisnosti vremenske konstante se pronašao energijski položaj duboke zamke odgovorne za uhvat naboja. Takve zamke se nalaze daleko od rubova vodljivog i valentnog pojasa i teško otpuštaju zarobljene nosioce naboja. Rezultat je uspoređen sa sličnim rezultatima u prijašnjim znanstvenim radovima, no nije bilo moguće jednoznačno odrediti kristalnu strukturu defekta koji bi odgovarao tom dubokom nivou. Ipak moglo se zaključiti da je defekt bio prisutan samo u dijelovima izloženim visokim dozama zračenja, ali ne i u neoštećenom dijamantu, te da je zarobljivao i otpuštao šupljine ali ne i elektrone. Njegova temperaturna aktivacija omogućava bolji rad detektora na visokim temperaturama.

Svi ovi rezultati mogu biti značajni za razvoj i nove primjene dijamantnih detektora namijenjenih radu o uvjetima povišene temperature i zračenja, kao i za bolje razumijevanje ograničenja koje kvaliteta kristala nameće na poluvodička svojstva dijamanta kao materijala za nove generacije elektroničkih uređaja.

Ključne riječi: dijamant, detektor, prijenos naboja, ionski snop, visoke temperature, oštećenja uzrokovana zračenjem

Contents

1. Introduction

Motivation

Going beyond the limits of silicon, by pushing the limits of diamond. This could be a brief summary of our motivation for this work. Silicon technology is by far the most advanced in wafer production, doping, structure fabrication, etc. However, wide band-gap semiconductor materials such as diamond, silicon carbide (SiC), and boron nitride (BN) offer material properties that add momentum in development of new electronic and optoelectronic devices. For radiation detection, diamond has been actively used and investigated for at least 70 years. The first diamond-based detectors used natural diamond crystals (excavated from mines). Later, the era of artificially grown crystals came, allowing better quality control and minimizing sample-to-sample variation. From the early 2000s, technological advances in MWPACVD (microwave plasma-assisted chemical vapor deposition) growth technology generated a leap toward widespread availability of high-quality diamonds, which have since become the standard for detector applications. Some important properties of diamond and silicon, relevant for their application as semiconductor radiation detectors, are summarized in the table 1.1.

High-quality single-crystal CVD diamond has been used for a variety of detection scenarios over the past 20 years: charged particle, X-ray, γ-ray, UV, and neutron detection; multi-pixel particle tracking for CERN; 3D electric field structure designs; radiation therapy monitoring; microdosimetry, etc. Furthermore, being an extremely wide band-gap semiconductor, diamond

Table 1.1: List of some basic properties of diamond and silicon at room temperature. [1, 2, 3]

Property	Si	Diamond
Mass density [g/cm^3]	2.33	3.52
Band-gap [eV]	1.12	5.47
Intrinsic resistivity [Ω cm]	2.3×10^5	$> 10^{15}$
Breakdown field [MV/cm]	0.3	10
Pair creation energy [eV]	3.6	13
Saturation drift velocity [cm/s]	1×10^7	$1.2 - 2.7 \times 10^7$

seemed to be a material of choice for high-temperature electronic devices, as it's intrinsic electronic properties should remain excellent with rising temperature. Namely, the thermal promotion of electrons to the conduction band is negligible even at 1000 K in intrinsic diamond, from which it can be estimated that the intrinsic carrier concentration in diamond at that temperature remains lower than that of silicon at room temperature. Taking this into account, together with promising results in terms of tolerance to radiation damage, CVD diamond is certainly a prominent candidate for a growing research in radiation detection operation in high-temperature and high-radiation conditions. Specifically, in recent years, there has been an increasing number of reports on diamond detectors performance at elevated temperatures. However, there is limited information and studies on operation in both harsh radiation and temperature environment. Two main reasons to investigate diamond in such conditions are: a) testing the semiconductor properties of high purity CVD diamond, and b) developing and improving radiation detection systems for specific, harsh environment, applications. One such application is the use of diamond detectors in nuclear fusion reactors for neutron or charged particles diagnostics.

In this work, high purity single-crystal CVD diamond samples, supplied by *Element Six ltd.*, were used for assembly of two particle detectors. A thin 65 μm diamond crystal was used for one of the devices, and a thick 500 μm crystal was used for the other. The electrodes were deposited in a parallel-plate geometry. To ensure that there would be no adverse thermal effects on the signal-processing components located in close proximity to the heat source, custom-made, thermally resilient, components were used for the mounting stage of the detector. MeV ion microbeam setup at accelerator facility of the Ruđer Bošković Institute was used to expose the detectors both to probing and damaging ion beams. Vacuum chamber of the ion microbeam setup was upgraded with an in-house developed heating stage to enable high-temperature device testing.

Several ion beam-based techniques were used in this work to characterize diamond detectors. The employed techniques allowed us to quantify the influence of radiation damage and temperature on both the fundamental semiconductor properties of the diamond material, and the macroscopic detector performance. After injection of charge carriers by probing ion beam, charge transport properties can be studied from the signal induced at detector electrodes: drift time of charge carriers, mobility-lifetime product, detrapping time from deep trap levels, charge collection efficiency and energy resolution. Parameters of charge transport were measured and compared for both electrons and holes wherever possible.

The influence of temperature on the polarization effect is also investigated and discussed. A section is devoted to modeling the evolution of polarization with the accumulation of trapped charge, and relates it to the observed experimental behavior. Polarization-related phenomena are one of the major challenges in the development of diamond radiation detectors.

The specific capabilities of ion microbeam setup were used to selectively expose only small

sections of a detector volume to high ion beam fluence, for induction of radiation damage. The irradiated regions are chosen to be small enough, so that the overall device performance remains unaffected, and subsequent probing with microscopic spatial resolution allowing direct comparison properties of pristine and radiation-damaged diamond within the same sample. Influence of crystal quality is also reviewed on several points for a broader context.

In addition, when discussing the results, the observed effects have been related to the predictions of semiconductor theory or to previous investigations reported by various research groups. Only tentative understanding of some of the observations could be obtained within the scope of this work, indicating that a systematic characterization of charge transport in single-crystal CVD diamond remains a challenging and complex endeavor. However, the presented results will certainly be useful to various research communities related to diamond and radiation detection.

Outline

The thesis is organized as follows. Chapter 2 contains a brief overview of the diamond crystal and band structure, semiconductor properties at equilibrium for intrinsic diamond, thermal conductivity, and finally a section on the fabrication of CVD diamond crystals. The third chapter incorporates principles relevant to the use of diamond as a radiation detector - from the theory of charged particle interactions, to signal formation and defect related phenomena. Then, chapter 4 presents the experimental techniques that have been utilized in this study. The main focus is placed on the ion microprobe setup and the associated ion-beam methods used for detector characterization. A section of this chapter is devoted to the description of the development of experimental setup and procedures, tailored to the specific needs of radiation detection at elevated temperatures. Technological steps that have been achieved throughout the course of this work proved to be crucial for understanding and exceeding previous high-temperature limits for radiation detection, as well as overall development of detector characterization techniques in the framework of the ion microprobe setup.

Experimental results are given in chapters six and seven. First, the investigation of charge transport and collection performance for pristine, unirradiated, diamond is presented. Then, the influence of the radiation damage on detector properties is quantified through several parameters that are influenced by trapping effects. Effects of polarization are also discussed. Finally, chapter 7 summarizes the presented results and outlines main conclusions and prospects of future work on this topic.

2. CVD diamond

Diamond is a wide band-gap semiconductor. It has superior electronic, mechanical and thermal properties compared to narrow band-gap semiconductors, such as silicon. Some of these properties, which are particularly important for the purpose of this thesis, will be discussed in more detail in this chapter.

2.1 Crystal structure and band properties

Diamond crystal structure can be understood as two face-centered cubic (FCC) lattices, with the same lattice constant $a = 3.567$ Å, but displaced along the body diagonal by one-quarter of its length. This can be seen on the unit cell of diamond, Figure 2.1. Carbon atoms form strong
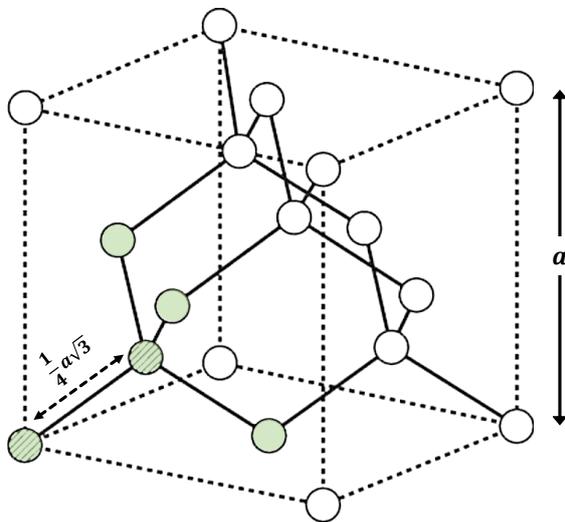
Figure 2.1: The unit cell of diamond crystal structure, with a lattice constant a. Two carbon atoms marked with pattern shading can be considered as base points of two interpenetrating FCC structures, displaced by a quarter of cell space diagonal. Five atoms that form a tetrahedral assembly are also highlighted with green shading. The carbon-carbon bonds are formed from overlap of sp^3 hybrid orbitals.

covalent bonds with four adjacent atoms. These four nearest neighbours lay at the corners of the symmetrical tetrahedron. Such geometry is dictated by hybridization of s and p states of valence electrons of carbon atoms, resulting in sp^3 hybrid orbitals. Each carbon atom has four sp^3 bonds that are symmetrically separated in space by an angle of 109.5°, thus forming tetrahedral assembly. Two neighbouring atoms are only 0.154 nm apart. This specific close-packing of atoms, called the diamond structure, results in the highest known atomic density of all materials, 1.76×10^{23} cm^{-3}. The bulk modulus is 4.4×10^{11} N/m^2, which is more than four

times higher than that of Si crystal.

Electronic band structure

The electronic properties of semiconductor materials are determined by the atomic structure. An electron bounded by an atom can occupy only discrete energy levels. In a crystal, an enormous number of atoms are combined into an ordered structure, a crystal lattice. As a result, electrons find themselves in a periodic potential. It can be demonstrated that for a such quantum-mechanical system, the allowed energy states are merged into quasi-continuous energy bands. A band of energy states in which an electron is bounded to an atom is called the valence band, while the states in which an electron is free to move are grouped in the conduction band. Between these bands lies an energy gap, the region of forbidden energy states.

If we consider a periodic potential, such that:

$$U(\vec{r}+\vec{a}) = U(\vec{r}), \tag{2.1}$$

Bloch theorem states that the wavefunction that is a solution of a Schrödinger equation of an electron moving in such a potential, satisfies the following condition:

$$\psi(\vec{r}+\vec{a}) = e^{i\vec{k}\cdot\vec{a}}\psi(\vec{r}), \tag{2.2}$$

or

$$\psi(\vec{r}) = e^{i\vec{k}\cdot\vec{r}}u(\vec{r}), \tag{2.3}$$

where $u(\vec{r}+\vec{a}) = u(\vec{r})$ is a periodic function, and $\vec{k}$ is the wave vector.
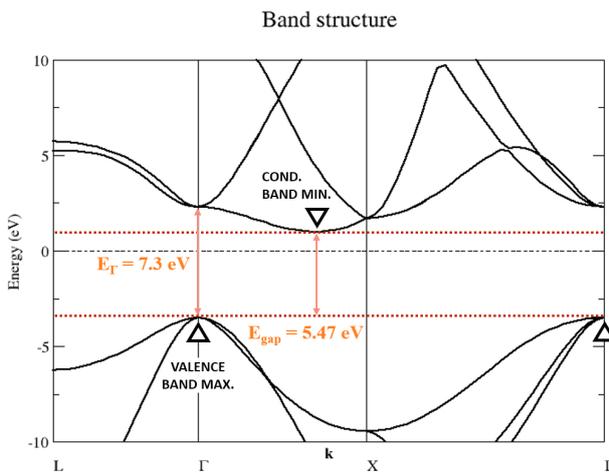
Figure 2.2: Band structure of diamond at room temperature, calculated using self-consistent Kohn-Sham density functional method. Open source SIESTA code [4] was used to produce the band structure plot, with the calculation which employs a basis set of strictly-localized atomic orbitals. Valence band maximum and conduction band minimum are marked with dashed lines. Direct and indirect band-gap values are also indicated.

In semiconductors, for each value of k, there are multiple solutions of the Schrödinger equation, whose eigenvalues $E(k)$ always lay inside valence or conduction band, with a range of forbidden energies (unavailable for electrons) formed between the bands. For the calculation of

allowed energy states as a function of k-vector value, we can employ density functional theory (DFT), where electron density in a material is approximated by a functional. E-k plot, or electronic band structure of diamond, is displayed in Figure 2.2. Points of high symmetry in the first Brilluion zone, L, Γ and X, are noted on the abscissa. At Γ point, the valence band reaches maximum (VBM) value. However, the conduction band minimum (CBM) is reached at a different point in k-space. Energy band-gap between these points is 5.47 eV, making diamond an ultra wide band-gap semiconductor. Electrons transitioning to the conduction state must "jump" over a rather large energy barrier. Furthermore, the fact that VBM and CBM are not overlapping in k-space makes diamond an indirect semiconductor. The conservation of momentum requires involvement of phonons during pair creation process in such semiconductors. Phonons transfer momentum to the crystal lattice.

Wide band-gap is at an origin of explaning many diamond's electronic properties, which will be especially important for the explanation of the performance in harsh environments of high-temperature and high-radiation that were explored in this work.

Effect of temperature on band-gap energy

Increased thermal energy in the crystal lattice results in larger amplitude of atomic vibrations. This affects the inter-atomic distance and deteriorates the bond strength. Consequently, the band-gap energy of most semiconductors tends to decrease with rising temperature.

This dependence is represented well by the Varshni's empirical expression [5]:

$$E_{gap}(T) = E_{gap}(0) - \frac{\alpha T^2}{T + \beta}, \qquad (2.4)$$

where α and β are fitting parameters, and $E_{gap}(0)$ represents the maximum value of the band-gap energy at 0 K temperature.

Figure 2.3 plots the results of nonlinear approximation, according to equation 2.4, to the experimental data $E_{gap}(T)$ for three semiconductors: GaAs, Si and Ge. Data obtained for natural diamond, published in 1964, indicate the similar thermal behavior [7] in diamond. According to these results, band-gap energy drops to 5.35 eV at 700 K. However, more recent and more reliable measurements on artificial CVD diamond samples are missing to confirm the exact temperature trend. Since there are no widely-accepted values for the temperature dependence of band-gap energy of diamond, fixed, room temperature, value will be used in this work, even for calculations at elevated temperatures. This is an approximation whose impact on the quality and interpretation of the measured values and parameters can be estimated as minimal.
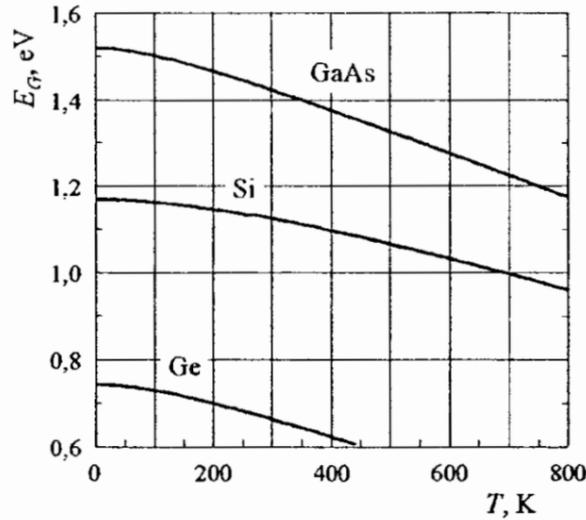
Figure 2.3: Band-gap energy dependence on temperature for GaAs, Si and Ge. Plotted functions are calculated as the best fit to experimental data to the equation 2.4. Reproduced from [6]. Actual, experimental temperature data points are omitted from the plot.

2.2   Charge carriers in semiconductors

2.2.1   Electron-hole pair creation

In a semiconductor, valence electrons can "jump" across the band-gap and move to the conduction band if they gain enough energy. This energy is usually transferred to the atoms and electrons through heat or radiation. After being released from the atom, the electrons leave behind a positively charged hole, and this process is called electron-hole pair (ehp) creation. The pair creation is shown schematically in the energy band diagram in Figure 2.4. The drift of conduction electrons and holes in an externally applied electric field is responsible for signal formation in semiconductors. Without an electric field, these charge carriers can still move randomly through the crystal lattice by diffusion.

The pair creation energy, E_{ehp}, is a constant of the material, that does not depend on the type and energy of the ionizing radiation [9]. E_{ehp} is always larger than the actual band-gap energy E_{gap}. Energy difference is lost on the excitation of lattice vibrations (phonons) [10]. The relationship between E_{ehp} and E_{gap} is shown for various semiconductor materials in Figure 2.5. A linear relation $E_{ehp} = A \cdot E_{gap} + B$ is observed, however, the experimental data are grouped in two branches that follow different linear dependencies. For example: Ge, Si and CdZnTe belong to a different branch, than SiC and diamond.

Let us consider ehp creation induced by the incident beam of ionizing radiation on a semiconductor. The number of created free ehp pairs is $N_{ehp} = E_{dep}/E_{ehp}$, where E_{dep} is the total energy deposited by the radiation particles. However, the charge generated in the detector will fluctuate due to the statistical nature of the ionization processes. If each pair creation event
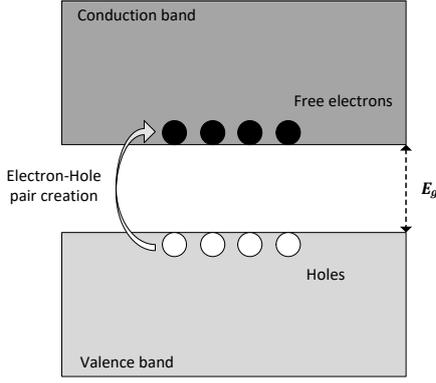
Figure 2.4: Mechanism of ehp creation in the semiconductor, depicted in the simplified energy band diagram.
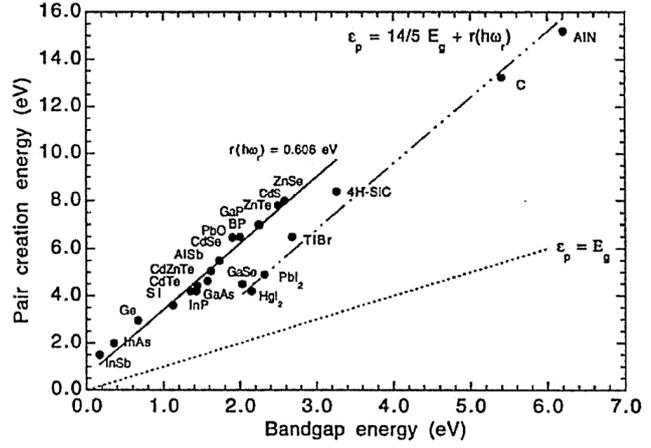
Figure 2.5: Average energy needed for ehp creation for semiconductors of different band-gap values [8].

was independent of the others, the variance in the generated signal would be given by a Poisson distribution. This is not the case when the ionizing radiation is completely absorbed in the sensitive volume of the detector. Then the ionization events are not truly independent, but are constrained by the energy conservation condition. This effect is accounted for by the Fano factor [11]. The intrinsic energy resolution of the semiconductor radiation detector, taking into account the variance in the statistics of ehp ionization events, will be:

$$\sigma_{intr} = \sqrt{F N_{ehp}}\,, \tag{2.5}$$

where the Fano factor F is $0 < F < 1$.

The measurement of this factor for diamond detectors is mainly limited by the incomplete charge collection efficiency, due to trapping related phenomena. Recent experiments by Shimaoka et al. [12] on high quality synthetic diamond using α-particles, found an averaged value of Fano factor for 3 detectors to be $F = 0.44$, and ehp creation energy $E_{ehp} = 13.1\,\mathrm{eV}$. Other authors have reported similar E_{ehp} values measured using different crystalline quality diamonds [1, 12, 13], with an average value of 13.05 eV. However, values as high as 16.1 eV [14] and 17.6 eV [15] have also been reported.

Regarding the Fano factor, more reliable and comprehensive experimental results are missing to draw conclusions on the exact value. Theoretical calculations predict F as low as 0.08 [16].

2.2.2 Intrinsic carrier concentration

An important characteristic of a semiconductor is the concentration of free carriers at a given temperature. This will influence leakage current of the device, so it is an important information for design of electronic devices like particle detectors. As described in the previous section, both

electrons and holes carry charge in the semiconductor material. Let us consider a semiconductor in the equilibrium, which means that there are no external forces, such as electric and magnetic fields or temperature gradients, acting on it.

Intrinsic semiconductor has no significant impurities or doping atoms in the crystal lattice. In other words, it is chemically very pure. In diamond, each carbon atom forms 4 covalent bonds with its nearest neighbours. When an impurity atom is introduced, it usually does not create the same number of covalent bonds, which results in either an excess or a deficiency of valence electrons. A large number of dopands induce imbalance between electrons and holes in the material. Doping is sometimes desired and intentionally introduced to modify electronic properties (intentionally doped semiconductors). For example, doping is used for forming *pn*-junctions in silicon based devices. In diamond radiation detectors, dopand atoms are undesired, as one needs high resistivity material, as close to intrinsic as possible.

For intrinsic semiconductor, number of conduction electrons and valence holes is equal, or $n_0 = p_0 = n_i$, where n_i denotes the intrinsic concentration of either conduction electrons or valence holes. At 0 K, all states in the conduction band are empty, and all states in the valence band are filled. At finite temperatures, some electrons will be introduced to the conduction band as governed by the statistics.

Intrinsic concentration n_i is given by [17, p. 114]:

$$n_i^2 = N_c N_v \exp\left(\frac{-E_{gap}}{kT}\right),\tag{2.6}$$

where k is the Boltzmann constant, T is the temperature, N_c is the effective density of states in the conduction band (for electrons), and N_v is the effective density of states in the valence band (for holes):

$$N_{c(v)} = 2\left(\frac{2\pi m_{e(h)}^* kT}{h^2}\right)^{3/2},\tag{2.7}$$

where $m_{e(h)}^*$ is the effective mass of electrons (holes), and h is the Planck's constant. Effective mass is generally a tensor, but it's value near CBM and VBM can be approximated as scalar. Theoretical and experimental evaluations of the carrier's effective mass in semiconductors often differ and are valid only in specific conditions, especially as effective mass depends on the relative movement of the carrier in respect to main crystal axes. Overview of the recent results for effective mass measurements in diamond can be found in [18].

We can exploit formula 2.6 to calculate the intrinsic concentration (or the number of free carriers) as a function of temperature, for different semiconductors. Let us do this for diamond and silicon. For the sake of simplicity let's assume, for both materials, $m_e^* = m_h^* = m_0$, where m_0 is the mass of free electron. Thus, the only differentiating factor in the calculation would be band gap energies, 5.47 eV (diamond), and 1.12 eV (Si), taken as constant for all temperatures.
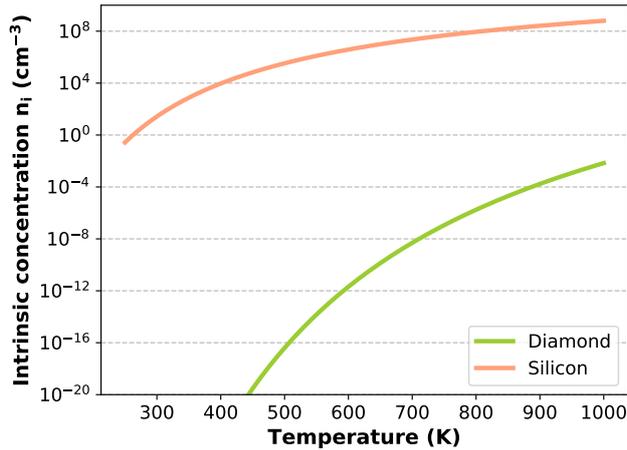
Figure 2.6: Intrinsic carrier concentration as a function of temperature, calculated according to eq. 2.6. $n_i(T)$ is displayed for diamond and silicon, with band-gap energy as only differentiating parameter. Note that y-scale is logarithmic. Number of thermally generated free carriers remains negligible in intrinsic diamond, even at 1000 K.

The results of the calculation are plotted in Figure 2.6. First, one can notice an enormous difference between the number of free carriers in diamond and silicon for all temperatures. Diamond is an extremely resistive semiconductor and has a negligible thermal generation of conductive electrons. Free charge carrier density in intrinsic diamond at 500 K can be estimated as $10^{-16}\,\mathrm{cm^{-3}}$. It increases to $10^{-2}\,\mathrm{cm^{-3}}$ at 1000 K, and this value still corresponds to practically zero free carriers in a typical device volume ($\leq 1\,\mathrm{cm^3}$). Therefore, these high temperatures should not impact noticeably electronic properties of perfect diamonds employed as radiation detectors. However, the calculation for the intrinsic diamond does not correspond with reported results measured in diamond-based detectors [19, 20, 21]. Higher leakage current than expected is reported, with varying orders of magnitude depending on the used crystal quality, indicating that free carrier generation will be enabled and dictated by the presence of impurities and their band-gap levels, which effectively lowers pair-creation energy. Crystal quality will surely have a strong impact on macroscopic properties and the performance of diamond radiation detection at high-temperature.

2.3   Thermal conductivity

Thermal energy in solids is most commonly transferred by free electrons or lattice vibrations. Free electrons efficiently conduct the thermal energy through the bulk. This form of heat conduction is prevalent in metals. Consequently, most metals are excellent heat conductors. In other crystalline solids (such as semiconductors), almost all heat is transferred by lattice vibrations, which tend to be less effective than free electron transport. However, in the case of diamond dissipation of heat by lattice vibration is quite effective. Synthetic diamond crystals have the highest thermal conductivity of any material [22]. This fact deserves a more detailed analysis.

The thermal conductivity is directly proportional to heat capacity, phonon velocity and phonon mean free path. In diamond, the phonon density of states extends to very high frequencies (high

Debye temperature), which translates into a high heat capacity. Phonon velocity is also high, transverse modes (sound waves) propagate at $v_{ph,l} > 10^6$ cm/s. Heat capacity and phonon velocity are high due to the small size of carbon atoms and their strong bonding in the diamond structure [23].

Third property, phonon free path, is mostly influenced by the purity and integrity of the crystal lattice, as phonon-defect scattering limits the flow of phonons. The investigation of the influence of point defect scattering dominates the available literature [24, 25, 26]. Consequently, values reported for heat conduction in high purity, synthetic diamond crystals, are even higher than those for previously investigated natural diamonds [22, 24].

Table 2.1: Thermal conductivity of several materials with good heat dissipation properties, measured at room temperature. Highest reported values for hexagonal BN (layered 2D material) and cubic BN have been referenced. Cubic BN has highest atomic density of all materials after diamond. All of the listed materials are appropriate for heat sink fabrication due to high thermal conductivity.

Material	Thermal conductivity [W/(cm K)]	Electrical conductivity
Synthetic diamond	>20	Semiconductor
SiC	2.8 - 4 [27]	Semiconductor
Hexagonal Boron-Nitride	<6 [28]	Insulator/Semicond.*
Cubic Boron-Nitride	<7.4 [29]	Insulator
Silver	4.2	Conductor
Copper	3.9	Conductor

Notes: * This material has a band-gap energy of ≈ 6 eV [30].

Table 2.1 lists some materials with high thermal conductivity at room temperature. Diamond, SiC and BN conduct heat with phonons, and even outperform some conventional heat-sink materials, like copper. Good thermal conductivity in a semiconductor is specifically important for high-frequency and power-electronic device applications, where heat dissipation is a mayor performance limit. For example, diamond-based JFET [31] was able to operate at temperatures up to 450 °C, due to combined ability to maintain good electronic properties, and dissipate heat effectively at temperatures higher than those available for silicon microelectronic devices.

For radiation detection, these diamond properties could be relevant in high temperature environments, like in a fusion reactor, or while being exposed to high intensity radiation beams (where beam-induced material heating could be quite intensive).

2.4 Crystal synthesis

Synthetic diamond crystals were first produced in the middle of the last century. The long development of the synthesis methods has led to the dramatic improvement in crystal quality and production scale. Today, there are many different techniques for artificial diamond synthesis. Both polycrystalline and homoepitaxial diamond material can be produced, depending on the needs of the user. In this limited overview of the recent progress in diamond production, the focus will be put on the synthesis of the highest-purity crystals that are used for electronic devices such as radiation detectors.

2.4.1 Natural and artificial diamonds

Use of natural diamonds in radiation detection dates as far back as 1940s and 1950s [32, 33, 34]. Natural diamonds were formed under extreme conditions in the Earth mantle, at $\sim$ GPa pressures, and temperatures higher than 1000 °C. Later, they were carried up to the surface by volcanic activity and were deposited in the rocks. The dominant impurity absorbed during natural diamond formation is nitrogen [35]. For this reason, diamond classification in gemology is usually based on nitrogen concentration (see Figure 2.7), as this influences the color and transparency of the crystal. Best available natural gems are classified as IIa, and contain only a few ppm[*] of nitrogen.
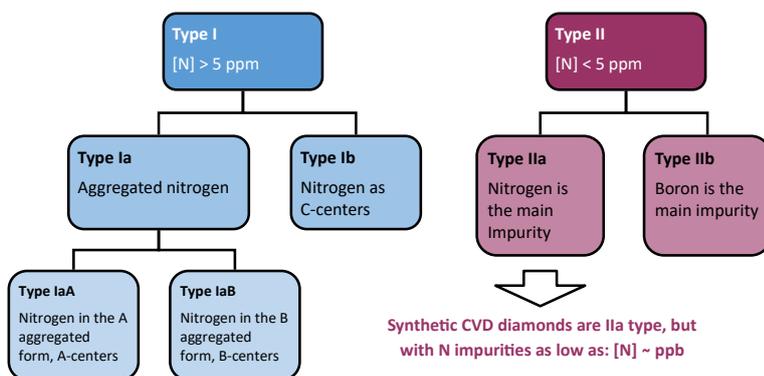
Figure 2.7: Commonly used diamond classification scheme according to their nitrogen concentration and predominant defect types. This scheme is mostly useful for naturally excavated gems, but not for synthetic diamonds, since their impurity contractions are usually very low, and tailored to specific needs in electronics, optics or machining.

Contaminants and other imperfections (e.g. bulk crystalline defects) in the crystal lattice will also determine electronic properties of the diamond. Electrically active defects exist as new energy levels in the previously forbidden energy gap. These levels can therefore have a significant impact in electrons ability to become conductive. It is crucial that the number of free charge carriers remains negligible in the diamond radiation detectors, as this affects their

---

[*]Atomic concentration can be expressed in this unit: ppm = parts per million, ppb = parts per billion

energy resolution, leakage current, and other macroscopic parameters. Contaminant control is impossible in natural crystals, and sample to sample quality usually varies significantly.

Maximum values of most common impurities (like nitrogen and boron) are usually guaranteed in process of synthetic diamond growth. Samples with [N] $\sim$ ppb are readily available on the market now. For this reason, artificially produced crystals have entirely replaced natural diamonds in electronic and optoelectronic diamond-based applications. However, state of the technology for diamond production is still nowhere near the scale and advancement of silicon semiconductor industry. This still influences the possibilities of wider employment of diamonds in cutting-edge and next-generation applications.

2.4.2 Chemical vapor deposition (CVD)

The most important diamond synthesis method is chemical vapor deposition (CVD). Samples used in this work were also produced using CVD process.

During CVD growth, carbon containing gas phase is passed around the solid substrate. H_2/CH_4 gas mixtures are usually used. Energy is transferred to the gas phase, which leads to activation of the gas molecules, and they dissolve into atomic hydrogen and CH_3 radicals. Presence of hydrogen seems to be crucial for plasma chemistry and growth properties [36, p. 16]. During this process gas temperature can reach up to 3000 K. The material is transferred to the substrate due to the temperature gradient (substrate is kept at lower temperatures). Here, chemical reactions occur which enable formation of small seeds of diamond structure (diamond nucleation) [35]. Nucleation chemistry is not fully understood, and deeper explanation of these reactions goes beyond the scope of this work. Shortly, diamond structure on the substrate is formed in non-equilibrium conditions, instead of carbon or diamond-like-carbon structures, which should be thermodynamically favoured. More details can be found in a large number of works on the synthetic diamond growth [35, 37, 38, 39].

Activation of gas phase can be achieved by different methods: hot filament, radio-frequency, microwaves, combustion flames, etc. Microwave plasma-assisted CVD (MWPACVD or PACVD) method has witnessed the most progress in recent decades allowing production of best quality crystals.

A schematic depiction of the MWPACVD reactor is shown in Figure 2.8. Microwaves are introduced into a reactor chamber that acts as a resonant cavity. The microwaves ignite gas phase in a ball-like plasma. The position and size of the plasma is determined mainly by the chamber geometry, and the plasma ball should be positioned a few centimeters above the substrate holder. The substrate is kept at a controlled temperature with a cooling stage, since diamond growth is only achieved at temperatures below 1100 K (above this, graphite growth becomes dominant). Nitrogen is usually introduced during crystal growth, as this promotes <100>
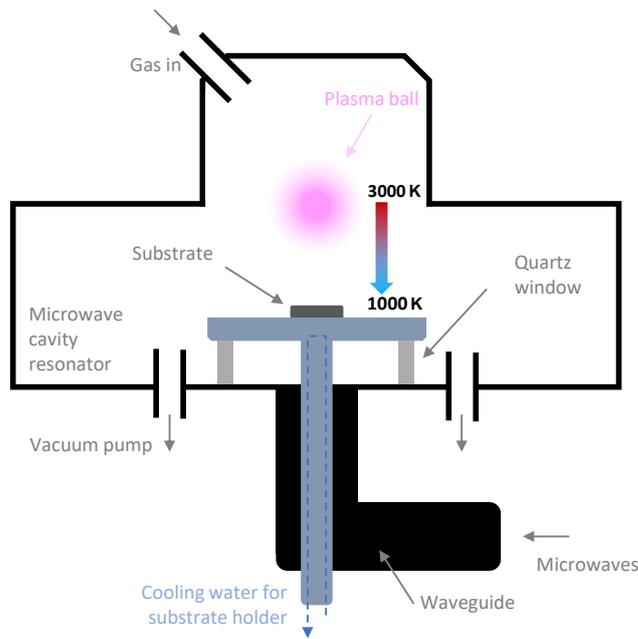
Figure 2.8: Schematic depiction of the microwave plasma-assisted diamond CVD reactor, of an ASTEX type. High power microwaves are introduced in the resonant cavity through a waveguide. Gas is ignited into a plasma above a substrate where diamond crystal nucleation and growth occurs. Illustration is based on [3, p. 46].

growth orientation and enables the growth rate at least 2-3 times higher [40, 41] as compared when no nitrogen is supplied.

Substrate on which a CVD process is started can be diamond or any material with diamond-like structure (for example, SiC substrate can be used [42]). The formation of diamond on non diamond substrate dominantly results in heteroepitaxial growth - crystalline mismatch between two structures. Due to the mismatch, crystal growth emerges from many nuclei sites with different crystal orientation located on the substrate surface. As growth continues crystal grains are formed from these nuclei and this results in the so-called pollycrystalline structure of the synthetic diamond [35]. Crystal grains significantly deteriorate diamond electronic properties as charge carriers are trapped on these bulk defects.

To achieve homoepitaxial single crystal CVD (sc-CVD) diamond growth (uniform crystal structure in the whole lattice), the base substrate must also be single crystal diamond also. Still, crystal defects can be induced during CVD process, mostly from nitrogen (or other impurities added in the gas phase) incorporation in the crystal lattice. For growth of high purity single crystals, several reactor conditions have to be followed: slow growth rate ($\sim \mu$m/h), low concentration of added nitrogen, high temperature uniformity from substrate to growth side. The last condition prevents realization of large high purity CVD diamonds - as crystal grows bigger, thermal stress is developed in the lattice from growth side (hot surface) to substrate side (where heat is dissipated on the holder). Stress induces structural defects and leads to the collapse of the crystalline order.

Excellent crystalline quality can be achieved with crystal growth when upper-mentioned condi-

tions are met. Nominally available nitrogen and boron concentration, resulting from the MW-PACVD high purity synthesis, on the order of $10^{14}\,\mathrm{cm}^{-3}$ are, however, still not satisfactory, and orders of magnitude improvement is desired. Therefore, the technological push on the diamond synthesis methods is far from over, as reliable production of bulk crystals remains challenging [43], and emerging scientific and commercial application require better control of point and extended defects, as well as bigger crystal sizes.

3. Diamond as a radiation detector

3.1 Ionizing radiation interaction with matter

During the penetration of ionizing radiation through the matter, different processes of interaction occur with atoms or their constituents (electrons and nuclei), leading to the energy loss, which is measured by the radiation detector. The nature of the interaction depends on the radiation type and its energy. There are charged particles (electrons, protons, ions, etc.), neutral particles (neutrons, etc.) and photons (gamma rays, X-rays, etc.). For each of these radiation sources successful theoretical description of the energy loss mechanisms already exists.

In the case of charged particles, the energy is lost mainly through the Coulomb interaction with atomic electrons. In this work, we will use fast ions of the MeV energy range that strongly ionize diamond detector volume, leading to the induction of a charge pulse. However, MeV ions can also create defects in the diamond crystal structure. Therefore, a brief summary of both electronic stopping power (responsible for energy transfer to atomic electrons) and nuclear stopping power (responsible for energy transfer to atomic nuclei, resulting in the production of radiation damage) of MeV ions will be given.

3.1.1 Stopping power of charged particles

Electronic energy loss

The energy loss of heavy charged particles occurs primarily through electromagnetic interactions with orbital electrons of the material. Calculations by Bethe and Bloch [44, 45] lead to widely accepted formula for electronic stopping power of charged particles in matter. The expression for energy loss per depth, for a specific target density, can be approximated as:

$$-\frac{dE}{dx} = KZ_1^2\frac{Z_2}{A}\left[\frac{1}{2}\ln\left(\frac{2m_ec^2\beta^2\gamma^2T_{\max}}{I^2}\right) - \beta^2 - \frac{\delta}{2}\right], \tag{3.1}$$

where $K = 4\pi N_A r_e^2 m_e c^2$, m_e and r_e are mass and classical radius of an electron, A and Z_2 are the target atomic mass and number, Z_1 is charge of the projectile, $T_{\max}$ is the maximum of kinetic energy transfer to a free electron during an interaction. Velocity of the radiation particle

is contained in the relativistic factor $\beta = v/c$, and $\gamma = 1/\sqrt{1-\beta^2}$. I is the average electron excitation energy, and it can be approximated as $I \cong 10Z_2$ eV [46]. δ represents a so called density correction, which becomes more important for relativistic energies.

Bethe-Bloch formula generally works well as long as the ion velocity is sufficiently high as compared to that of the inner shell electrons (and they can be considered as static). However, the formula is not valid for too high ion energies, when additional relativistic corrections need to be added to the expression [47].

At non-relativistic energies, β is very small, and the electronic stopping power is dominated by the $1/\beta^2$ term. In this regime the energy loss decreases with rising ion energy. At near-relativistic energies $\ln(\beta\gamma)$ is dominating, and the energy loss is growing slightly with energy.

A specific feature of energy loss of fast ions is the effect of maximum dE/dx reached near end of the range when the velocity of the particle becomes very small. At such velocities, an ion will tend to pick-up electrons from target atoms, which in effect lowers it's stopping power. Therefore, stopping power will not keep increasing as the particle's energy goes to zero, but will exhibit a specific energy loss profile, where the maximum is reached near end of the range, when, as the electron pick-up effect takes place, stopping power will drop sharply. This behavior is displayed in Figure 3.1, and such ionization profile is called Bragg curve. In this work, Bragg curve behavior will be used to inject charge carriers in the semiconductor sensitive volume, so that the maximum number of carriers is created at a desired depth.
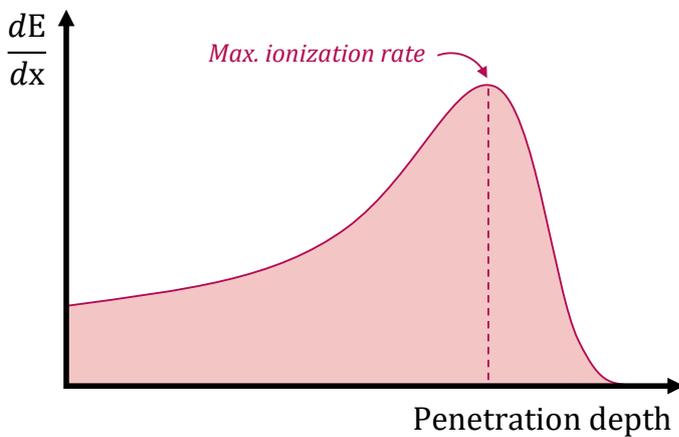
Figure 3.1: Electronic energy loss of a heavy charged particle as a function of penetration depth in matter. The particle loses most of the energy near end of the range, exhibiting specific Bragg-peak profile.

Nuclear energy loss

Energy loss of fast energetic ions by elastic scattering of atomic nuclei dominates over electronic stopping only at very low ion energies. The maximum rate of nuclear, or non-ionizing energy loss (NIEL) occurs between ~ 100 eV and ~ 1 keV for light and for heavy ions, respectively [46]. At these energies ions transfer large amounts of energy to the atomic nucleus, which usually results in displacement of the atom in the crystal lattice of the material (if the transferred

energy is higher than the binding energy of the atom). Primary knock-on atom can cause further displacements as long as it's kinetic energy is high enough. The kinematics of these interactions can be described by the scattering of two positive nuclear charges in the repulsive Coulomb potential. Furthermore, the rest of the energy is transferred to the crystal lattice due to the phonon scattering.

Simulation of electronic stopping power

To predict the effects of electronic and nuclear stopping of ions in matter, such as ion path, range, energy loss distribution with depth, damage production etc., a Monte-Carlo simulation code SRIM (The Stopping and Range of Ions in Matter) [48] can be used. This is one of the most widely accepted tools for such calculations.
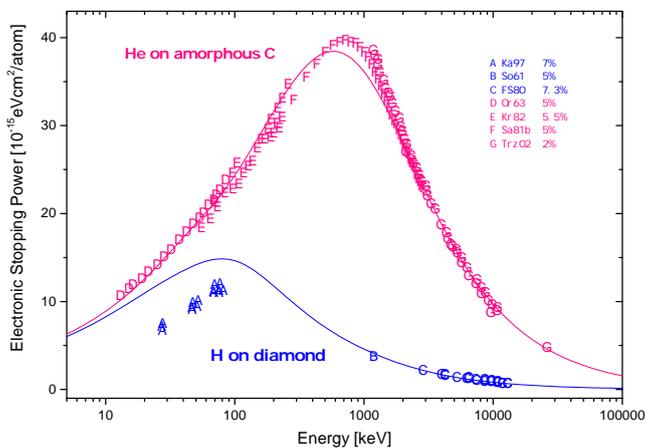
Figure 3.2: Electronic stopping power of H ions in diamond target, and He ions in amorphous carbon target, for a range of projectile energies. SRIM simulation is represented by solid lines. Experimental results from several different works are also plotted, and the sources are listed in the legend. This data was obtained through the IAEA stopping power database [49, 50].

Figure 3.2 displays both a SRIM simulation and a selection of experimental data of electronic energy loss of H ions in diamond target, and He ions in amorphous carbon target (no experimental data is available for the stopping of He ions in diamond). In this thesis both H and He ions were accelerated on a diamond detector target, and the used energies were in the 1 - 10 MeV range, where there is a satisfactory agreement of simulated and experimental results. Hence, the predictions obtained through the SRIM code can be taken with reasonable confidence. These simulations will be used on several places throughout the later chapters in support of the measurement results of the ion beam based techniques.

As for the nuclear stopping power, SRIM calculations are based on a 5 parameter "Magic formula" for atom-ion scattering, together with specific interatomic potentials that account for Coloumb screening effects. More on the underlying theory can be found in the [51, Ch. 7]. Detailed discussion on the radiation damage and defect creation due to non-ionizing energy loss will be given in chapter 3.3.

3.2 Semiconductor theory for radiation detectors

Semiconductor physics is a well developed branch, and a systematic overview of theory is available elsewhere, [17, 52, 53]. Different concepts introduced in this and the following sections were built upon multiple elements of semiconductor physics whose understanding was already assumed.

In narrow band-gap semiconductors, the number of intrinsic free charge carriers is rather high at room temperature. To obtain a region of low carrier density, or a depletion region, PN- junction is usually formed. This region depleted of free carriers acts as a sensitive volume for any new charge induced within, e.g., by ionization with radiation particles. In solid-state radiation detectors based on diamond, the sensitive volume is created in a simpler way. Since the intrinsic density of the free charge carriers is very low, the entire diamond volume between the electrodes acts as the sensitive volume. Electric field in diamond detector can be calculated from the Poisson's equation (for electrostatics)

$$\frac{d^2 V}{dx^2} = -\frac{\rho(x)}{\varepsilon} \tag{3.2}$$

where $\rho(x)$ is the charge distribution and ε is the dielectric constant. In diamond $\rho(x) \approx 0$, and the integration of the Poisson's equation yields

$$\frac{dV}{dx} = -E = const. \tag{3.3}$$

where the integration constant is determined from the geometry conditions. In other words, electric field value is constant in the whole sensitive volume. Electron and hole pairs created in the sensitive volume will drift in opposite directions due to electrostatic force.

For a case of the detector with applied voltage difference ΔV over the distance Δx, the electric field magnitude will be $E = \Delta V / \Delta x$.

Diamond crystal sandwiched between metal electrodes will operate as a solid-state ionization chamber when an electric field is applied on it. Ionizing radiation can be detected and quantified using such a device.

3.2.1 Drift and diffusion of charge carriers

Drift

Conduction electrons (and valence holes) are essentially free particles that move around the semiconductor. The average displacement of free carriers due to random motion in the crystal lattice is zero.

In low electric fields, the motion of a carrier of charge e, can be described starting with the

Newtonian mechanics:

$$\vec{F} = e\vec{E} = m^*\vec{a},\tag{3.4}$$

where m^* is the effective mass of a hole or an electron. After being accelerated, carrier will start moving at a direction of the applied field, until it scatters off phonons or charged impurities (more details later). One can assume that the average velocity after scattering events is zero, so that they are reducing the movement along the field direction. If the mean time between collisions is τ, and if we consider time interval dt, the change in velocity along the field direction, dv, will be:

$$\mathrm{d}v = a\,\mathrm{d}t - v\frac{\mathrm{d}t}{\tau}.\tag{3.5}$$

Directional movement of carriers in the presence of the electric field is called drift. Combining equations 3.4 and 3.5 gives

$$\frac{\mathrm{d}v}{\mathrm{d}t} + \frac{v}{\tau} = \frac{eE}{m^*}.\tag{3.6}$$

Velocity of free carriers will reach the stady-state value soon after the field is applied, and the dv/d$t = 0$, and we have:

$$v_d = \frac{e\tau}{m^*}E = \mu E,\tag{3.7}$$

where v_d is drift velocity, and μ is the charge carrier mobility. μ is inversely proportional to the effective mass, and proportional to the mean time between collisions. It is worth noting that μ is actually not a scalar, since carrier's mobility depends on a direction of a drift in respect to the crystalline axes (mobility is not isotropic).

Relationship 3.7 holds for electric fields that are small enough, so that the time interval between collisions is field independent. This is true when the drift velocity is small in comparison to the thermal velocity.

Thermal velocity Velocity gained from the thermal energy can be calculated from:

$$\frac{1}{2}m^*v_{th}^2 \approx \frac{3}{2}k_B T,\tag{3.8}$$

where it is visible that thermal velocity has temperature dependence: $v_{th} \sim T^{1/2}$. At room temperature, thermal velocity of carriers in diamond can be estimated as $v_{th} \sim 10^7$ cm/s.

Effective drift velocity model Empirical model [54] is used for drift velocity evaluation in high electric fields:
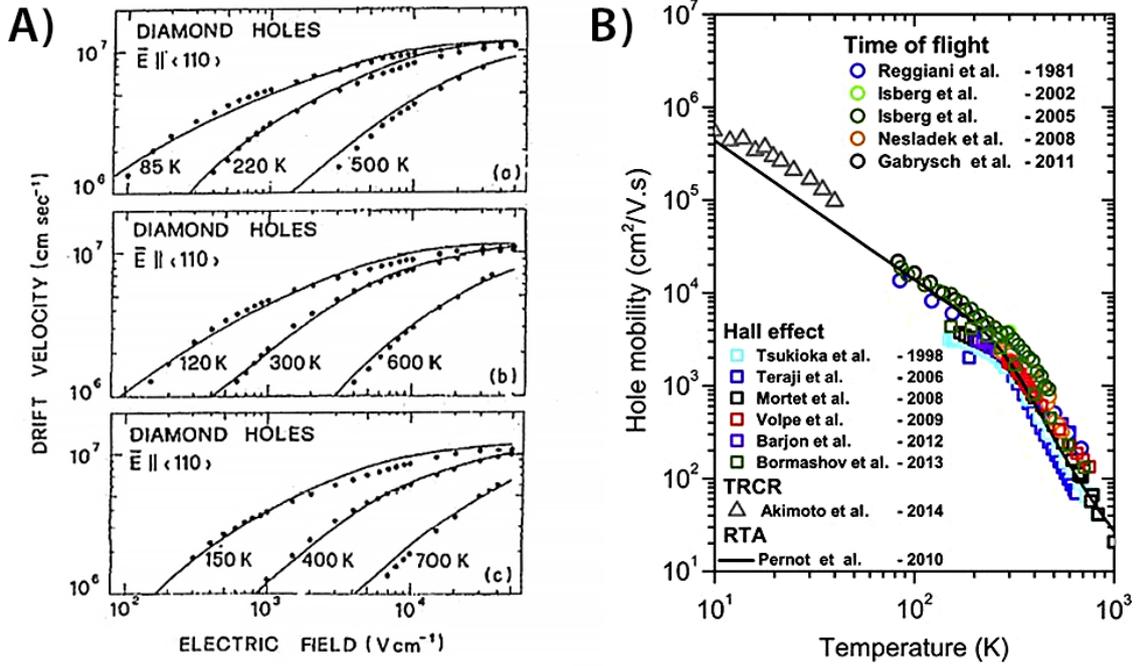
Figure 3.3: A) Hole drift velocity, in natural diamond sample, as a function of the electric field, applied in the $\langle 110 \rangle$ crystalline direction. Results were obtained at different temperatures from 85 K to 700 K. Reprinted with permission from [55]. Copyright by the American Physical Society. **B)** Hole mobility as a function of temperature in single-crystal diamonds. Solid line: calculation using relaxation time approximation (RTA). Individual points: experimental values, measured using one of the following techniques: Time-of-flight, Hall effect, Time-Resolved Cyclotron Resonance (TRCR). Reprinted from [3], with permission from Elsevier.

$$v_d = \frac{\mu_0 E}{1 + \frac{\mu_0 E}{v_{sat}}} \, , \tag{3.9}$$

where μ_0 is the zero field mobility, and v_{sat} is the saturation velocity: it is the maximum velocity of the carrier's drift through a specific crystal lattice (material constant).

Hole drift as a function of the applied electric field in natural diamond sample is shown in Figure 3.3-(A). Saturation of the velocity for high electric fields is visible. Measurements were performed at various temperatures in the range from 85 K to 700 K. Velocity increases for lower temperature, which can be explained by understanding scattering mechanisms that govern mobility of the charge carriers.

Scattering mechanisms Higher mobility (velocity) at low temperatures is caused by suppression of scattering mechanisms as thermal energy in the crystal lattice is being decreased. Mobility is affected by carrier's scattering on crystal lattice impurities and phonons. Summary of scattering mechanisms affecting carrier mobility in diamond is given in table 3.1. Impurity

scattering can significantly influence the mobility only at lower temperatures, while on temperatures around room conditions acoustic phonon scattering is the main limiting influence on the charge carrier drift. Here mobility scales with temperature approximately as $\mu \sim T^{-3/2}$. At higher temperatures optical phonons start participating in scattering mechanisms, and mobility starts to decrease even faster.

Table 3.1: Scattering mechanisms affecting charge carrier mobility in diamond. Simplified description of each mechanism is given, as well as temperature dependence and temperature range (compared to room temperature) where the influence of the effect comes into consideration.

Scattering mechanism	Type	Description	Power law	Temp. range
Impurity scattering	Ionized impurity	Ionized impurities create local Coloumb-like potentials, on which charge carrier's scatter via EM force. Scattering cross-section decreases as a carrier gains thermal energy.	$T^{3/2}$	Low
	Neutral impurity	Neutral impurities can be seen as local disturbances of the crystal lattice, and the scattering mechanism can be approximated as temperature-independent.	T^0	Low
Phonon scattering	Acoustic phonon	These phonons can be seen as collective dispacements of crystal atoms, that create longitudinal waves with wavelengths similar to that of carrier's drift wavelengths.	$T^{-3/2}$	Middle
	Optical phonon	Optical phonons are out-of-phase movements of neighbouring atoms in the lattice, and have higher energy than acoustic phonons. Hence, they affect mobility at higher temperatures.	$T^{-\alpha}$ $\alpha(T) > 2$	High

Figure 3.3-(B) plots the values of hole mobility, collected from various experimental works, together with theoretical calculation. Change of power law is visible around 300 - 400 K. Here optical phonons start to govern the mobility behavior. In general, both hole and electron mobility is high in diamond. At room temperature, measurements in high-purity diamonds using time-of-flight (TOF) techniques are grouped around ~ 2200 cm^2/Vs (with exceptions going as high as 4500 cm^2/Vs, reported by Isberg et al. in 2002 [56]). Systematically lower mobility values are reported using Hall effect. This discrepancy has not been fully understood yet [57]. Hole mobility seems to be comparable to electron mobility, with values reported for room temperature ranging from 2000 to 3000 cm^2/Vs. Values obtained by Hall and TOF techniques are generally in close agreement. Notably, very high mobility (3800 cm^2/Vs) was reported in sc-CVD diamond by Isberg et al. [56] using TOF measurements.

Electron and hole mobility in silicon are significantly lower (around 1400 and 500 cm^2/Vs respectively).

To conclude, charge carrier mobility in diamond is high. This is mainly based on high energy of phonons [58]. At elevated temperatures mobility scales as $\mu \sim T^{-\alpha}$ with $\alpha > 2$, which can lead to order of magnitude mobility decrease from room temperature (RT) to 1000 K.

Diffusion

In the absence of electric field, electron and holes can still move through the crystal lattice due to inhomogeneous distribution of free carriers. Their movement than can be described as a Brownian-like motion. This process is called diffusion, and it will force carriers to move until (local) equilibrium is reached. Diffusion is described through the flux $\vec{F}$ equations:

$$
\begin{aligned}
\vec{F}_n &= -D_n \nabla n \\
\vec{F}_p &= -D_p \nabla p .
\end{aligned}
$$

(3.10)

(3.11)

$\vec{F}_{n/p}$ is the electron/hole flux, $D_{n/p}$ is the corresponding diffusion constant, and ∇n (∇p) is the gradient of electron (hole) concentration.

Mobility and diffusion are related through Einstein equation:

$$
D_{n/p} = \frac{k_B T}{e} \mu_{n/p} .
$$

(3.12)

Current due to drift and diffusion

Current density due to combined effect of drift and diffusion will be:

$$
\vec{J} = e(n\mu_n + p\mu_p)\vec{E} + e(D_n \nabla n + D_p \nabla p) ,
$$

(3.13)

and it is referred to as drift-diffusion current. Drift component normally dominates, unless the applied electric field is very low, or it is locally screened in the regions of the semiconductor bulk (which can occur due to build-up of frozen charge, or polarization). Then, diffusion component can become comparable or dominant to drift.

3.2.2 Signal formation: Shockley-Ramo theorem

If one applies electric field through the semiconductor volume through electrodes, free carriers (electrons and holes) will be forced to drift in the direction of the field gradient. This will in turn induce surface charge and current on the electrodes. In the theory developed by Shockley [59] and Ramo [60], a point charge q moves in the presence of an arbitrary number of electrodes, but only one electrode (sensing electrode) is biased at unit potential, and all other electrodes are at zero potential. The current I_{ind} induced at the sensing electrode at any point during the carrier motion will be:

$$
I_{ind} = \mathrm{d}Q_{ind}/\mathrm{d}t = -q\,\vec{v}\cdot\vec{F}_w ,
$$

(3.14)

where $\vec{v}$ is the velocity of the carrier, and $\vec{F}_w$ is the weighting field at the current position of the motion. Weighting field is defined as a derivation of electric field over the electric potential on that electrode. In a simple case of a parallel-plate geometry, and in the absence of space charge distribution between electrodes, weighting field can be expressed as:

$$\vec{F}_w = \vec{E}/V .\tag{3.15}$$

$\vec{E}$ is the constant electric field, created in the semiconductor volume. This geometry is displayed schematically in the Figure 3.4.
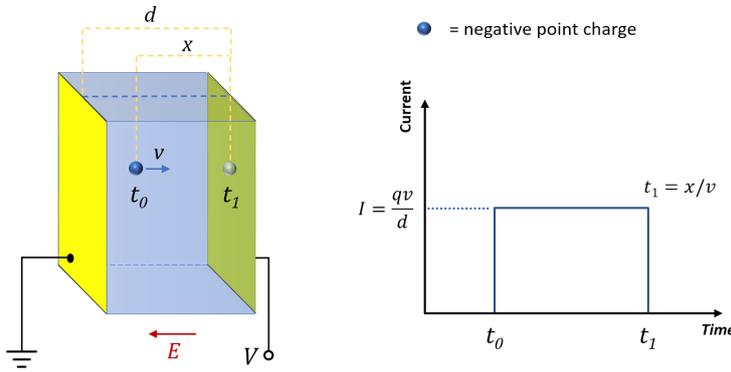

Figure 3.4: (Left panel) Schematic representation of the semiconductor detector with parallel plate geometry. Point charge is created on distance x from the sensing electrode. (Right panel) Current signal from the detector, based on the Shockley-Ramo theory, under assumption of constant electric field between electrodes.

We know that in this case $E = V/d$, where d is the distance between electrodes, and where we have dropped the vector notation since this can be understood as 1D problem. It follows that:

$$F_w = \frac{1}{d},\tag{3.16}$$

and the induced current will finally be:

$$I_{ind} = -\frac{qv}{d} .\tag{3.17}$$

Drift velocity is only dependant of the electric field, which is set by the bias potential, and is constant in the whole device volume in the parallel plate geometry. Induced current will therefore have a constant value during drift time of the charge carrier, until it reaches the sensing electrode. This is displayed in the right panel of Figure 3.4. Please note once again, charge carrier does not need to reach the electrode for current/charge response creation. Drift of the carrier is responsible for instantaneous mirror-charge induction on the electrodes, which results in signal response of the detector in the whole time window $(t_1 - t_0)$. Shockley-Ramo theory can be proved on the basis of energy conservation of mirror-charges [61, 62].

Equation 3.17 can be rewritten to represent a more general case where one does not have a single charge carrier, but a distribution of charges moving in a detector volume. This distribution can

be represented by current density $j(x,t)$, and:

$$I_{ind}(t) = \frac{1}{d} \int_0^d j(x,t)dx \qquad (3.18)$$

For more realistic evaluation of signal created in the detector, trapping effects need to be included, as well as non-homogeneous electric field profile.

3.2.3 Semiconductor-Metal interfaces

To establish an electric field in diamond and prepare a radiation detector, metal contacts need to be connected on the semiconductor. Typically, and for the purposes of this work, planar electrodes are deposited on two opposing faces of the diamond crystal, forming an electric field and thus a sensitive volume for radiation detection. The electric field vector is uniform in direction and magnitude in all points between electrodes.

Good quality contacts are critical for the application of semiconductors as electronic devices. For diamond radiation detectors, the contacts should not inject free electrons from the metal side when the bias voltage is applied. They must also be effective in extracting excess charge from the diamond side. Two types of contacts can be distinguished: ohmic and Schottky.

Ohmic contacts is a metal-semiconductor connection in which the voltage drop across the interface is small compared to the voltage drop across the active device volume. Diamond detectors with ohmic contacts should have a linear or quasi-linear current-voltage characteristic.

The other type of contact was first theoretically explained by Schottky in the 1930s [63, 64, 65], and in his honor it is commonly refereed to as Schottky contact type (or Schottky barrier theory). The potential barrier across the metal-semiconductor junction is formed due to the difference of two Fermi levels. Diamond detector with Schottky contacts will have a built-in potential even when no bias voltage is applied through the electrodes (due to the potential barrier, voltage drops across electrode interfaces with diamond). In addition, diamond detector with Schottky contacts has a distinctly nonlinear current-voltage characteristic.

It is also important to give a brief discussion on the treatment of diamond surfaces before the electrodes are deposited on them.

The surface of diamond, after the crystal growth phase, is usually treated with a hydrogen- or oxygen-termination process. Termination affects the surface in different ways depending on the direction of crystal growth, mainly by determining the number of danging bonds and surface chemistry of the end layer. Dangling bonds, which are unsaturated covalent carbon bonds that exist on the edges of the material, are terminated and the surface becomes stable after this treatment. The height of the Schottky barrier, and more generally the stability of the metal-semiconductor interface is affected by termination process. In this work, single-crystal CVD
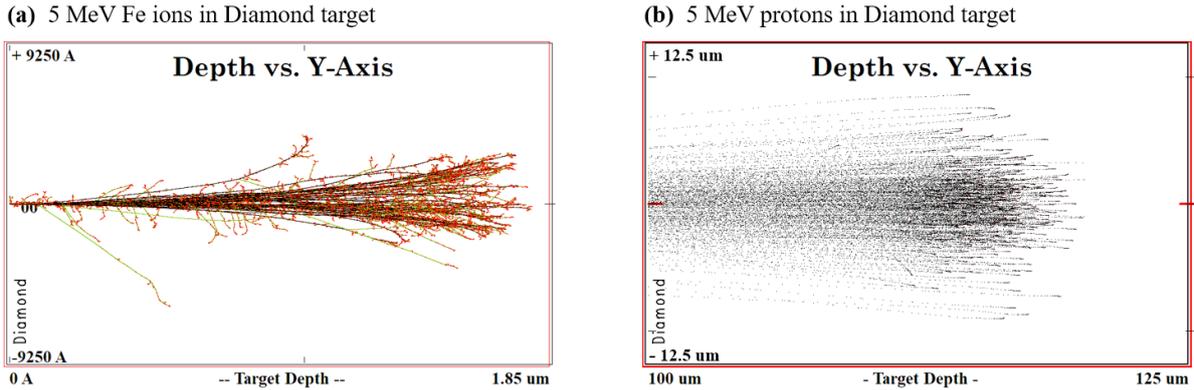
(a) 5 MeV Fe ions in Diamond target

(b) 5 MeV protons in Diamond target

Figure 3.5: SRIM simulation of collisions during ion penetration in diamond, using "Detailed Calculation with full Damage Cascades" mode. Plot **a)** displays full range (0 - 1.85 μm) of stopping of 5 MeV Fe ions (50 ions calculated); while **b)** displays only end of the range region (100 - 125 μm) of stopping of 5 MeV protons (500 ions calculated). Black points are locations of collisions between ion and target atom, and they can be used to track individual ion trajectories. Green points represent calculated collisions of recoil atoms with other lattice atoms, resulting in new knock-on atoms. Red points are the positions of stopped ions and atoms. Primary knock-on atoms receive more energy during stopping of heavy MeV ions, which enables multiple new collisions (collision cascades) during their own stopping. Collision cascades lead to defect clusters. On the other hand, light MeV ions (H and He) primarily produce only point defects, vacancies and interstitials. *Note: single red points are barely visible in figure b) without zooming in.*

diamonds with <100> orientations were used. The samples were treated in oxygen plasma for O-termination.

3.3 Overview of defects and Shockley-Read-Hall population statistics

3.3.1 Defect production with MeV ions

During the penetration of charged particles through the solid target, they can come to a complete stop, provided the thickness of the target is larger than the range of the projectile. The nuclear stopping power will have a strongest contribution near the end of penetration range, as the ion energy drops to zero.

The minimum energy to displace atoms from their lattice positions is called the displacement-threshold energy. The displaced target atoms are usually referred to as primary knock-ons. After leaving their lattice sites, these atoms are stopped as interstitials, and their original sites are left as vacancies. A primary knock-on atom can have enough energy to induce new, secondary, interstitials and vacancies, before coming to a stop.

For diamond, displacement energy ranges from 38 - 48 eV for different crystalline directions, as measured in the experiments with incident electron beam [66].

Figure 3.5 shows the results of the simulation of collisions occurring during the energy loss of two types of MeV ions in diamond, 5 MeV Fe ions and 5 MeV protons. Heavy Fe ions have a much shallower penetration range than light ions, such as H or He. Mean energy loss per travelled distance is therefore much higher for a heavy ion.

During the stopping of light ions, the collisions result in low energy transfer to displaced atom, which are stopped near by the original site as interstitials. However, the average energy transfer during the collisions with heavy ions is higher. Therefore, primary displacements are more likely to absorb enough energy to cause secondary collisions during their stopping [67, p. 277]. These so-called collision cascades can produce multiple new vacancies and interstitials near the stopping range of the recoil carbon atom track. The high density of point defects in collision cascades leads to defect agglomerations or defect clusters. Simulations suggest that clusters should have electrical properties different from point defects [68], but little experimental evidence for their existence or crystal structure characteristics is available (see, for example, investigation into oxygen clusters in Si [69]; or a more comprehensive overview of extended defects in a book by D.B. Holt and B.G. Yacobi [70]).

3.3.2 Defect evolution after irradiation

There are no accurate models for the evolution of ion-induced damage in semiconductors. This is due to two general problems: a) Wide range of factors determine the dynamics and a final state of a defect - these include temperature, already present impurities, type and energy of the ion, charge state of the defect; b) Difficulties in accurately characterizing the crystalline nature, concentration and spatial distribution of a defect. This prevents the establishment of a quantitative framework for predicting defect evolution. However, a few defects have been studied more extensively, and their origin and properties have been determined. A brief overview of most studied defects, that are common in synthetic diamond, is given here. All of these point defect species can be formed due to ion beam irradiation. A more complete overview can be found in [71, Ch. 3]

High level irradiation with MeV ions will lead to amorphization of diamond, that is, to the collapse of crystalline order. However, ion irradiation below the amorphization threshold will result mainly in large number of vacancies (V) and interstitials (I) produced in collisions. These are formed in highest density at the end of the range of the ion path.

Both V and I are stationary at room temperature and stay mostly fixed at their lattice sites after creation. So the next defect complexes will be usually formed only upon their thermal activation, after which they become mobile. The illustration of the processes of V- and I-related
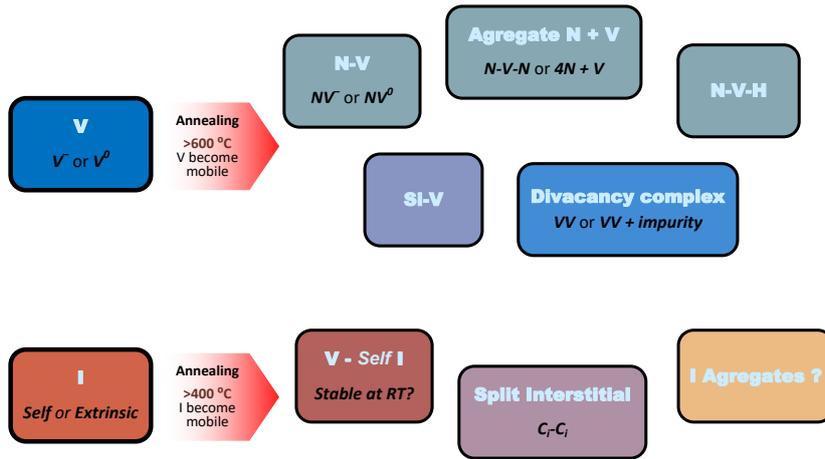
Figure 3.6: Some of the defect complexes formed in diamond after irradiation. *V* or *I* become mobile at different temperatures in diamond. *V*-related complexes seem to be more abundant and investigated.

defect evolution in diamond is given in Figure 3.6.

Vacancy is a trapping center and exists in a neutral (GR1[*]) charge state, and negative charge state (ND1). Vacancies become significantly mobile in diamond at temperatures above $600\,^\circ$C [72]. Mobile vacancies will tend to form stable defect complexes with N (which is commonly present even in best quality crystals). NV center is the best known product of this interaction, because of its unique spin properties [73] that make this defect a promising candidate for applications in quantum sensing and information processing. Furthermore, if aggregate nitrogen is present in diamond, vacancies can form N-V-N complexes or 4H centers (4N + V) in such environment. Divacancy complex is a stable defect that can also be formed after irradiation, and further create more complex defects with other impurities (VV + impurity).

Both self-interstitials and extrinsic interstitials (from ion species) are formed during ion irradiation. Self-interstitial in diamond (more precisely <100> - split self-interstitial, I_{001}^0) was the first observed isolated self-interstitial in any group-IV material. Its activation energy was determined as $\approx 1.6\,$eV, meaning that it is thermally activated at temperatures above $400\,^\circ$C [74]. Interestingly, it appears that smaller number of interstitials than vacancies survive after irradiation at room temperature. This can be explained by an alternative, highly mobile state of an interstitial, that leads to increased recombination during irradiation [75]. This interstitial form could have very low migration energy level of $0.3\,$eV. After irradiation, the surviving interstitials go back in low mobility state. Therefore the dynamics of I-related defects might be different during and after irradiation (in a latter case, new defect formation can be induced only at temperatures $> 400\,^\circ$C). Small number of stable I-related defects have been identified up to date. $C_i - C_i$ pairs [76] are one of those confirmed, also I-V pairs [77].

---

[*]Common names of some more famous defect levels in diamond will be given in this section. The history of their naming varies, but most were identified in various optical spectroscopy experiments.

3.3.3 Trapping/Detrapping phenomena

Theory proposed by Shockley, Read and Hall (SRH) [78, 79] is often used to explain charge trapping and recombination on energy levels formed in the band-gap due to electrically active defects. Let us consider a level in a band-gap, that is formed due to existence of an impurity in the crystal lattice. This impurity will have a possibility to capture and emit electrons and holes. Level is either occupied by electrons or by holes. In other words, it can exist only in one of those two states. Impurities occupied by electrons have density n_t, and occupied by holes p_t, so that total impurity density is N_t. Processes considered in the SRH theory are displayed schematically in Figure 3.7. They are: (a) electron capture, (b) electron emission, (c) hole capture, (d) hole emission, (e) pair generation (equivalent of process (b) followed by (d)), (f) pair recombination (equivalent of (a) followed by (c)).
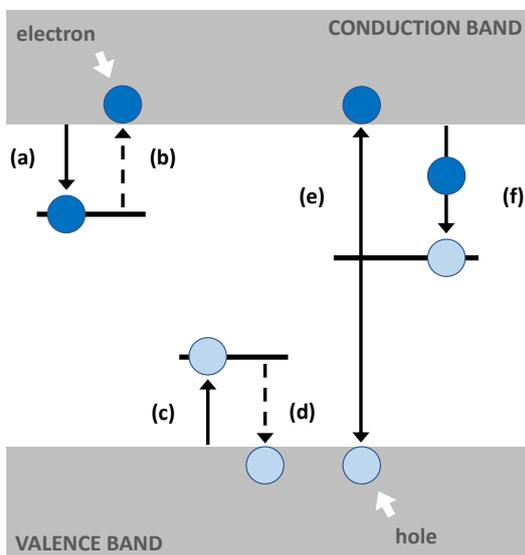

Figure 3.7: Processes in Shockley-Read-Hall model: **(a)**electron capture, **(b)**electron release, **(c)**hole capture, **(d)**hole release, **(e)**e-h generation, **(f)**e-h recombination. Levels near band edges are considered as shallow levels, and trapping time on them is usually not long. Therefore, probability of re-emission of the captured carrier to the band is high. Trapping on the deep level is much stronger. For example, a hole from the valence band is captured on the deep level. Subsequently, conduction electron is also trapped, as in process (f), before the hole was released. In this way, e-h recombination occurs, and free charge is lost.

Traps and recombination centers   Energy level can be considered as a trap if, i. e. after electron capture (a), there is a greater probability for detrapping (b), than for hole capture (c). For hole trap, (c) is followed by (d). Traps are usually close to band edges, and thus have a significant probability to capture just one type of charge carriers (donors or acceptors). Levels that are closer to the middle of the band gap will have greater probability for generation and recombination processes, and are usually called generation-recombination (G-R) centers. Due to prevalence of the term "trap" in the literature, all centers will usually be referred to as traps, or have a subscript "t", regardless if they are dominantly acting as a G-R center or a trap. Let us list properties relevant for the SRH statistics:

- density of electrons in the conduction band, n
- density of holes in the valence band, p
- trap's capture cross-section: for an electron, σ_n; for a hole, σ_p

- average thermal velocity of a charge carrier, v_{th}
- emission probability from a trap: of electrons, e_n; of holes e_p.

Capture rate (or trapping rate) for electrons is given by:

$$r_c^e = n\sigma_n v_{th} p_t \,, \qquad (3.19)$$

and it is proportional to the electron capture cross section, electron thermal velocity, density of electrons in the conduction band (since the electron is being captured from the conduction band) and number of traps not occupied by electrons (in other words, occupied by holes).

Detrapping rate (or release rate) for electrons is given by:

$$r_d^e = e_n n_t \,, \qquad (3.20)$$

and it is proportional to the electron emission probability and number of traps already occupied by electrons (since electrons are going from the trap into the conduction band).
Analogously, trapping and detrapping rate for holes are: $r_c^h = p\sigma_p v_{th} n_t$ and $r_d^h = e_p p_t$.

While generation and recombination effects change the number of free charge carriers in the device permanently, trapping and detrapping events have temporal effects, in the sense that charge captured in trapping centers is only temporally immobile. The lifetime of electrons and holes is determined by the number of different trapping centers present in the lattice, and their distribution.

Donors and acceptors   n- and p- doping technologies are well established for silicon, where they are used to form junctions of differently doped material, that enable realization of devices such as diodes and transistors. Intentional doping forms shallow levels in the band-gap that enable control of conductivity and other semiconductor properties. Doping induced levels are usually referred to as donor and acceptor levels, to distinguish them from other *unwanted* impurity centers.

In diamond, p-type doping is possible with boron, which forms an acceptor level at 0.37 eV above the valence band maximum. n-type doping is more difficult to achieve artificially. Nitrogen forms a deep level in diamond, 1.17 eV below the conduction band. Doping with phosphorus appears to create a more favorable shallow level, with an activation energy of 0.57 eV.

For microelectronic device development, a suitable doping technology must allow fabrication of thin layers in a semiconductor with desired doping concentrations depending on a final device application. The development of such devices with B and P doping is a very active research area

with promising results for power electronics technology [3, 31, 80, 81]. In contrast to power devices, diamond-based radiation detectors exploit intrinsic properties of diamond crystals. Any impurity that forms deep or shallow levels in the band-gap is undesirable, because it lowers the effective resistivity and affects the transport properties of the charge carriers, such as lifetime and drift distance. Nitrogen and boron are the main impurities in CVD diamond growth. Their concentration must be reduced to obtain the best crystal purity without shallow or deep levels that can be used for radiation detectors.

Polarization   The polarization effect occurs due to build-up of trapped charge in the crystal lattice. The space charge affects the electric field in the detector, as the externally applied field can be neglected due to the internal polarization field. The number of accumulated charge carriers and their distribution determine how severe the impact on detector performance will be. Typically, the polarization mechanism is explained by two most probable scenarios: a) *surface polarization*, trapping of carriers at the metal-semiconductor interface or: b) *bulk polarization*, the accumulation of space charge at traps randomly distributed throughout the detector volume (such trapping centers usually originate due to the incorporation of impurities in a diamond during the crystal growth - unintentional "doping"). Finally, separate scenario has to be mentioned, where the detector is exposed to large dose of radiation that induces new trapping centers in the material. Polarization effect can become more pronounced in such conditions [82], as compared to pristine, undamaged detector.

3.4   Overview of silicon and diamond for radiation detection

Some properties of silicon and diamond have a significant impact on radiation detection capabilities and detector design and deserve direct comparison and summary. Focus is put on specific applications where diamond offers performance improvements or new frontiers. Due to large band-gap value, visible light photons do not have enough energy to ionize diamond, so diamond detectors have a property of solar blindness and can be operated under light without effect on electronic properties. Silicon-based detectors on the other hand have to be operated in darkness. Due to low atomic number (Z=6) diamond is very tissue-equivalent, and a growing number of applications in medical- and bio-physics have been reported in recent years, out of which new developments in diamond dosimeters for radiation therapy are particularly interesting [83, 84]. On the other hand, silicon's higher atomic number (Z=14) ensures better cross-section for γ-rays or X-rays. In neutron reactors, radiation monitoring requires separation of neutrons from large gamma background. Diamond's high transparency for gammas makes it favorable for such applications. Fast neutrons can deposit energy directly in diamond through inelastic scattering on carbon. For thermal neutrons, neutron converter to charged particles needs to be used

[85]. Many research groups are actively investigating possible solutions for high neutron flux or neutron cross-section measurements [85, 86, 87]. Regarding intrinsic electronic properties, due to almost 5 times lower band-gap value as compared to diamond, silicon offers superior spectroscopic resolution. Lower band-gap equals to lower pair-creation energy, so that the same energy deposited by the radiation particle will produce more signal in silicon. Moreover, this feature favors detection of low ionizing particles using silicon detectors, like in large solid angle multi -strip and -pixel detector systems in particle physics [88, 89]. But wide band-gap offers advantages in other electronic properties and radiation hardness. Leakage current properties in diamond detectors are by far superior to silicon and germanium (even when they are cooled), and leakage remains low even at elevated temperatures (as it was already discussed). High resistivity of diamond offers possibility of formation of solid-state ionization chamber without the need for pn-junctions. This can be exploited in advanced detector geometries, where electrodes are buried in diamond as pillars, or even more complex 3D structures [90]. Such structures can give regions of high electric field on tight micrometer scale distances where particle collection time is very short. Fast response to radiation is also enabled by high mobility and saturation velocity of both electrons and holes in diamond. This feature is important for fast counting or timing applications, for example in high luminosity X-ray beam monitoring [91, 92]. Radiation hardness is another promising feature of diamond, as strong bonding of the crystal lattice ensures higher threshold for defect production [93]. Deep trapping levels in diamond are, on the other hand, an important limiting factor in realization of full potential of this material, specially regarding to polarization phenomena [94]. Silicon is by far superior in this regard, as even low temperature annealing of defects can recover materials properties significantly. Interestingly, by exploiting natural strength of diamond, self-supported thin diamond films (membrane-like) can be realized as detectors [95]. Membranes demonstrated excellent radiation hardness and resistance to polarization [96, 97], due to the extremely short distance across which the electric field is applied, enabling the charge multiplication regime.

Finally, strong covalent bonding of carbon atoms makes diamond chemically inert, enabling resistance to chemically active mediums.

4. Experimental techniques

Most of the experimental work performed in this thesis was based on the use of ion beams with the ion microprobe setup. Ion microbeam was used to either induce electron hole pairs in the detector (probing beam), or to produce radiation damage (damaging beam) for the purpose of analysis of defects and radiation hardness in diamond. Fast ions of the MeV energy can deposit a large amount of energy in a short penetration distance (with heavier ions of smaller energy), or they can be used to transverse the whole thickness of the device (with lighter ions, like protons, of higher energy). This capability together with the ability to achieve focused beam spot size smaller than one micrometer, makes ion microbeam a powerful analytical or materials modification tool. After description of the microbeam technology, details are provided on the use of the ion beam probing for investigation of charge transport properties: mobility-lifetime characterization, charge transient spectroscopy and recording of transient current signals.

4.1   Ion microprobe

Ion microprobe setup is located at the Ruđer Bošković accelerator facility, which is operated by the Laboratory for Ion Beam Interactions (LIBI) [98]. Ions are accelerated in one of the two attached electrostatic accelerators, 1.0 MV HVE Tandetron and 6.0 MV HVEC EN Tandem Van de Graaff. Ion sources equipped before the accelerating stages are able to produce a variety of ion species (H, He, Li, C, Si, Cl, Cu, Au, etc.). Layout of the facility showing both accelerators and all 9 experimental beamlines is shown in Figure 4.1.

The ion microprobe system consists of beam focusing elements along the beamline and an experimental end-station in which the sample is positioned. To achieve focusing of energetic ions to a micrometer-sized spot at the sample position, the beam is both physically truncated along the path by use of small apertures and compressed via Lorentz force action with so-called quadrupole magnetic lenses. The beam current and beam size is initially defined by the primary aperture (object slits). Approximately 6 m downstream toward the end-station beam is further cut by the collimator slits. After that, ions enter a set of three magnetic quadrupoles. The magnetic force in each quadrupole squeezes the ions into a single plane. Therefore, at least two quadrupoles are needed to achieve focusing in both axes.
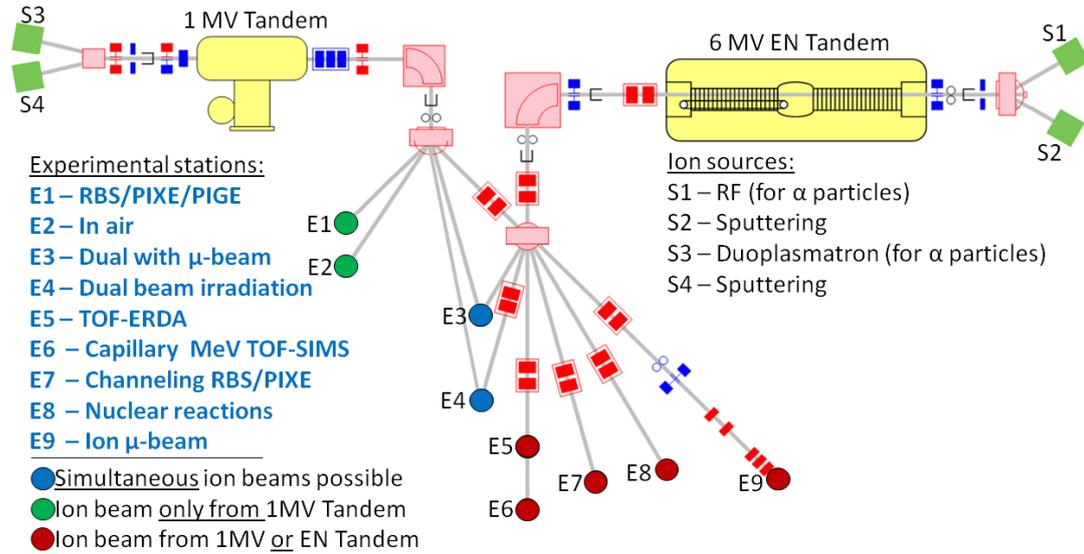
Figure 4.1: Layout of accelerators and experimental beamlines at Ruđer Bošković Institute accelerator facility in the year 2021. E9 marks the position of the ion microprobe end-station.

Result of ion optics simulation for ray-tracing, showing path of 2.5 MeV protons as they approach end of the microprobe line is displayed in 4.2. LIBI microprobe system uses the so called high-exication Oxford triplet configuration, that employs 3 qudrupole lenses, with a working distance (distance from the last qudrupole to the focal point) of 11.2 mm. The precise alignment of the two aperture sets ensures that the ions enter the magnetic lenses in a correct, well-defined trajectory, that follows the central axis of a magnetic triplet. For good focusing outcome, object slits opening is $< 100\,\mu m$ and collimator slits opening is $< 1\,mm$. In this geometry, ions are routinely focused to a spot size of a $1 - 2\,\mu m$ profile in both dimensions. Under the most favorable conditions, with highly reduced beam divergence by tightly closed slits, spatial size of the spot is reduced down to ≈ 250 nm profile. With small aperture openings significant portion of the beam current is cut along the path, before reaching the sample. Usually, no more than 10 fA current on the sample position can be achieved in the low current mode needed for good focusing. In high current mode (with larger slit opening) current ranges from ~ 1 pA to ~ 1 nA.

Triplet configuration is capable of focusing ions of lower rigidity, up to 6 MeV ME/q^2. For higher rigidity focusing (up to 15 MeV ME/q^2), configuration of magnetic lenses is changed to a simple doublet using only the first two magnetic quadrupoles. The ion beam can be raster scanned over the sample surface with the use of magnetic deflection system. Maximum scan size depends on the ion beam rigidity, but generally is between 1 and 2 mm^2. In-house developed SPECTOR software [99] integrates the scanning process with data acquisition system for various ion beam analysis techniques available in the microprobe system. In other words, software correlates beam position with the data collected by the detectors used in the experiment. Spatial resolution is directly proportional to the size of the beam spot.
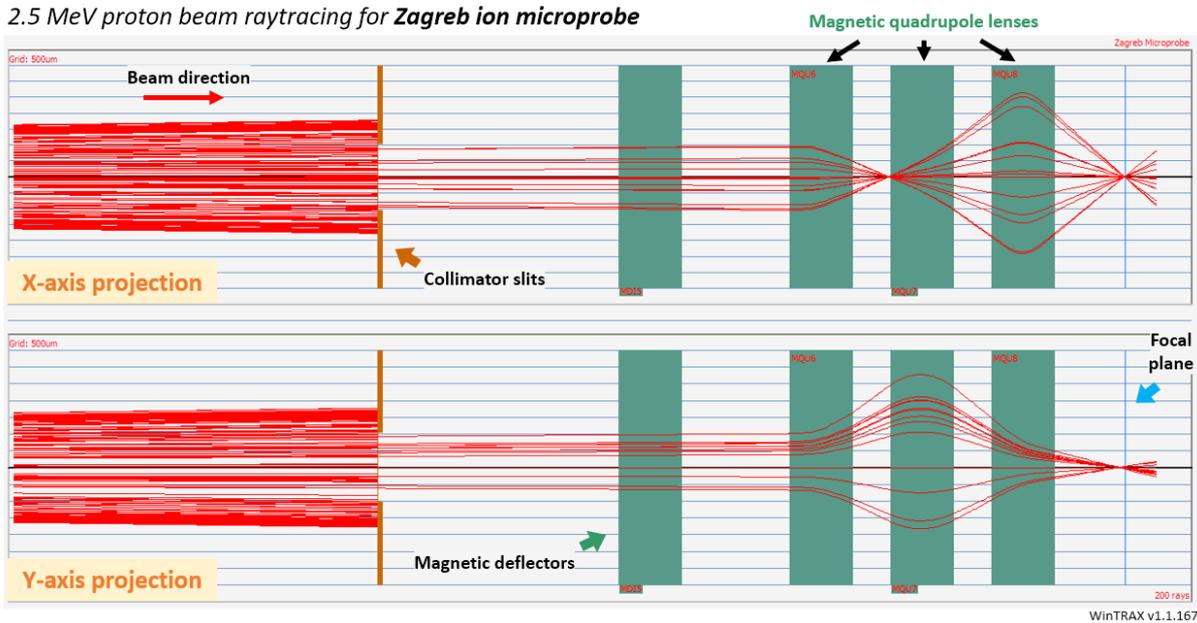
Figure 4.2: Simulation of ion beam optics, for 2.5 MeV ions accelerated towards the ion microprobe experimental station at LIBI microprobe facility. Only last portion of the path is displayed, where beam is cut by collimator slits (1×1 mm^2 opening) and focused by magnetic quadrupole lenses. Note that, in presented triplet configuration, ion beam focusing is stronger in horizontal plane, then it is in vertical. Simulated using WinTRAX software, developed by *Oxford Microbeams Ltd.*

4.1.1 Ion Beam Induced Charge (IBIC) technique using ion microprobe

In the IBIC technique [100, 101] each single ion that impinges on the sample is used to ionize the sensitive volume of a semiconductor detector. The detector is exposed to the focused ion beam (with ion rate of around 1 kcps*) and coupled to a readout electronic chain that registers the response signal. In the ion microprobe, beam's position can be controlled, which enables spatial mapping of the device response with the micrometer resolution. In a such setting IBIC microscopy offers unique capabilities and advantages over other detector characterization techniques. A single MeV ion generates high number of electron-hole pairs along a well defined penetration trajectory.

This trajectory is nearly a straight line, because low angle scattering events (ion-electron collisions) are statistically dominant during the energy loss. At the ion's end-of-range energy is reduced enough so that ion-atom collisions (nuclear stopping) become equally probable, which impacts the trajectory angle more significantly.

Ions with energies in the range of $10-100$ keV have a larger contribution of nuclear stopping during energy loss, and therefore undergo more deviations from their impact trajectory as compared to MeV ions. For example, the average ratio of the projected ion range and the total
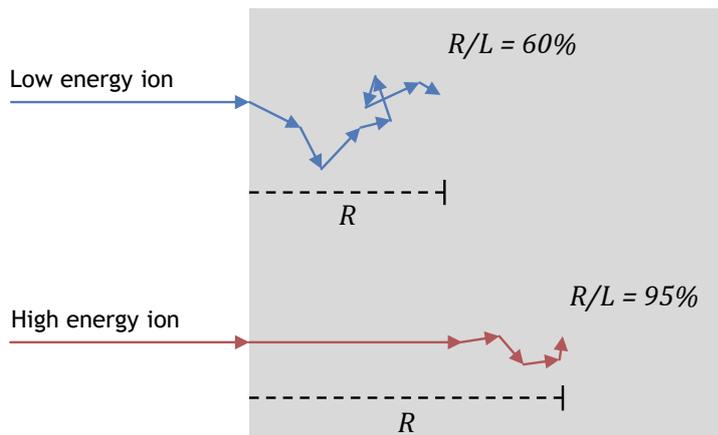
---

*cps = counts per second.

Figure 4.3: Typical trajectories of low- and high-energy ions in a semiconductor material are shown. The spatial dimensions of two cases are not to scale, as the low-energy ion path is enlarged for visual clarity. Average ratio of projected range and total path length, R/L, is close to 1 for the high-energy trajectory. Ions above 1 MeV energy can be considered as high-energy in this context. Based on [102, p. 300]

trajectory length for a 40 keV ^{7}Li ion in germanium is 0.4 [102, p. 301]. Typical trajectories for low- and high-energy ions in a material are displayed in Figure 4.3. Variations in range and angle of individual ion trajectories result in longitudinal and lateral straggling of the ion beam, which limit the final resolution of the IBIC imaging.

Due to low mass of an electron, an electron beam stopping in solids generates even more large angle scatterings.

By choosing ions of different mass and energy a wide span of penetration depths can be covered in a microprobe experiment, from $\sim 1\,\mu m$ for heavy ions to $\sim 100\,\mu m$ for MeV protons. In this way one can choose an appropriate ion beam to probe a desired depth of a sample under investigation. In semiconductor radiation detectors, different ions can be used to induce charge carriers just in a small volume beneath the sensing electrode; or throughout the whole active thickness of the device. Small ionization volume and well defined ion positions in an ion microprobe setting enables us to probe the whole volume of a typical semiconductor device (with dimensions of the order of: 1 mm x 1 mm x 100 μm) with micrometer resolution. Each ion typically generates enough charge carriers for a measurable electronic response. Therefore, IBIC can be considered as a single ion technique.

The schematic overview of the ion microprobe used in an IBIC measurement is shown in Figure 4.4. To obtain a 2D IBIC map, the ion beam is raster scanned across the sample. The signal response from the device is processed through a charge-sensitive preamplifier and integrated by a shaping amplifier. The charge signal is further processed by the ADC unit, where analog-to-digital conversion and pulse height analysis are performed. Software than incorporates all the information (pulse height, time stamp, beam position) into a user interface with a 2D map and event count histogram. The data is updated in real time, allowing the user to observe the effects instantaneously as the beam is scanning. In offline analysis, it is possible
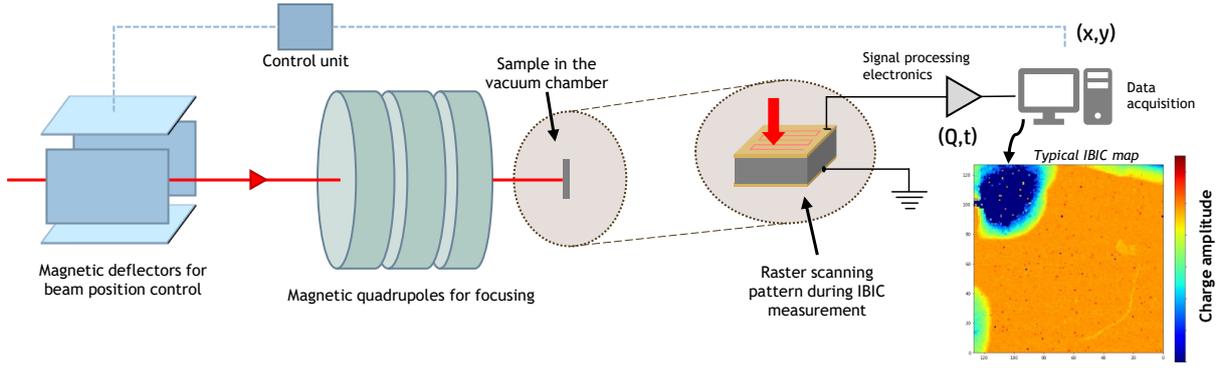
Figure 4.4: Schematic depiction of the IBIC microscopy experiment at the ion microprobe. Semiconductor detector is exposed to focused ion beam that is raster scanned over it. Each ion induces signal response in the detector that is processed and recorded together with a beam position information and a timestamp of the event. 2D IBIC map is recreated live during beam scanning, and each pixel represents average charge amplitude mapped to that position.

to filter and extract data corresponding only to certain timestamps or beam positions. Maps are recreated so that each pixel represents the average charge amplitude collected at that position (since the beam passes over the same position multiple times during scanning). The event rate during IBIC scanning does not exceed 1 kcps to avoid charge pile-up in the processing electronics. Scanning speed is defined by the "time-per-pixel" parameter, which is usually set in the 1 μs range. The sample is positioned in the chamber with 4 degrees of freedom (3 translational and 1 rotational so that the sample surface can be tilted with respect to the beam axis).

4.2 Mobility-Lifetime characterization

Let us consider what occurs with charge pairs, electrons and holes, after they are induced in the semiconductor crystal by an ionization process. If the electric field is applied, holes will drift in the field direction, and electrons in the opposing direction. Along their movement path they will encounter impurities in the lattice, where charge carriers can get trapped and recombined. Therefore, lifetime of a carrier, τ, will not be infinite, but limited by the trapping-detrapping mechanisms. With an assumption of a homogeneous volume distribution of the traps, we can write the differential equation for the number of free carriers in time:

$$\mathrm{d}n = \frac{n}{\tau}\mathrm{d}t\,, \tag{4.1}$$

If n_0 is the starting number of free carriers, the solution to the equation is:

$$n(t) = n_0 e^{-\frac{t}{\tau}}\,. \tag{4.2}$$

Current induced due to electron drift

For simplification we can continue with the calculation assuming only one type of carriers, electrons, drifting through the semiconductor under the applied electric field E. This situation is realistic for short range ion probing in a parallel-plate electrode geometry (figure 3.4, ions penetrate just beneath the electrode on negative potential). Distance between electrodes is d. In such geometry, holes will have a negligibly short drift time before they reach their collecting electrode, and therefore negligibly small contribution to the induced current and charge according to the Shockley-Ramo theorem. Majority of the output signal is induced by electron drift. As induced current is proportional to the number of moving electrons that are being trapped, it will decrease exponentially in time, in accordance to equation 4.2:

$$I_{ind}(t,E) = \frac{e\,n_{0,e}\,v_e(E)}{d} e^{-t/\tau_e}.$$ (4.3)

Subscript 'e' in the parameters of number (n_e), drift velocity (v_e) and lifetime (τ_e) denotes that they refer to electron properties. Induced charge is obtained by time integration:

$$Q_{ind} = Q_0 \frac{v_e(E)}{d} \int_0^{t_e} e^{-t/\tau_e} \mathrm{d}t = Q_0 \frac{v_e(E)}{d} \tau_e \left(1 - e^{-t_e/\tau_e}\right)$$ (4.4)

where $Q_0 = e\,n_{0,e}$ is the number of free electrons at $t = 0$ (injection), and integration limits are taken from $t = 0$ to $t_e = d/v_e(E)$, which is drift time for electrons. This relation can be used to estimate carrier's lifetime τ, if drift time can be measured independently.

We can rewrite the last equation by implementing the expression for t_e and taking into account that $v(E) = \mu_e E$, so that we have:

$$CCE = \frac{Q_{ind}}{Q_0} = \frac{(\mu_e \tau_e)E}{d} \left(1 - e^{\frac{-d}{(\mu_e \tau_e)E}}\right).$$ (4.5)

Here we have introduced the CCE (Charge Collection Efficiency) parameter which is defined as a ratio of charge induced at electrodes and charge deposited inside the detector volume. This parameter is a common and useful measurement of charge transport performance in semiconductor detectors, and will be often used in the experimental results of this work. For sufficiently large electric fields, CCE is typically close to 100%, for detectors made of high quality single-crystal CVD diamond. However at lower electric fields, drift time of charge carriers can become comparable to their mean lifetime (which is a free flight time, determined by the statistical probability of capture on electrically active traps present in the crystal lattice). Therefore CCE value can be used to quantify charge transport and consequently crystal quality of diamond material used for detector assembly.

Equation 4.5, that represents the charge induced in the detector after ionization in the vicinity of one of electrodes, is called Hecht's equation [103]. By measuring CCE at different applied

electric fields, one can obtain the mobility-lifetime product as a fitting parameter of the equation to the measured values. In the first approximation, $\mu\tau$ product can be considered as constant, even-though effective mobility scales with electric field (see subsection 3.2.1), and only zero-field mobility is actually a constant.

Graphical representation of the Hecht equation is shown in Figure 4.5. $CCE(E)$ was evaluated for a range of electric fields $E = 0 - 2\,\mathrm{V}/\mu\mathrm{m}$, and for two different semiconductor thicknesses and two different mobility-lifetime products to test the influence of these parameters on the detector behavior. We can see that CCE reaches 100% with varying rapidness, but for the combination of $\mu\tau = 10^3 \mu\mathrm{m}^2/\mathrm{V}$ and thickness $d = 500\,\mu\mathrm{m}$, full CCE is not reached in the covered electric field range that is typical for diamond detector operation. This case is representative of a device with high homogeneous distribution of traps in the bulk that are limiting the lifetime of charge carriers, and thus affecting charge collection efficiency.
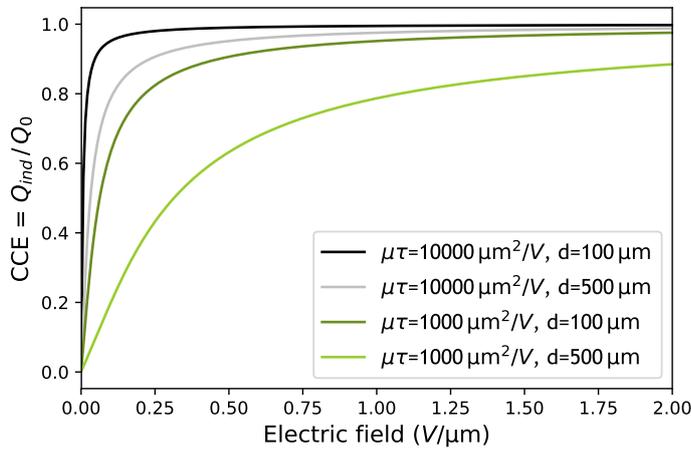

Figure 4.5: Plot of equation 4.5, representing CCE as a function of electric field. Different values of semiconductor thickness d and mobility-lifetime product $\mu\tau$ were used to evaluate their influence on the behavior (namely: $d = 100, 500\,\mu\mathrm{m}$, and $\mu\tau = 10^4, 10^3 \mu\mathrm{m}^2/\mathrm{V}$). CCE does not reach 100% in a displayed range of electric fields for the case of thicker semiconductor and lower $\mu\tau$ product.

Hecht equation will be used to fit the experimental data of charge collected at different electric fields, induced by shallow penetrating ion beams, so that only one carrier type will be dominating induced signal, and whose properties can than be extracted from the fit.

4.3 Charge transient spectroscopy

4.3.1 Thermally induced charge detrapping

Under equilibrium conditions the trapping process self-balances with the release process in SRH statistics. If we consider trapping level near the conduction band, that is trapping and releasing conduction electrons, this balance principle requires that the emission rate equals the trapping rate, or, using equations from the section 3.3.3:

$$e_{no}n_{to} = \sigma_n v_{th} n_o p_{to} = \sigma_n v_{th} n_o (N_t - n_{to}),\tag{4.6}$$

here the subscript "o" stands for equilibrium. n_o is the density of conduction electrons, and $p_t o$ ($n_t o$) is the density of impurities occupied by holes (electrons), and total impurity density $N_t = n_{to} + p_{to}$, under equilibrium conditions. n_o and n_{to} are defined as [104, p. 260]:

$$n_o = n_i \exp\left(\frac{E_f - E_i}{k_B T}\right) , \tag{4.7}$$

$$n_{to} = \frac{N_t}{1 + \exp((E_t - E_f)/k_B T)} . \tag{4.8}$$

More information about the definition of Fermi energy level, E_f, intrinsic energy level, E_i and intrinsic concentration, n_i, can be found in any classical book on semiconductor physics, for example [17, 52, 53].

Combining equations 4.6, 4.7 and 4.8, results in the following expression for the emission coefficient:

$$e_{no} = \sigma_n v_{th} n_i \exp\left(\frac{E_i - E_t}{k_B T}\right) . \tag{4.9}$$

Then, an assumption is made that the emission and capture coefficients outside equilibrium remain equal to their equilibrium values. This assumption should be valid as long as the conduction or valence band densities do not change significantly, and if the thermal energy remains a dominant contribution that induces releasing of the carriers from the traps. Electric field can be the other factor that provides energy for detrapping to charge carriers during detector operation. As an example, the influence of electric field was investigated for the gold acceptor level in silicon: the field dependence of the emission coefficient was found to be negligible, for fields up to 1 V/μm; and only for field values reaching around 10 V/μm, emission begins to increase noticeably [105]. A more general conclusion can be drawn from that: *field assisted detrapping can probably be neglected in favour of thermally induced detrapping* for typical donor and acceptor levels in semiconductors, during operation under weak and moderate electric fields.

Using this assumption, we can rewrite equation 4.9, dropping the "o" subscript for equilibrium. Furthermore, for electrons, we can use the fact that the energy needed for emission from the trap level to band minimum is $E_c - E_t$, and that intrinsic concentration n_i becomes the effective density of states in the conduction band N_c. Also, at this point, definition of the electron detrapping time $\tau_D^e = 1/e_n$ can be introduced, and we have:

$$\tau_D^e = \frac{1}{e_n} = \frac{\exp\left((E_c - E_t)/k_B T\right)}{\sigma_n v_{th} N_c} . \tag{4.10}$$

Effective density of states in the conduction band is:

$$N_c = 2 \left(\frac{2\pi m_e k_B T}{h^2} \right)^{3/2} \tag{4.11}$$

where m_e is the effective density-of-state mass for electrons. Thermal velocity (see subsection 3.2.1) is $v_{th} = \sqrt{3 k_B T / m_e}$. Injecting this into the expression for detrapping time, we get the following refined result:

$$\tau_D^e = \frac{1}{T^2} \frac{\exp\left((E_c - E_t)/k_B T\right)}{\gamma_n \sigma_n} . \tag{4.12}$$

Factor $\gamma_n = 3.25 \times 10^{21} (m_n/m_o) \, \mathrm{cm^{-2} s^{-1} K^{-2}}$ depends only on the electron effective mass.

Analogous procedure leads to the expression for detrapping time constant for a hole trap:

$$\tau_D^h = \frac{1}{T^2} \frac{\exp\left((E_t - E_v)/k_B T\right)}{\gamma_p \sigma_p} . \tag{4.13}$$
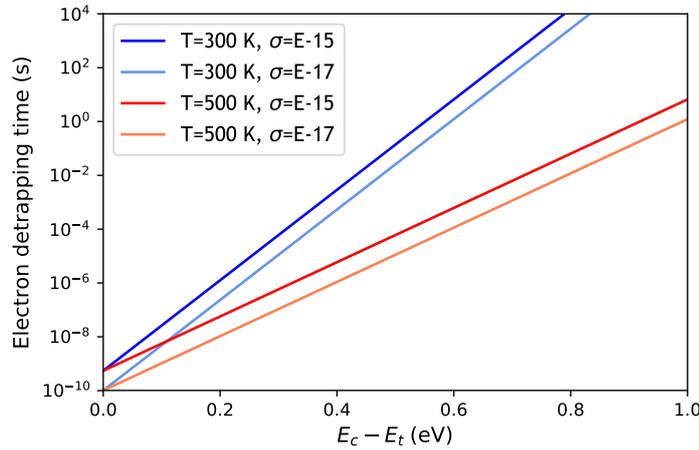

Figure 4.6: Electron detrapping time constant, evaluated using equation 4.12, as a function of trap energy position with respect to the conduction band minimum. Detrapping time was calculated for two different temperatures: 300 K and 500 K, and two capture cross-sections: $\sigma_n = 10^{-15}$ cm^2 and $\sigma_n = 10^{-17}$ cm^2.

Detrapping time constant, from the equation 4.12 is plotted as a function of $\Delta E = E_c - E_t$ (trap energy level in respect of the conduction band minimum) in Figure 4.6. Detrapping time was evaluated for two different temperatures (300 K and 500 K), and two different capture cross sections (differing two orders of magnitude). It can be seen that a higher cross section increases detrapping time one order of magnitude regardless of temperature or the trapping level energy position. Furthermore, the detrapping time strongly depends on the temperature. For the same energy level, detrapping time is shorter for higher of the two shown temperatures, and this difference is more pronounced for the traps with energy levels deeper in the band-gap. For a trapping level at $\Delta E = 0.4$ eV, and a cross-section of $\sigma_n = 10^{-15}$ cm^2, expected detrapping time decreases from $\approx 10^{-3}$ s at 300 K to $\approx 10^{-6}$ s at temperature of 500 K. For a deep level at $\Delta E = 0.8$ eV, these values change to 10^4 s and 10^{-2} s respectively.

In a charge-sensitive signal processing electronic chain, the detector is coupled to a charge-sensitive preamplifier, and shaping amplifier. Typical integration times in shaping amplifier are $\sim 1 - 10\,\mu$s. This would indicate that deep level detrapping constant, estimated from the data
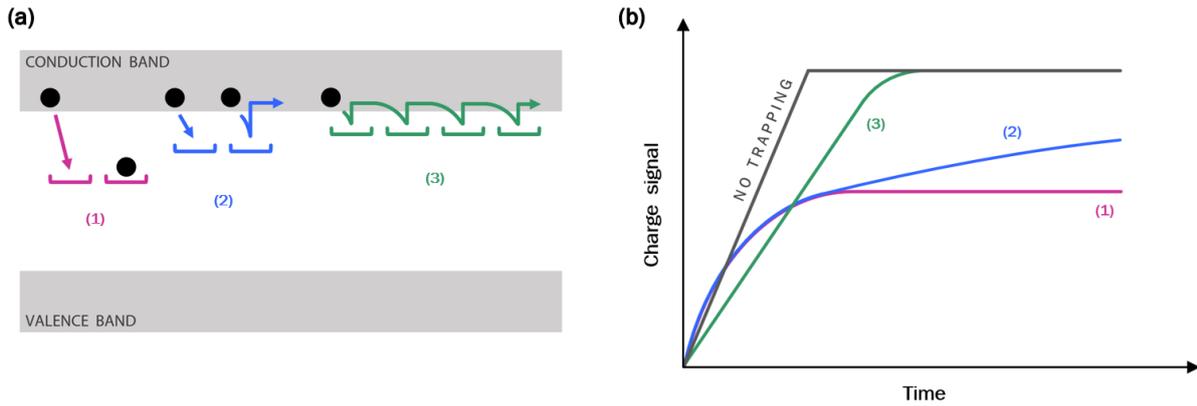
Figure 4.7: **(a)** Schematic representation of trapping-detrapping process for electrons on traps near the conduction band edge: 1) Deep level, 2) Trap level between shallow and deep, 3) Shallow level. **(b)** Time evolution of collected charge, induced due to electron drift, taking into account trapping at different trap levels from the Figure (a). *Adapted from [106, p. 255]*

in Figure 4.6 will have a strong influence on the amount of collected charge depending on the temperature during collection.

Schematic representation of trapping-detrapping process for a deep trap, intermediate trap, and a shallow trap level, are displayed in Figure 4.7-(a), while the corresponding collected charge signal in time domain, for these three different trapping situations, is shown in Figure 4.7-(b). Charge trapped in deep levels will remain there for a time period orders of magnitude longer than charge trapped at shallow levels. Therefore deep trapped charge is more likely to be recombined during trapping period by an opposing carrier, and can be considered as lost. On the other hand, almost all charge trapped in shallow levels will return to conduction band, after relevant time has passed. Using information contained in transient charge signals we can observe the detrapping recovery trend, and extract detrapping time constant. By observing charge transients at different temperatures, equation 4.12 or 4.13 can be used to model temperature behavior and to extract activation energy of the trap. Described procedure is the basis of the Charge Transient Spectroscopy (QTS), or, Charge Deep Level Transient Spectroscopy (Q-DLTS) technique.

4.4 Transient Current Technique

Experimental set-up

Signal of the detector was processed with a broadband current-sensitive amplifier. This amplifier actually converts instantaneous current to a voltage signal, so it is also current-to-voltage converter. However, since it is operated with known gain, voltage is easily recalculated in analysis in current units. Broadband amplifiers are designed to work with fast signals, that is with fast response detectors. DBA-IV amplifier (supplied by *Micron Semiconductor Ltd.*) that was used

in this study, was developed specifically for diamond detectors [107]. It has 2 GHz bandwidth, and 50 Ω impedance.
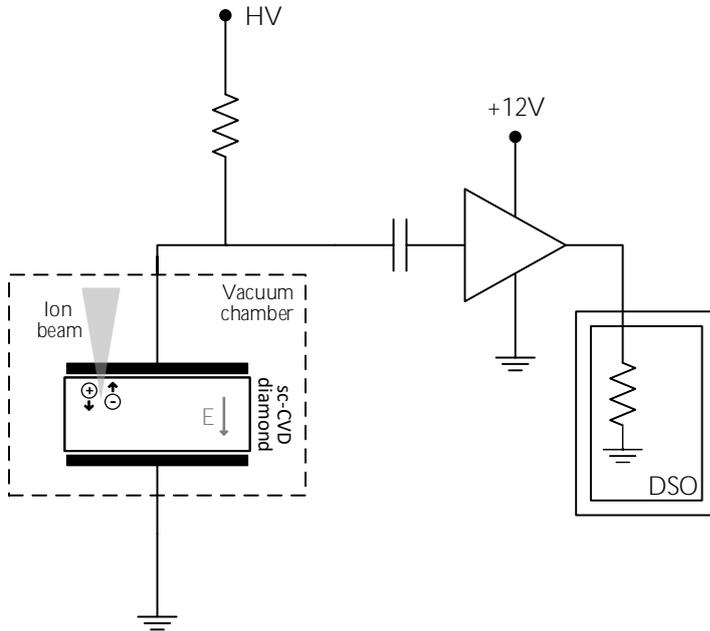

Figure 4.8: Schematics of the electronic chain for transient current technique measurements. Detector was AC coupled to the input of the broadband amplifier. Current pulses are recorded on a fast digital oscilloscope (DSO). Good electrostatic shielding was ensured to minimise noise pickup in the processing line.

Electronic chain for the transient current technique (TCT) setup is shown schematically in Figure 4.8. Detector signal was collected from the top electrode (where the ion beam penetrates the device), while bottom electrode is grounded. Signal is further processed via shielded cable and AC coupled to the input of the amplifier. Therefore, DC component of the signal is filtered out before reaching the amplifying electronics. After this, signal is fed to a fast digital storage oscilloscope (DSO), *LeCroy WaveMaster 8500A*, with 20 GS/s and 5 GHz analog bandwidth.

Relevant time constants in transient signal

Transient current signals read-out from diamond detector can be used to monitor charge transport properties during carrier drift in diamond bulk. Since transport time windows are on the order of nanoseconds, and rising and trailing edges are on the order of picoseconds, for good results, signal needs to be processed so that initial time structure fidelity is preserved as much as possible. First limiting factor is bandwidth (BW) bottleneck of 2 GHz, which limits the measured rise time to approximately:

$$t(10\% - 90\%) = 0.35/\text{BW} \approx 180\,\text{ps}\,.$$

Furthermore, since diamond with parallel plate electrodes has to be considered as a capacitor, fast components of the signal will be masked by the RC constant. This is a crucial factor that prevented us from using TCT technique with thin diamond detector. We had at our disposal for

this work two devices, made from 65 μm and 500 μm thick diamond detectors, with estimated τ_{RC} constants as:

$$\tau(65\,\mu m) \approx 350\,\text{ps} \quad \text{and} \quad \tau(500\,\mu m) \approx 20\,\text{ps}\,.$$

However, it is likely that actual RC time constants are higher due to parasitic capacitance components in the circuit. The capacitance of the overall circuit with thick crystal, up to the input of the broadband amplifier was measured as $C_{\text{tot}} = 2\,\text{pF}$, which would correspond to the $\tau_{\text{tot}}(500\,\mu m) = 100\,\text{ps}$. This is 5 times higher than estimated. Now, expected transit time, at electric field of the order of 1 V/μm, which is common for detector operation, for thin diamond is no more than 2 ns, and for thicker diamond is longer than 10 ns. Therefore signal shape will be much better preserved for thicker diamond, and data extracted from transient current can be used with confidence.

4.5 Development of the high temperature setup

4.5.1 Overview of diamond detector operation at elevated temperatures

The charge transport properties of diamond and its ability to operate as a radiation detector at high temperatures have been studied and described in a number of papers in recent decades, with noticeably increased interest in the last few years. Important pioneering experimental work [13, 55, 108] was performed in the 1980s by a research group that used natural diamonds as detectors for investigation of electron and hole transport at temperatures up to 700 K (the temperature dependence of mobility and free drift time was reported), as well as spectroscopy performance to α-source radiation. It was found that the pulse-height-spectrum (PHS) degrades as temperature approaches 500 K, which was determined as operating limit. Most subsequent work investigating high-temperature performance of diamond detectors has used similar experimental conditions: devices were exposed to alpha particles, neutrons or gama-rays to induce signal that was processed in a pulse (spectroscopy mode) to obtain PHS.

In recent years, several groups have studied the effects of temperature on detectors developed from artificial single-crystal diamonds [19, 20, 21, 109, 110, 111, 112, 113]. In some cases, degradation of signal properties started at temperatures as low as 400 K, which rendered detector inoperable for spectroscopy. The highest reported spectroscopy temperature limit of 570 K was reported in 2017 [111], using a sc-CVD diamond detector. A review article [114] from 2021 gives a more complete overview of available literature on the topic of high-temperature diamond detectors, with deeper insights of technical aspects in various works. Summarizing the results from different works is not easy because the data are obtained with diamond samples of different qualities, geometries, electrical contacts and detector housings. Such inconsistencies pose a significant challenge for further investigations as results may not be reproducible. This

in turn affects the next stage of detector development for practical use in harsh environments which are more restrictive than laboratory conditions. Better understanding of whether the effects of elevated temperature occur due to intrinsic limits of the used diamond material or due to technical limitations of metallization or detector housing is crucial.

Intrinsic limits of the diamond material are determined by the presence and quantity of impurities in the crystal lattice. Temperature effect on charge transport and defect dynamics can be tremendously difficult to understand and quantify. At elevated temperatures impurity atoms (as well as self interstitials and vacancies) can become mobile which will lead to formation of new shallow or deep traps. Furthermore, trapping/detrapping statistics is strongly influenced by the temperature, as emission and capture rates have an exponential dependance on temperature. Shallow trapping levels will be continuously emptied and deep levels can be activated. For example, temperature activation of several hole traps with E_A in the range 0.9–1.6 eV was investigated in [115], showing that trapping levels at around 1 eV became active at temperatures around 500 K.

From this we can further conclude that buildup or release of space charge (trapped charge carriers) will also change with temperature - polarization effect is in fact the most mentioned negative phenomena affecting detector performance at high temperatures. However, other, more complex and interrelated effects based on trapping/detrapping dynamics often need to be considered and better understood when interpreting charge transport results.

To conclude, the interplay of technical inconsistencies and variations in crystal quality in previously published papers limit the possibility of a systematic review of the effects of high temperature on diamond radiation detection. The design of our experimental setup and procedure to mitigate some of the aforementioned problems, and consequently help us gain new information and insight into the charge transport properties in CVD diamond under conditions of high radiation and elevated temperatures, is described in the following subsection.

4.5.2 Realisation of detectors and experimental setup

Development of the experimental procedure for testing diamond detectors under simultaneous exposure to high temperatures and ion beam irradiation proved to be a challenging task. During the development of the experimental setup, a goal was set to achieve operation under temperatures as high as possible, in order to push the limits of previous investigations. Two critical technical developments have been realized for this purpose: a) heating stage for the microprobe vacuum chamber, b) thermally resilient detector housing.

Heating stage for the vacuum chamber

The heating stage for the vacuum chamber have been developed for the specific experimental needs of this work. The setup was designed to meet the following criteria:

- To be compatible with the existing chamber sample holder and manipulator
- To minimize the heat transfer to nearby components
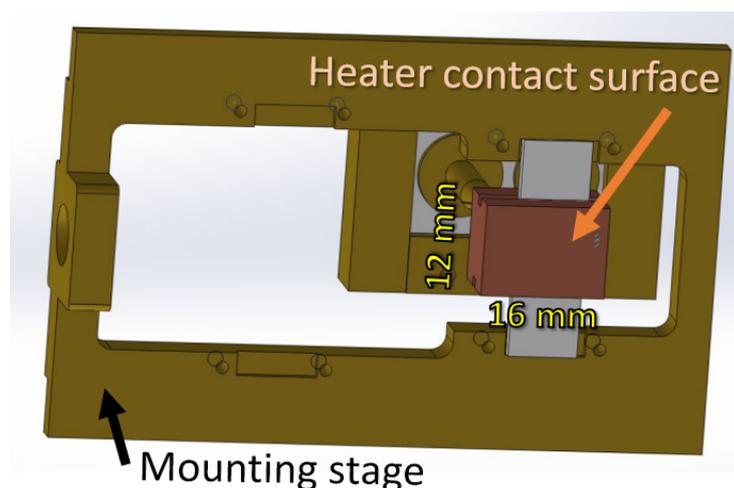- To be able to operate under high-vacuum condition, $\sim 10^{-7}$ mbar

Figure 4.9: 3D model of the heater stage. Detector is mounted on the heating element made from copper. Copper block is thermally isolated from the mounting stage that mechanically connects the heater to the microprobe sample holder.

The heating stage was designed and constructed locally, in the mechanical workshop of the accelerator facility. 3D model of the setup is shown in Figure 4.9. Current runs through the copper mass which acts as a resistive heater. Current is applied via programmable power supply unit. Heating element is held in place by two ceramic bars fixed on the mounting stage, and that also provide thermal isolation preventing the heat spread from copper to other components that might be placed on the mounting stage. Maximum temperature that can be reached and maintained for longer periods (several hours) by this setup in the vacuum conditions of the microprobe chamber is around 900 °C. In this work temperatures up to 500 °C were applied.

sc-CVD diamond crystals and electrode deposition

Two diamond crystals were used for radiation detection. Both crystals were procured from the *Element Six, Ltd.*, which produces synthetic, CVD grown, diamonds for specific needs in industry and science. Their highest purity line of crystals, so called electronic grade (EG) diamonds, offer guaranteed maximum impurity concentration of nitrogen and boron below few ppb-s ($[N]_s^0 < 5$ ppb, $[B] < 0.5$ ppb) [116]. This, at a time of writing, was the best quality offered as a commercial product on a market. Crystals were grown in MWPACVD reactors (see section 2.4 for more details), via homoepitaxy to form single-crystal material. Growth direction is along <100> crystal axis. Crystals from this manufacturer are commonly used for diamond-based electronic devices. Several studies have already been made in last 15 years

Table 4.1: List of important information about detectors D1 and D2.

Detector	Thickness	Electrode	Electrode area	Diamond	Measurements
D1	65 μm	Tungsten	$3 \times 3\,\text{mm}^2$	sc-CVD, EG	IBIC, QTS, Rad. hardness
D2	500 μm	Tungsten	$1.5 \times 1.5\,\text{mm}^2$	sc-CVD, EG	IBIC, TCT, Polarization

with quite comprehensive overview of the crystal-quality performance of this diamond material [36, 117, 118, 119, 120]. Taking that into consideration, no additional quality study was performed in the framework of this work.

The main difference between the two used diamonds is their thickness. Since detectors were realized in a parallel-plate geometry, where electrodes are placed on opposing crystal faces, thickness here refers to the distance between electrodes. Thickness of one diamond was 65 μm, and of the other 500 μm. Thinner crystal was processed by *Almax easyLab Inc.* with laser slicing and mechanical polishing to the final thickness. On both crystals, tungsten electrodes were deposited using sputtering technique. Diamond metallization was performed by M. Pomorski at "Diamond Sensors Laboratory" at CEA-LIST institute in France. The detector made from thinner crystal will be named D1 and from thicker crystal D2. Some parameters of two metallized crystals are given for reference in table 4.1.

There are two main motivation factors for use of two detectors of different thicknesses. Overview of the previously published works seems to suggest that thinner diamond detectors have higher maximal operating temperature [114]. If deterioration of charge transport is caused by trapping of defects that are uniformly distributed in the crystal volume, larger thickness would be undesirable. Trapped carriers would lead to build-up of bulk space charge, that screens the electric field applied through electrodes (polarization effect). In such circumstances, the greater the spacing between electrodes, the stronger the screening effect would be. This would deteriorate charge collection. Also, any trapping can limit carriers free lifetime, so thinner crystals of the same quality should have better charge transport properties than thicker crystals.

Thermally resilient detector housing

In most of the previous investigations from the field of diamond employment in high-temperature radiation detection, little to no focus was put on ensuring thermal resilience of the electronic processing components. One research group has, however, reported on the development of a special diamond detector design for high temperatures [21, 112]. The device demonstrated stable response to radiation for temperatures up to 600 K. Figure 4.10-(a) displays schematically diamond detector with custom developed high-temperature housing, in the ion microprobe vac-

uum chamber with heating stage. Diamond with the deposited electrodes was mounted on a ceramic plate with printed golden conductive pads. One side of the detector, the back electrode, was glued directly to the pad using electrically conductive 'Silver Paste Plus' from the *SPI Supplies Division of Structure Probe, Inc.* Due to the high content of silver solids in the suspension, this paste is suitable for high temperatures. It also does not evaporate under vacuum conditions. The top electrode was connected to another golden pad via a thin gold wire. The wire end, which sits on the diamond electrode, was glued by hand under the microscope by applying a small amount of the conductive silver paste with a fine tip needle.
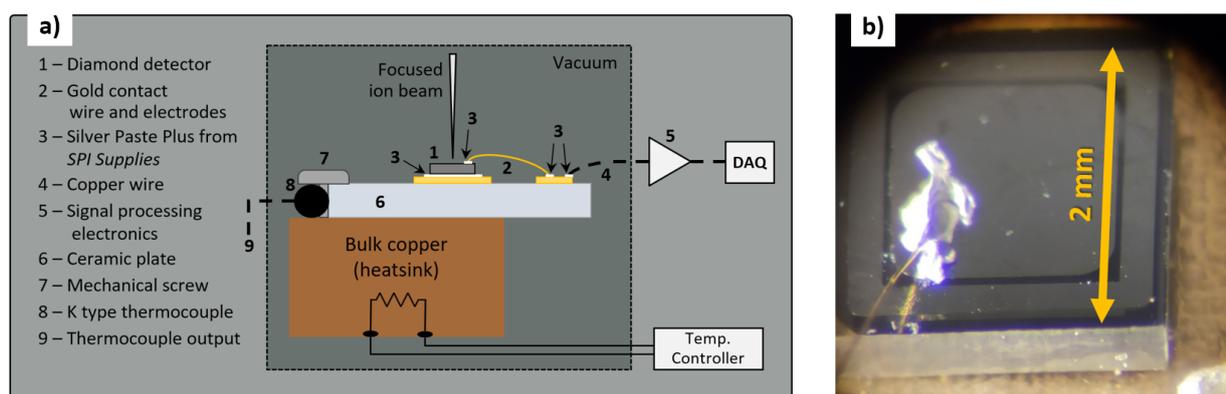

Figure 4.10: **(a)** Schematic view of the diamond detector with housing mounted on the heating setup in the ion microprobe vacuum chamber. Device is exposed to focused ion beam through the front electrode. **(b)** Connection of the gold wire on the top electrode of D2 detector with silver paste is seen under the microscope. Wire is used for signal processing and biasing. Back electrode is on the ground potential.

The microscope view of the top electrode after this step is shown in Figure 4.10-(b). Since this side of the detector was exposed to the ion beam, it was important to localize the spread of the paste on the surface, as this limits the clear area for ion probing. Attempts were also made to bond the gold wire to the tungsten electrode, but this was unsuccessful. The back of the ceramic plate was in direct contact with the surface of the heater. A stainless steel screw with a washer pressed the plate onto the heater to ensure good contact and stability. This is shown schematically in the figure. The washer was also holding the sensing head of the type K thermocouple. To ensure that the temperature at the measuring point matches the temperature on the actual diamond position, heat distribution on the front side of the detector mount was recorded with infrared camera (manufactured by *Optris*, model: PI 640i [121]). The test at various temperatures was performed in-air, and showed an average deviation between the thermocouple and camera reading of 5 K.

Infrared view of the detector D1 at one elevated temperature is shown in Figure 4.11. Inset of the Figure shows the regular photo of the same detector for comparison. Measuring point of thermocouple is positioned so that it is in direct contact both with the heater and one edge of
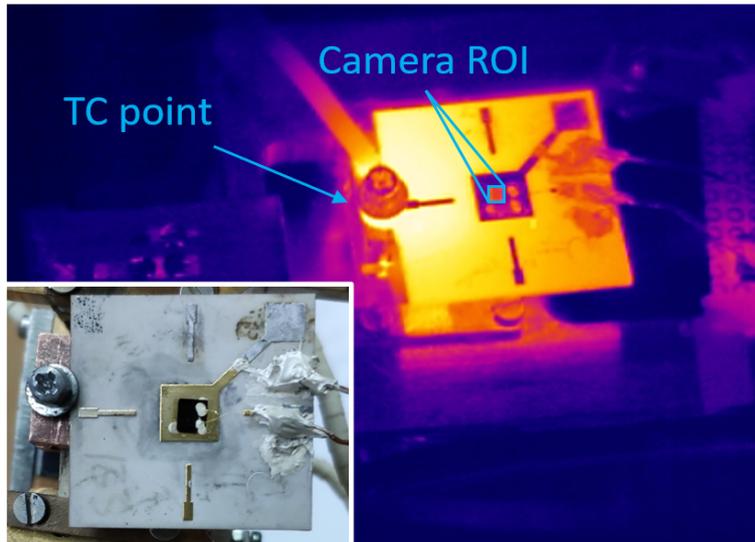
Figure 4.11: Heat distribution on the surface of D1 detector mount, recorded using IR camera. Heating element is below the PCB (bright square region), diamond is in the center of the PCB. Silver paste connections (two brighter spots) can be seen on the top electrode of diamond. TC is mechanically screwed on the heating stage so that it touches both the side of the PCB and copper heat-sink. Temperature of the diamond detector is readout as an average value from the annotated ROI (Region-Of-Interest).

the PCB. By looking back to Figure 4.10-(a), the center of the heating element is not aligned with the PCB, which is positioned towards the right side. This causes slight variation of the heat distribution on the PCB, which can be seen on the IR view, from left to right side. Heat distribution becomes uniform several minutes after the temperature of the TC is stabilized. This was taken into account during measurements. Temperature of the diamond was determined as the average value from the region of interest (ROI) marked with blue square on the surface of the front electrode. Please note here that metal electrodes appear darker on the image as metals have different emissivites[†] as compared to ceramic, however correct emissivity value was set in ROI for tungsten so that correct temperature is readout at that region.

[†]Emissivity describes effectiveness in emitting of thermal energy from the surface of the material.

5. Charge transport properties in pristine, unirradiated, diamond

5.1 Leakage current characteristics

The two diamond detectors used in the study were first characterized by the current-voltage dependence at various elevated temperatures. Leakage current was measured using a sensitive picoammeter with integrated voltage source, *Keithley, model 6487*. Detectors were heated to various elevated temperatures to observe the effects on current density. The results are shown in Figure 5.1 for D1 (thin) detector and in Figure 5.2 for D2 (thick) detector. The bias voltage is applied to the front electrodes of the devices, the same side that will be facing the ion beam in subsequent experiments. The rear electrode is grounded.
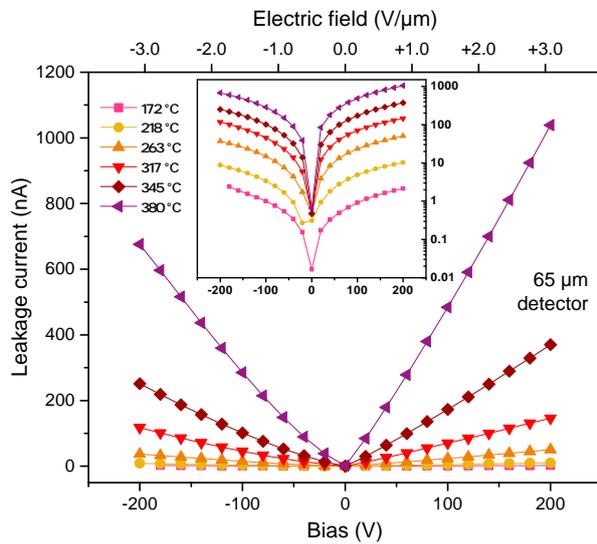
Figure 5.1: Leakage current - voltage measurements for D1 (thin) detector. Inset displays the same graph with logarithmic y-axis.
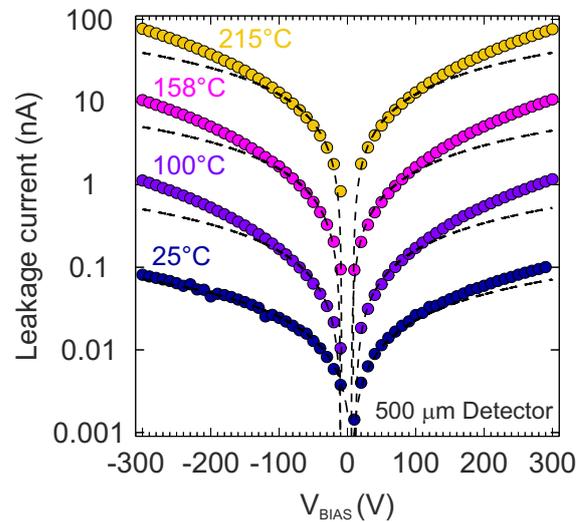
Figure 5.2: Leakage current - voltage measurements for D2 (thick) detector. Black dashed lines correspond to the best linear fit to data points.

As can be seen, the I-V characteristics for D1 detector are linear over the entire range of electric fields and temperatures covered in the measurement. The data are plotted in lin-lin and

lin-log (in the inset) scale. For the D2 detector, the I-V behavior is linear at low electric fields (up to about 0.2 V/μm), after which linearity is not fully preserved. Nevertheless, it can still probably be concluded that the near-linear dependence indicates that metal-semiconductor interface for tungsten-diamond is ohmic in nature, at least up to a certain limit of voltage potential difference. Discrepancies between the two devices can be prescribed to differences in contact quality, as the two detectors were not processed and metallized simultaneously.

Furthermore, conclusions can be made about the influence of temperature on intrinsic electronic properties, since the leakage current increases significantly with increasing temperature. At higher bias voltages, the difference in leakage current between highest measured temperature and the room temperature, for both detectors, is around 3 orders of magnitude. Number of free carriers that can be estimated from these results is much higher than expected for intrinsic diamond (see calculation in section 2.2.2). This certainly indicates that defects in the band-gap are assisting thermal promotion of electrons to the conduction band!

5.2   IBIC mapping

The detector under investigation is mounted in the ion microprobe vacuum chamber. The geometry of the setup is shown in Figure 5.3, along with the main components of the electronic processing chain.

The ions penetrate the front electrode of the device and ionize the underlying volume. The signal is read from the front electrode, while the rear electrode is grounded. The back side of the device is also in direct contact with the heating element of the sample holder.

When probing the detector with ions, the first step is to map the induced charge signal over a large area using IBIC microscopy. This enables us to quickly accumulate information about spatial uniformity of the signal and identify regions of interest for further investigation.

The left side of Figure 5.4 shows a pulse height spectrum (PHS) obtained when scanning a 2 MeV proton beam across the diamond detector D1 (thinner, 65 μm thick). The signal from the detector is first processed by the charge-sensitive preamplifier (CSP), ORTEC 142A, and then by the shaping amplifier ORTEC 570. CSP preserves the "shape" (time information) of the induced signal as it is amplified, while the shaping amplifier finds a maximum value of the input charge trace and outputs a Gaussian-like function whose peak amplitude is proportional to the original input maximum. In this way, the time structure is lost and only the charge amplitude is passed to the next element in the processing chain. Pulse-height-analysis is performed by a combination of ADC (Canberra8075 ADC) and the MCA integrated in the DAQ system. Each stored event corresponds to a charge (or deposited energy) induced due to the interactions of a single ion with the active volume of the device, as IBIC is a technique sensitive to single ions. 2 MeV protons have an average range of 24.5 μm in diamond (calculated using SRIM), therefore
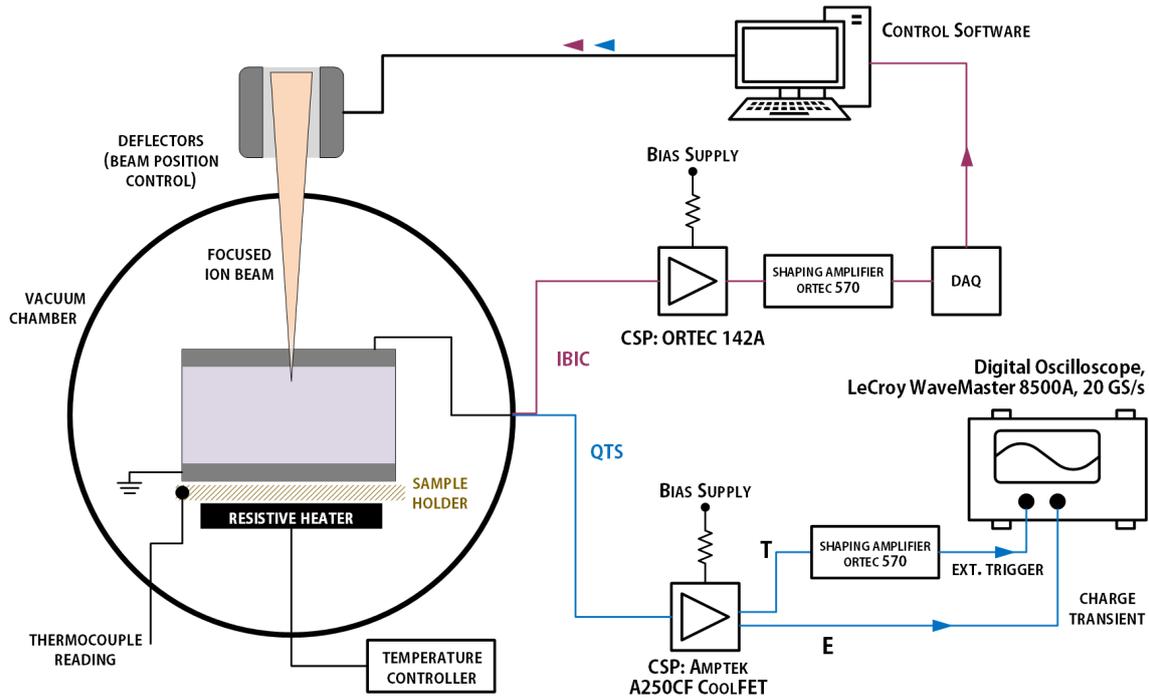
Figure 5.3: Schematic view of the detector in the ion microprobe vacuum chamber, together with main components of the electronic chains for IBIC and QTS signal processing and collection. Ions penetrate the device perpendicular to the front surface. After ionization, charge carriers drift to top and bottom electrodes. Top electrode is used to supply bias and readout the signal. Bottom electrode is grounded. For the analysis of charge traces (QTS technique), timing output (T) from the A250CF preamplifier was acting as an external trigger at the oscilloscope, while the traces were provided through the energy (E) output.

they deposit the full energy in the device. We can use this information to calibrate the charge height to energy units. We never assume the full charge collection efficiency in diamond, but rather use a cross calibration with a surface barrier silicon detector (using the same electronic chain). For the calibration, the e-h pair creation energy in silicon was assumed to be 3.62 eV, while the value used for diamond was 13 eV. In this way PHS can be represented with energy or collection efficiency units on the abscissa.

The PHS shown on the left of Figure 5.4 is a cumulative histogram of all of the events collected during scanning. Spatially resolved information can be plotted on the so-called IBIC map. The IBIC map corresponding to the shown spectrum is displayed on the right side of Figure 5.4. The charge amplitude is converted to CCE units and is represented by different colors, ranging from blue to red. It can be seen that the device exhibits very good spatial uniformity of the induced signal. A drop in CCE is visible near the electrode edges and around the contact points covered with silver paste (the ions loose energy as they penetrate through the paste). A smaller but noticeable drop in CCE is also observed in two irregularly shaped regions located on the right part of the map. These regions were also seen under the light microscopy image of the front electrode, so they are probably some sort of surface contamination on the
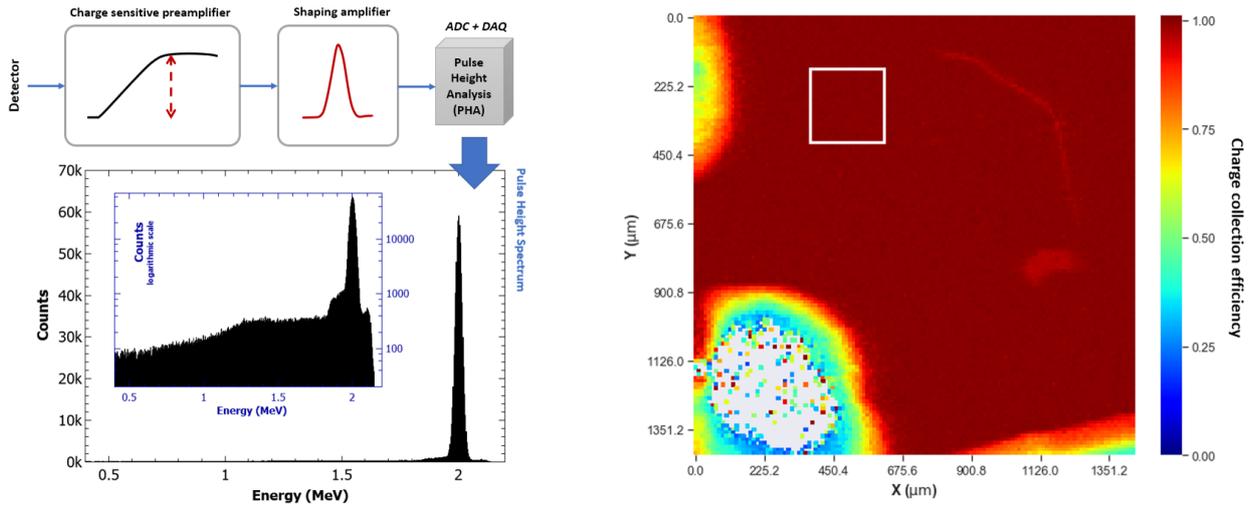
Figure 5.4: *(Left)* Schematics of signal shape as it is processed with IBIC electronic chain. Shaping amplifier receives signal from CSP and reads the amplitude (within shaping time window), output of the amplifier is a gaussian-like function with amplitude proportional to the original charge amplitude. Pulse height analysis is performed on the output of the amplifier, and spectrum is reconstructed. The shown spectrum was collected using signal induction with 2 MeV proton beam. *(Right)* IBIC map displays the spatial distribution of the collected events shown in the PHS. Color represents charge pulse height (normalized to CCE units). Electrode edge near the bottom of the map is visible. Also, two regions with low CCE on the left correspond to contact points with silver paste. Large areas of the device have uniform, full CCE, response. One such region of interest is marked with a white rectangle.

metal. Using the information from this map, ion beam was localized within the detector region marked with a white rectangle, chosen due to good uniformity of the induced signal, with full collection efficiency. Only signals induced within this region were used to further investigate properties of pristine diamond.

5.3 Charge collection efficiency at high temperatures

We will start the investigation of the influence of temperature on diamond detectors with the experimental scenario where IBIC method was used to estimate spectroscopic parameters at high temperatures. For this purpose, probing ions have to be stopped inside the detector, so that they deposit all initial energy to electron-hole pairs. Therefore, charge amplitude of the induced signal, will correspond to the ion energy. In this way IBIC PHA gives us both energy collection efficiency (equivalent to charge collection efficiency) and energy resolution (spectroscopic resolution) information. IBIC spectra, induced by proton irradiation, and collected at different temperatures for thin (D1) diamond detector were analyzed to extract this information. In addition, spectroscopy was performed with an α-source to emulate a scenario more appropriate to nuclear physics applications.

5.3.1 Results for D1 (thin) detector

Parts of this subsection have been previously published in author's research paper in 2020. [122]

A 2 MeV proton beam was used to induce charge in the 65 μm thick detector. Protons of this energy can be considered as intermediate probes for our detector, as they penetrate and ionize half of the total thickness of the device. Therefore, after ionization, both electron and hole drift will induce the response signal at the electrodes. The electric field applied to the detector at all measurements was $E = 0.092\,\text{V/µm}$. At this value of the field, charge collection reaches saturation, as the average drift time (flight time from the point of creation to the collecting electrode) of electrons and holes becomes shorter than their lifetime. This means that further increase of the field does not contribute to higher collection efficiency. At lower values, signal amplitude is lower due to insufficient field drift. Nevertheless, it is worth noting that usual operating values for diamond detectors are around $E = 1\,\text{V/µm}$ [123].
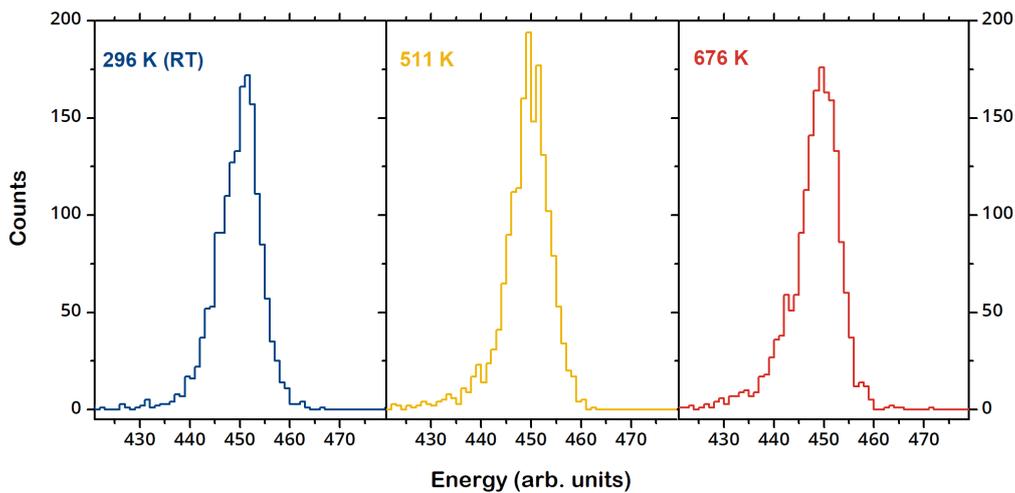
Figure 5.5: IBIC pulse-height spectra, collected at 3 different temperatures: 296 K, 511 K, 676 K, using D1 diamond detector, ionized with 2 MeV protons. Electric field of $E = 0.092\,\text{V/µm}$ was applied at all temperatures.

Selected IBIC pulse-height spectra, collected at various elevated temperatures (RT, 511 K and 676 K) in pristine diamond are displayed in Figure 5.5. All spectra follow a Gaussian distribution, and a fit was performed using Gauss function to extract the peak's energy position and the FWHM.

The results of the fitting were used to calculate CCE (from peak position) and spectroscopic resolution (from FWHM/peak-position) as a function of temperature. The results are shown in Figure 5.6, demonstrating excellent spectroscopic properties of the used detector in the entire temperature range from RT to 725 K.

Figure 5.6: *(Upper panel)* Charge collection efficiency of the pristine diamond for all temperatures between RT and 725 K. Data are calculated as the peak position of the IBIC PHS, induced by 2 MeV proton beam. Stable CCE is recorded for the whole covered temperature range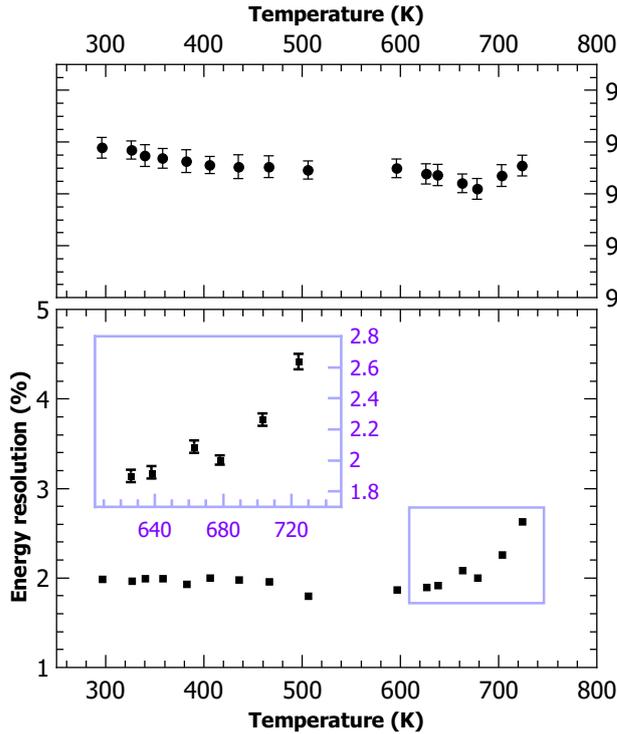. *(Lower panel)* Temperature dependence of the energy resolution. Data points are calculated from the FWHM of the IBIC PHS. 2% spectroscopic resolution starts deteriorating for temperatures above 700 K. This section of data is enlarged in the lavender colored inset of the plot. This data has been published in [122].

Discussion about proton-spectroscopy results

Appropriate spectroscopic behavior of a detector for nuclear applications usually understands that the energy distribution of the deposited radiation exhibits a distinct peak with a gaussian-like profile. Peak width denotes the spectroscopic resolution. Performance of the detector can be estimated by the $\Delta E/E$ ratio, and the stability of the operation is monitored by observing possible shifts in peak position or resolution degradation at prolonged irradiation times. This is particularly important for high-temperature spectroscopy experiments, where adverse thermal effect might not occur immediately, but can have a delayed manifestation as heat gradually builds-up and spreads to signal processing components that are in contact with the detector itself and whose electric performance can be affected by temperature change.

In the above presented results, CCE remains virtually constant over the entire covered temperature range. The measured value at room temperature was 95.8%, and the lowest value was 94.2% at 678 K.

The good collection efficiency obtained is also accompanied by a good spectroscopic energy resolution. The resolution remains constant, at about 2% (which corresponds to 40 keV FWHM) from RT to about 660 K. Above this temperature resolution starts degrading slightly, finishing at 2.6% for the IBIC spectrum induced at the highest recorded temperature (725 K). This value is still more than adequate for most applications. Potential degradation of spectral properties was also tested by long-term spectra accumulation, with irradiation times up to few tens of minutes at several elevated temperatures. It was confirmed that the peak position and

resolution remained unaffected.

It should be noted that both CCE and resolution depend on the optimization of electronic noise in the signal processing chain. This can be achieved primarily by using preamplifiers that provide better signal-to-noise ratios. An example is CSP with cooled FET at the input stage, which outperforms the more classic models, like ORTEC 142A CSP that was used in this measurement. Although such preamplifier was available to us, it can be considered as an extremely low-noise device, not standard for typical nuclear experiment settings. Therefore, the used electronic chain may not provide the best spectroscopic performance (in which CCE would edge more closely to 100%, and resolution would be improved), but is more comparable to the average laboratory and application conditions. To the best of our knowledge, at the time of writing, there was no other diamond-based radiation detector reported to have stable spectroscopic performance at temperatures as high as 725 K.

α-spectroscopic performance

In 2016, Steinegger et al. [110] reported results of α-spectroscopic performance with sc-CVD, 500 µm thick diamond detector. Alpha peaks were clearly resolved (with ≈ 50 keV FWHM for ^{239}Pu line) for temperatures up to 180 °C. At higher temperatures rapid deterioration of spectroscopic performance was observed together with increase in electronic noise. Kumer et al. [111] published results of the performance study of 300 µm thick detector exposed to α-radiation, for temperatures up to 570 K (300 °C), without degradation of resolution or peak position in the covered temperature range. 2% energy resolution for 5.5 MeV peak was reported.
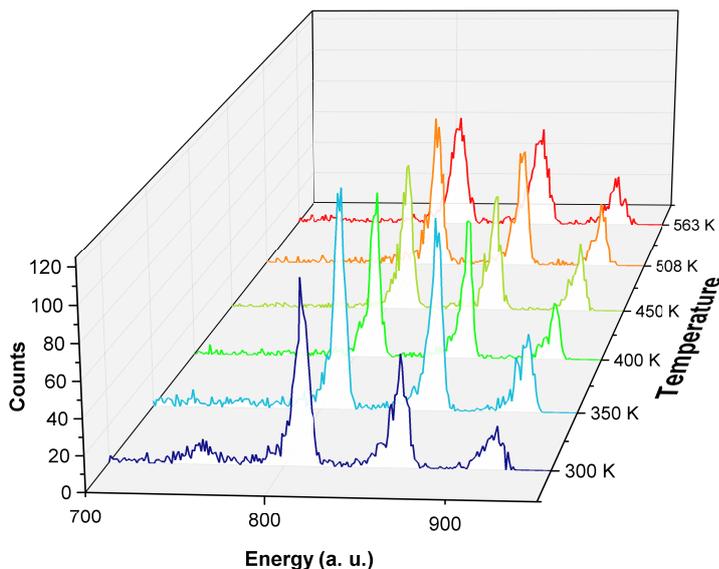
Figure 5.7: Counts-energy spectra collected by D1 detector at different elevated temperatures. Radiation was produced by a 3-radionuclide α-source (calibrated reference source). Note that statistics per data-set is low to minimize exposure of the source to heat.

D1 detector was also exposed to alpha radioisotope source radiation in order to replicate similar experimental scenario and compare results more directly with previous research. En-

ergy spectra were recorded at elevated temperatures up to 560 K (290 °C). Higher temperatures were avoided to prevent heat transfer to the α-source itself, which was positioned 1 cm from the detector, facing the front electrode. The source consisted of a mixture of 3 radionuclides (^{239}Pu, ^{241}Am, ^{244}Cm). The main lines of these components are: $E = 5.16, 5.5, 5.8$ MeV (each radionuclide emits several closely-valued energy lines, but the listed ones are statistically dominant) [124]. The obtained α-spectra are plotted in Figure 5.7. A spectroscopic resolution of about 1% is observed for the 5.16 MeV peak. Resolution and peak position remain stable with time, as the data acquisition took several hours. These results support the previously discussed excellent charge collection performance of the same detector during probing with MeV protons. A more comprehensive study can include probing with different ion species and energies relevant for nuclear applications, but as a proof-of-concept, published spectroscopy results are quite sufficient. Testing the response of the detector to neutron irradiation at elevated temperatures would be a next step toward device prototyping for practical applications, like the one for fusion reactor monitoring.

5.3.2 Results for D2 (thick) detector

D2 detector was also tested at high temperatures, in the same way as was done for the D1 detector. To induce signal in the detector at various elevated temperatures, proton beam of 2 MeV energy was used. Unfortunately, the results of this experiment are not relevant for energy spectroscopy applications, as the average recorded charge amplitude is not stable, but degrades on time scales as short as few seconds (corresponding to an accumulation of a $\sim 100\,\mathrm{cm}^{-2}$ ion fluence), after the device is exposed to a probing ion beam. This effect occurs due to bulidup of space charge (polarization effect) in the crystal lattice. Investigation of the polarization at different temperatures is discussed separately in section 5.6. However, as polarization effect may significantly reduce application possibilities of diamond detectors, here we discuss how the adverse effects of polarization can be mitigated. In the case of IBIC, irradiation conditions can be modified by lowering the ion rate and increasing the area where the detector area exposed to ions. In such conditions, local charge density is reduced, and the space charge has less impact on detector performance. Other depolarization techniques could also be exploited to restore the internal electric field in the detector, but none of these techniques represent relevant conditions in which continuous, long-term, energy spectroscopy experiments would be performed. Therefore, the results about the spectroscopic performance of D2 detector are not presented in this section.

Still, it can be said that the actual maximum operating temperature of the thick (D2) detector is much lower than that of the thin (D1) device. Temperatures of up to about 500 K (230 °C) were attainable. After that, signal properties quickly deteriorate as the electronic noise increases and the signal-to-noise ratio deteriorates. This is consistent with reports of other authors [110, 114],

in which systematically lower operating temperatures were reached for thicker diamond crystals.

This inverse proportionality of maximum achievable temperature and diamond thickness is not trivial to explain. As temperature increases charge carriers have lower drift velocity, which in turn increases the cross-section for capture on trapping centers. Any trapping related effect is more pronounced when separation between electrodes is larger, as electrons or holes lifetimes might not be long enough to reach them. It is not clear exactly which trapping related mechanisms come into play at elevated temperatures, and how defect dynamics (defect annealing and new complex formation) evolves in a certain temperature range. A more systematic study of crystal quality and detector thickness behavior at high temperatures is needed in order to understand underlying mechanics and to mitigate undesired thermal effects.

5.4   Mobility-Lifetime characterization

Parts of this section have been previously published in author's research paper in 2021. [125]

In section 4.2 it was demonstrated that for a specific case, when only one type of carriers is responsible for signal creation, the expression for the induced charge amplitude behaves according to the Hecht's equation:

$$Q_{ind} = Q_0 \frac{(\mu\tau)E}{d} \left(1 - e^{\frac{-d}{(\mu\tau)E}}\right), \tag{5.1}$$

where Q_0 is the charge injected by the ionizing radiation, d is the distance between electrodes, E is the electric field, and $\mu\tau$ is the mobility-lifetime product of the carrier responsible for signal induction. Induced charge, which is a function of the electric field, was calculated and plotted in Figure 4.5. It can be seen that after a strong increase at small values of the field, induced charge reaches saturation at higher fields and becomes near constant. In other words, when the electric field is sufficiently strong, drift time of carriers becomes shorter than their lifetime, and they successfully reach the opposing electrode.

This equation was used to extract mobility-lifetime product from the IBIC data. Short range ion beam (3 MeV He$^+$) was used to ionize the D1 detector volume. Since one type of charge carriers drifts to the top electrode (the one exposed to the ion beam) and the other type drifts to the opposite electrode, according to the Shockley-Ramo theorem, majority of the signal will come from the latter carrier type. Also, due to the Bragg-peak shape of the ionization profile (shown in lower panel of the Figure 6.4), maximum number of carriers will be created at depth of 5.7 μm between electrodes, therefore we can use a modified version of the Hecht's equation [126] to account for this:

$$CCE = \frac{Q_{ind}}{Q_0} = \frac{(\mu\tau)E}{d}\left(1 - e^{\frac{x-d}{(\mu\tau)E}}\right), \tag{5.2}$$

where x is the depth of maximum ionization. We have also used the fact that the ratio of induced and injected charge is charge collection efficiency. Since the bottom electrode is always grounded, by changing the bias voltage polarity from positive to negative, switch from dominantly hole drift to electron drift in the device can be achieved. In this way we are able to measure this dependency for both types of carriers. Due to the fact that the mobility depends on the crystalline direction, it should be noted here that in our geometry the charge carriers drift along the <100> crystalline direction, so the obtained mobility-lifetime values can be denoted as $\mu\tau_{<100>}$. As all the results of the $\mu\tau$ were measured along the same direction, <100>, its occurrence in the subscript will be omitted in further text. Data were obtained at multiple elevated temperatures ranging from RT to 725 K. Several sets of measured data of CCE vs electric field are displayed in Figure 5.8.
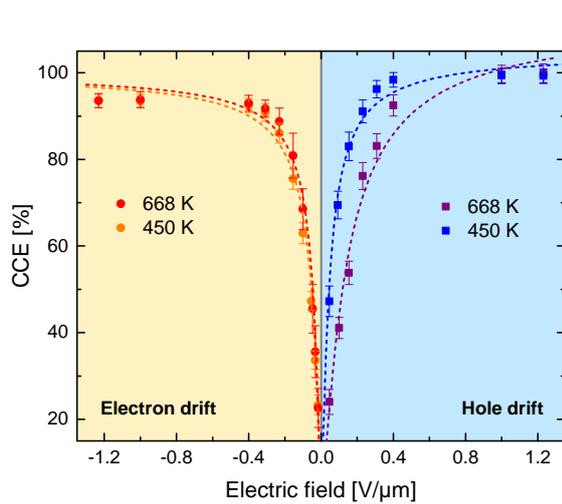

Figure 5.8: CCE as a function of applied electric field to the detector. Signal is induced either by electron or hole drift, after charge injection by 3 MeV He$^+$ ion beam. CCE data is displayed for two selected elevated temperatures, 450 K and 668 K, together with the results of nonlinear approximation according to equation 5.2 (dashed lines).
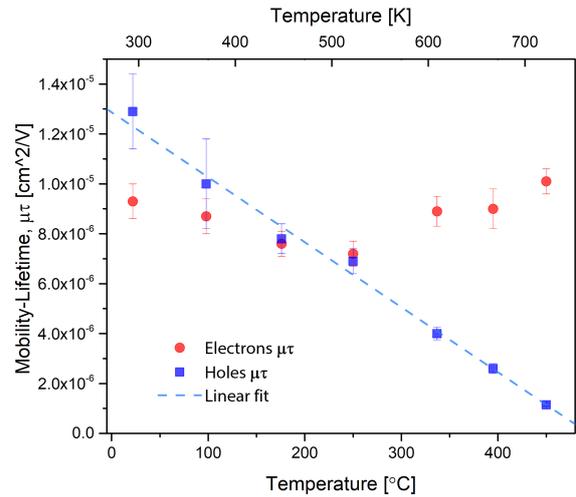
Figure 5.9: Mobility-lifetime product of both electrons and holes in pristine single crystal diamond, obtained as a result of approximation according to the Hecht's equation to the experimental data. $\mu\tau$ was measured for various elevated temperatures. Holes $\mu\tau$ exhibits linear decreasing trend with temperature.

All results of the fitting for electrons and holes are given in the Table 5.1. R^2 goodness-of-fit parameter is also listed*. The lowest R^2 is 0.97, indicating that the data are reasonably well approximated by the Hecht's model. However, some precaution needs to be taken before further analysis of the obtained values. First, the fidelity of the results could be higher if more

*Parameter is calculated as R^2 = 1 - (Residual Sum of Squares)/(Total Sum of Squares)

points were measured for each temperature. More importantly - mobility of the charge carriers at different electric fields is not constant, but varies non-linearly (see subsection 3.2.1). Therefore, the assumption of $\mu\tau$ as a fitting parameter of each CCE(E) curve is not exact, and the extracted values cannot be taken as material constants for CVD diamond. Furthermore, more complex models [127] based on the original Hecht equation have been developed to account for nonuniform electric field and space charge effects. Careful usage of such models can sometimes be beneficial for the fitting results, but this would incorporate non-physical parameters in the equation which usually complicates the interpretation of the results. For this reason, simple Hecht model was used in our data analysis. Even with such limitations posed on the extracted data, mobility-lifetime values can still be used to examine the effect of temperature on charge carrier transport, by comparing relative changes among them.

Table 5.1: Results of fitting the modified Hecht's equation to the CCE(E) dependencies, measured at different temperatures. Goodness-of-fit is evaluated through the R^2 parameter. R^2 value closer to 1 indicates that a greater proportion of variance is accounted for by the model. Instrumental weighting method was used to incorporate the uncertainty of measured data points.

Temperature (K)	294	370	448	522	610	667	722
$\mu\tau$ (elec.) $\left(\frac{cm^2}{V}\cdot 10^{-6}\right)$	9.3 ± 0.7	8.7 ± 0.7	7.6 ± 0.5	7.2 ± 0.5	8.9 ± 0.6	9.0 ± 0.8	10.1 ± 0.5
R^2	0.973	0.978	0.985	0.973	0.987	0.970	0.989
$\mu\tau$ (hole) $\left(\frac{cm^2}{V}\cdot 10^{-6}\right)$	12.9 ± 1.5	10 ± 2	7.8 ± 0.6	6.9 ± 0.5	4.0 ± 0.25	2.6 ± 0.2	1.15 ± 0.06
R^2	0.986	0.992	0.999	0.999	0.986	0.986	0.998

Results from the table 5.1 are plotted in Figure 5.9, where the temperature dependence of the $\mu\tau$ product can be seen. There is an overall decrease of the $\mu\tau$ value with temperature for holes, which changes one order of magnitude from the room temperature to 725 K. If we assume this trend to be linear, the rate of decrease is -2.6×10^{-8} cm^2 V^{-1}/K (indicated with a dashed line on the plot). For electrons, initial decreasing trend is stopped at around 520 K, after which mobility-lifetime seems to recover to higher values. However, this trend is less evident as comparing to a clear deteriorating behavior for holes.

Notably, mobility-lifetime estimates for diamond at high temperature seem to have been only published before for natural diamond [13] and in a thesis by A. Lohstroh [128] for pc-CVD diamond, and not for the high-purity synthetic diamond. Decreasing temperature behavior was measured in natural diamond for both electrons and holes [13]. This is expected, as the mobility of charge carriers scales negatively with temperature due to the increased scattering on phonons (see again Table 3.1). In our results, $\mu\tau$ data for electrons suggests that a drop in mobility is counterbalanced by an increase in the lifetime at temperatures above 520 K. This could be possible due to thermal activation of an electron trap at these temperatures, which would lead to the release of previously trapped electrons. Detrapping would improve effective lifetime of

carriers. However, this theory could not be ratified, as no detrapping was observed in charge traces collected at these temperatures in pristine diamond. More details on the investigation of detrapping effects will be given in section 6.2.

In conclusion, these results provide a very good insight into the properties of charge transport in CVD diamond. But, more studies and experimental data are needed to better understand the observed unbalanced behavior for holes and electrons with rising temperature. One possibility would be a direct measurement of charge carrier lifetimes.

5.5 Transient Current Technique (TCT) measurements

For the Transient Current Technique, broadband electronics is used to process the current signal from the diamond detector. A signal is induced due to drift of electrons and holes in the applied electric field between the electrodes. As it was already explained, to study the transport properties of a single charge carrier type, an ionization event needs to occur near one of the electrodes. Two ion beam species were therefore used to ionize detector D2: 8.2 MeV He^{2+} and 5 MeV He$^+$. The ionization profiles of these two ions in diamond are shown in Figure 5.10.
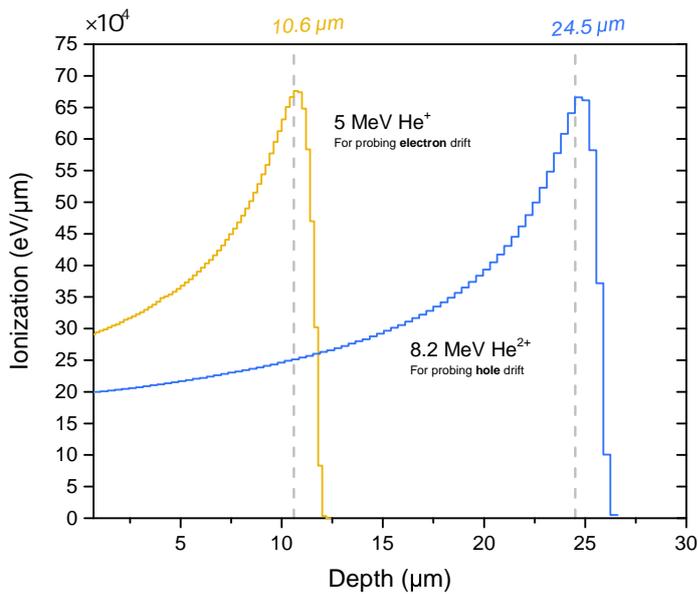
Figure 5.10: Ionization profile (electronic energy loss rate) of 5 MeV and 8.2 MeV He ions in diamond target, simulated with SRIM. Both profiles exhibit Bragg curve dependency on penetration depth, with peak ionization rate positions indicated on the plot with dashed vertical lines.

Experimental procedure and data processing

Individual current pulses were recorded in the oscilloscope memory. Each pulse was induced by a single ion impinging through the front electrode of the detector, and ionizing the volume along its penetration trajectory. In a typical scenario, the detector was heated to a certain temperature after which few minutes were taken for temperature stabilization. Then, the bias voltage was applied to electrodes. At this point, ion beam valve was opened, and ionization processes

started. In order to minimize the ionization density, which can lead to polarization effects, a very low particle rate was used, around 10 cps, and the beam was also scanned over a small area of around $50 \times 50\,\mu m^2$. However, as it will be explained, the influence of polarization on pulse shape was nevertheless observed during the data analysis. Around 100 traces were recorded for every given pair of temperature and applied bias voltage. After this, offline analysis was performed in the following way: 20-30 traces were selected, baseline correction was performed (in the same way as in QTS analysis), and for some traces a small time shift was applied to correct for trigger jitter. This corrected data set was then averaged. An example of a data set with 20 individual traces, together with a resulting averaged pulse, is shown in a left panel of Figure 5.11.
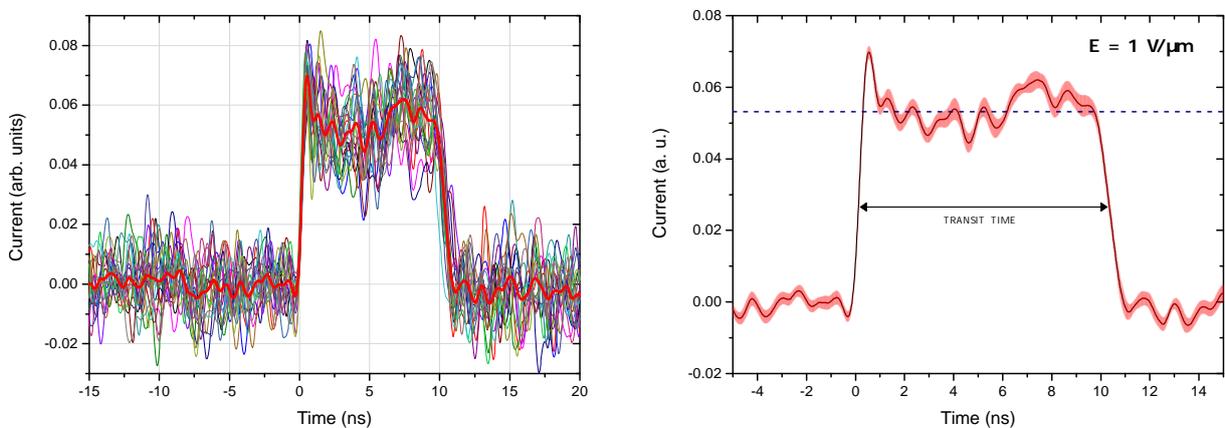

Figure 5.11: *(Left)* 20 current pulses recorded using TCT technique, induced by electron drift at 357 K. Applied electric field was $E = +1\,V/\mu m$. Bold red line represents an average of individual traces. This example is representative for data sets recorded at different temperatures and electric fields. *(Right)* An averaged transient current signal from the left plot is displayed together with standard deviation (red shading). Average value of the current amplitude during drift is calculated and marked with dashed line. This value is used to find FWHM of the signal, which corresponds to the average transit time of the carriers.

The right panel of the same figure displays only the averaged signal, together with standard uncertainties. The signal is induced due to drift of single type of carriers, that transverse a distance from the point of creation to the rear electrode. By using wideband processing electronics, very fast rising and falling edges of the current pulse were preserved and could be used to mark exact time points when the drift started and finished. Therefore, the FWHM of the pulse corresponds to the time-of-flight of a charge carrier drifting in the diamond volume.

Analysis of charge transport properties

Transient current signals induced either by hole or electron drift at different elevated temperatures, from RT to about 550 K, are displayed in Figure 5.12-**(a)**-**(b)**. The electric field applied during electron drift was $1\,V/\mu m$ (500 V bias), and during hole drift was $0.9\,V/\mu m$ (450 V bias).

Drift time was extracted from these traces and is shown in Figure 5.12-**(c)**-**(d)**. It can be seen that the drift time increases as temperature rises for both electrons and holes. Furthermore, for higher temperatures, gradual change of slope of a trailing edge is observed for holes, which can indicate that distribution of drift times of holes becomes larger. This effect is not observed for electron induced signals.

Carriers drift across the full detector thickness and are collected on the back electrode. For propagation of carriers at sufficiently large electric fields, as used in this experiment, it can be assumed that average drift distance is longer than detector thickness, so that most of electrons and holes reach the rear electrode. In such conditions, both drift time and trajectory length are known, and drift distance can be calculated as:

$$v_d = \frac{L}{t_d},$$
(5.3)

where L is the average drift length of electrons or holes. Since both used ion beams, that have been used, have a Bragg-peak ionization profile, most of the carriers are induced at the depth of maximum ionization. This depth (peak position) x_{peak} is, as estimated from SRIM simulations, at 11.8 μm for 5 MeV He$^+$ and at 25.6 μm for 8.2 MeV He^{2+} (also shown in Figure 5.10. Most probable drift length L can be calculated as: 500 μm - x_{peak}, since charge carriers drift from the point of origin to the back electrode. This gives: L(elec.) = 488.2 μm and L(holes) = 474.4 μm.

The drift velocity can now be plotted for different temperatures, Figure 5.12-**(e)**-**(f)**. This graph actually shows both velocity and the mobility value, since mobility is simply: $\mu = v/E$, and electric field was constant for all measured temperatures for either electrons or holes. Left axis of the plot is in velocity units (μm/ns), and right axis is in the mobility units (cm^2/Vs - squared centimeters per volt-second).

It should be noted again that the calculated mobility is the effective drift mobility of the carriers at the electric field $E = 1$ V/μm (electrons) or $E = 0.9$ V/μm (holes). Electrons and holes drift along the direction of the applied electric field, which points along the <100> crystalline direction. Therefore, the measured drift mobility of the charge carriers can be denoted as $\mu_{<100>}$, as mobility value depends on the direction of charge movement in respect to crystal lattice symmetry (however the subscript will be omitted, as all of the mobility results are measured for the same crystalline direction). As it was previously explained, mobility scales non-linearly with electric field in diamond. In fact, both electrons and holes achieve maximum mobility when no external field is present. Zero-field mobility is considered as a material constant, and can be extracted from the mobility-field dependence as a fitting parameter. Most of the previously reported mobility estimates for diamond have been obtained with this procedure [1, 56]. Unfortunately, in the used experimental settings it was not possible to collect TCT waveforms at low electric fields, as signal amplitude and shape profile were strongly affected
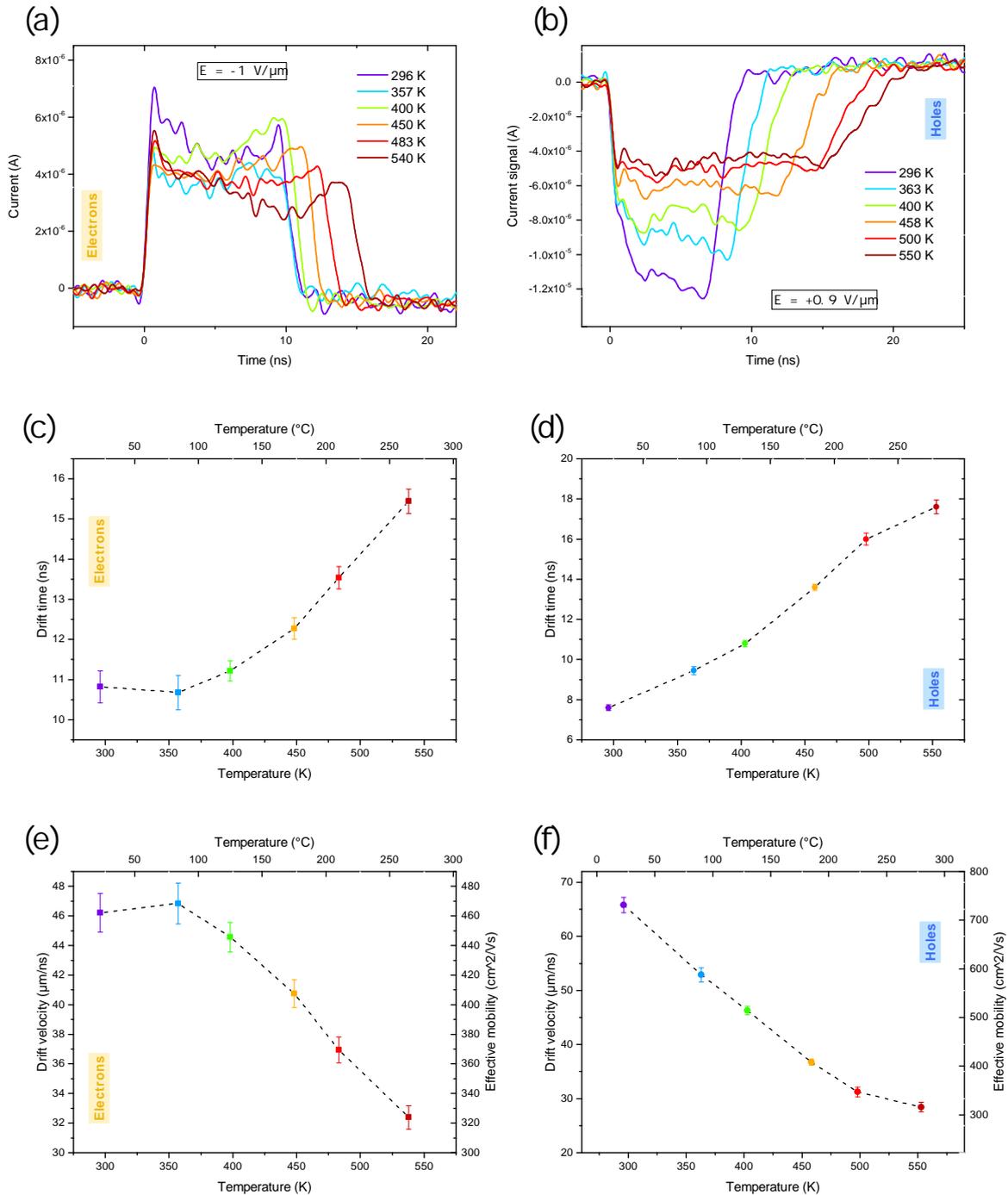
Figure 5.12: Averaged current pulses induced by electron drift **(a)**, or hole drift **(b)**, at various elevated temperatures. Electron signals were recorded for $E = 1\,\text{V/μm}$ ($U_{\text{bias}} = -500\,V$), hole signals for $E = 0.9\,\text{V/μm}$ ($U_{\text{bias}} = +450\,V$). Plots **(c)** and **(d)** show drift time of electrons and holes as a function of temperature. Drift time is calculated as a FWHM of TCT pulses. Plots **(e)** and **(f)** show velocity (and effective drift mobility) of carriers, calculated from the drift times. Dashed lines on plots **(c)-(f)** are drawn as visual guides.

by the background noise level.

Obtained effective drift mobility and drift velocity data can be used to analyse the influence of temperature on the charge transport properties. Drift mobility drops with rising temperature for both types of charge carriers. Rate of decrease is stronger for holes than for electrons. At room temperature, effective mobility was measured as 730 cm^2/Vs for holes, and around 450 cm^2/Vs, but they scale down to the approximately same value of 320 cm^2/Vs at 540 K (highest covered temperature). Similar, but slightly higher values (about 20% higher) were reported recently, where the drift velocity was estimated using TCT signals induced by α-radiation in sc-CVD diamond [113], for temperatures up to 480 K. Similarly, stronger rate of decrease of mobility with temperature was observed for holes.

Going back to results in figure 5.12-(e)-(f), it can be seen that measured drift velocity at first two temperatures for electrons is virtually the same, and only afterwards begins to decrease. For holes, highest two temperature points also exhibit very close value, that deviate from the previous temperature trend. As this seems to deviate from the expected trend, we attempted to check the fidelity of the results by integrating the area under the induced current curves to obtain total induced charge during transit time. Charge integral should remain constant for different temperatures, and deviation from this can indicate additional effects that influence charge transport and which should be taken into consideration.

In order to investigate total collected charge, one simply needs to integrate area under the current transient:

$$Q_{tct} = \int_{t_1}^{t_2} I_{tct}(t)\, \mathrm{d}t\,, \tag{5.4}$$

where integration limits t_1 and t_2 are time points determining the beginning of a rising edge and the end of a falling edge. The results of numerical integration are shown in Figure 5.13, both for holes and electrons. The trapezoidal rule was used for calculation.

Calculated charge, Q_{tct}, is displayed both in coulomb units and in CCE units. For this case, CCE was defined as a ratio of Q_{tct} and the charge induced by an ion. The latter is calculated by converting ion energy to deposited charge:

$$CCE_{tct} = \frac{Q_{tct}[C]}{(E_{ion}/E_{ehp}) \cdot 1.602 \times 10^{-19}[C]}\,. \tag{5.5}$$

Here we divided ion energy with pair-creation energy ($E_{ehp} = 13\,\mathrm{eV}$) to obtain statistically most likely number of created pairs, and multiplied this with elementary charge value to get total induced charge in divisor.

CCE units on plots displayed in Figure 5.13 are more useful since absolute charge units differ between electrons and holes due to the different ion energy being used for signal induction (5 MeV vs. 8.2 MeV).

First observation that can be made is that the average value of CCE for both cases is just below
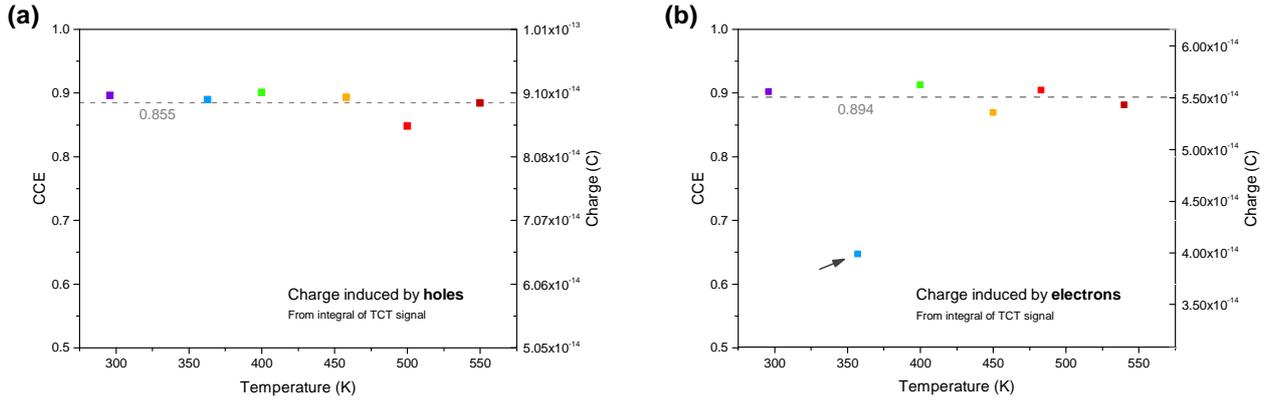
Figure 5.13: Charge induced by: **(a)** holes, or **(b)** electrons drift as a function of temperature, obtained as integrated area under transient current traces. Right axis on each plot is shown in coulombs (C), while the left axis is recalculated as a charge collection efficiency. Horizontal line displays average CCE for different temperatures. For electrons, charge collected at 363 K deviates significantly from other points, and is excluded from average value.

90%. Therefore, it can be suspected that some charge was trapped and lost during the drift. CCE value might be also underestimated, as the broadband electronics have a worse signal-to-noise performance than the charge sensing electronics, so that IBIC PHA might extract more charge. Also, in charge sensitive electronic chain, charge integration time is significantly longer than in the TCT technique (microseconds against nanoseconds).

Other observation that can be made from the results is that, for electrons, charge induced at 363 K is significantly lower from the average value. This suggests that the TCT shape for this temperature is less reliable for drift time extraction. The reason of such drop in electron drift induced charge at this temperature cannot be deduced from these data alone. The shallow trap could be thermally activated at these temperatures and start releasing captured charge with some detrapping time constant. Delayed charge transport would give signal collection at times longer than transit window. It can in fact be seen that corresponding electron pulse at 363 K has a tail-like shape outside the main pulse, that is slightly offset above other traces.

For holes, there are no charge values that deviate significantly from the average value. However, the charge collected at 500 K is somewhat lower than at other temperatures, which could affect the drift time and velocity values.

5.6 Polarization effect

An additional brief analysis of the TCT pulse shapes can give us more information about the charge transport during the transit time. Since the transient current signal is induced by the charge carrier drift through the space between the electrodes, the current at any time during this drift is proportional to the instantaneous drift velocity of carriers. This drift velocity is directly

proportional to the local value of the electric field at the carrier's current location in space. Thus, we have: $I_{ind.} \sim v_{drift} \sim E_{local}$. Consequently, the TCT shape in the time domain, $I(t)$, can be used to analyze the electric field profile in spatial coordinate $E(x)$ (where x is the distance between electrodes aligned along the electric field direction). In the subsection 3.2.2, where the Shockley-Ramo theorem was used to model the electric field in a parallel-plate geometry, we concluded that for an intrinsic diamond, the electric field has a constant value throughout the volume, so that the transient current pulse should have flat-top shape profile. A possible deviation from this profile indicates trapping effects and deterioration of the constant field due to space charge effects.

By looking at TCT waveforms induced by the hole drift, shown in Figure 5.12-(b), it can be observed that at the two lowest temperatures (RT and 363 K) the signal amplitude during collection is not constant, but increases with time. At higher temperatures, signal form corrects to a flat-top profile. This is indicated in the Figure 5.14, where, for clarity, only two hole-induced TCT traces are plotted again.
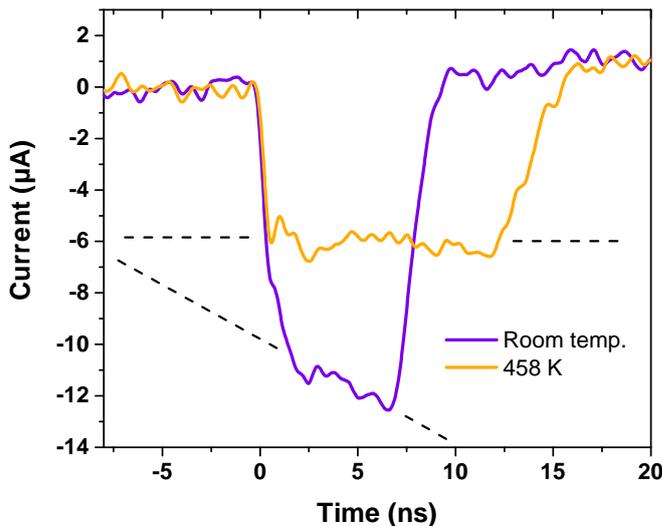
Figure 5.14: Two, selected, transient current signals, induced by hole drift at RT and elevated temperature of 458 K. Pulse shape for two signals behaves differently, indicating linearly changing electric field in detector at RT, which evolves to constant field profile at elevated temperature.

Following the conclusions from the work of Pernegger et al. [15], this trend can be attributed to the effects of volume polarization, that is build-up of space charge, trapped uniformly throughout the detector bulk.

Let us see how the model of a volume polarization explains the observed TCT behavior for holes. This model is shown schematically in Figure 5.15 - the polarization occurs due to the accumulation of trapped positive charge in a detector volume. The process goes in the following way. Short-range radiation particles ionize the small volume under the front electrode. Electrons are immediately collected on the front electrode, while the holes drift to the back electrode and induce the response signal of the detector according to the Shockley-Ramo theory. Next, we assume that the diamond is uniformly filled with defects that act as hole capture centers. During

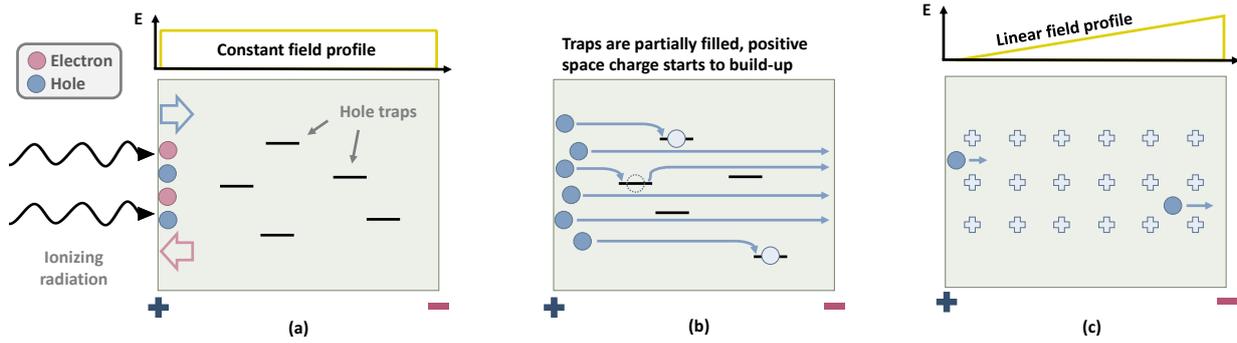**Figure 5.15:** Simplified model of polarization effect induced after ionization by short-range radiation in a plane geometry. **(a)** Radiation impinges the sample and ionizes small volume below the front electrode. Negative bias potential is brought on the back electrode, which attracts holes. Electrons are immediately collected on the positive electrode and do not contribute to the signal. Volume is filled with hole traps. **(b)** Signal is induced by hole drift, during which some holes are being trapped (and detrapped) on capture centers. As the traps are being filled, positive space charge is building-up throughout the active detector volume. **(c)** After enough irradiation time, balance of trapping/detrapping rates is established and the created space charge results in a modified electric field profile.

the carrier drift, some holes are trapped and released by these defects. After sufficient time has elapsed, during which new carriers were constantly produced by the irradiation, an equilibrium between the capture and release rates is established. A constant average number of carriers flow through the detector volume in eqilibrium conditions. However, the electric field profile, which was constant at the beginning of the irradiation, has deteriorated to a linear profile between the electrodes, as a positive space charge has built up due to the trapped holes. Therefore, the newly produced holes "sense" a lower local field near the front electrode, and as they approach the rear electrode, the field value increases. This would lead to the increasing current profile, as we have measured at room temperature and 363 K (recall: $I \sim v \sim E$).

However, at higher temperatures, the induced signal corrects to a flat-top transient behavior, indicating a change in the trapping/detrapping balance. If the trapping center responsible for the build-up of space charge is shallow (near the valence band edge, $\Delta E < 1\,\mathrm{eV}$), the detrapping rate can become very fast even at these "not so high" elevated temperatures. It is well known that boron interstitials, and boron-related defects are main hole trapping levels in CVD diamond. The boron interstitial level is located at 0.38 eV. An increased charge detrapping rate from this level could be responsible for the restoration of the electric field in the diamond bulk. If higher temperatures lead to enhanced charge carrier release, the amount of collected charge at the electrodes should increase compared to lower temperatures. However, this was not observed in the results shown in Figure 5.13, where charge collection was estimated from the integral of TCT waveforms. This is not a definitive confirmation because the signal-to-noise ratio in our TCT results was not optimal, which limits the accuracy of the charge integration values.

Therefore, we proceeded to investigate polarization effect by observing the induced charge with slow charge-sensitive electronics, where the signal-to-noise ratio is much more favorable. Here, we observed the evolution of the IBIC signal amplitude was monitored during prolonged time periods, with continuous injection of new carriers at a constant rate of about 1 kcps of short-range ions.
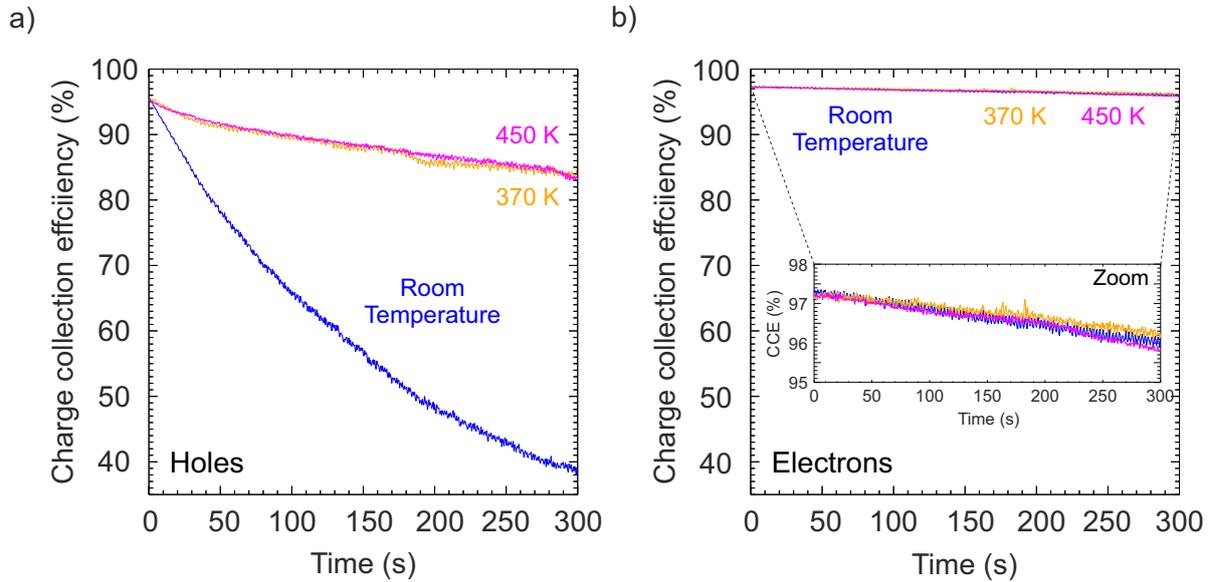

Figure 5.16: Temporal evolution of CCE in D2 detector, induced by: **(a)** hole drift, **(b)**electron drift. 3 MeV He^{2+} ion microbeam was used to ionize the detector. Charge signal was processed and analyzed using standard IBIC PHA signal processing chain. The detector was probed with 1 kcps of ions in 10 minute time period. This resulted in accumulation of 600k He ions during irradiation.

The results are shown in Figure 5.16, as a time evolution of the charge collection efficiency, for both electron and hole drift. The behavior was recorded at 3 different temperatures: RT, 370 K and 450 K. It can be seen that at all 3 temperatures the CCE for electrons decreases by only one percentage point after a period of 10 minutes. For holes, on the other hand, the signal at RT, in a same time period, drops to less than half of the original value. Interestingly, the decrease is much less pronounced at other two elevated temperatures. This supports well the previously presented explanation of the polarization effect due to the build-up of positive space charge. Since the amplitude of the charge signal amplitude is read-out by the shaping amplifier after a time much longer than the nanosecond time scale of the transient drift (the shaping time was ∼µs), the total collected signal here is more accurate compared to the TCT results. Collected charge is reduced due to trapping and consequently limited lifetime of the holes. Detrapping of holes at higher temperatures results in a larger number of holes reaching the back electrode and a higher CCE! It can be said that thermal depolarization of the positive space charge has been achieved. It is also worth noting that at RT the rate of decrease in CCE for holes weakens as the time progresses, indicating that the number of trapped charge carriers has saturated. This also

agrees well with the evolution of the polarization in our model from the Figure 5.15.

It should be noted that the applied electric field at the D2 detector during the polarization measurements was ± 0.45 V/μm (± 225 V). Rising the electric field to higher values, up to 1 V/μm affects and somewhat mitigates the temporal decrease of IBIC signal induced by the hole drift. However, the decrease remains present and occurs quickly after the start of ion probing, even at higher electric fields. Negating polarization only with change of the electric field was therefore not possible in the used experimental scenario. This can be compared to the behavior observed with the short range probing of the thin D1 detector, where negative effects of the space charge build-up were not observed even at very low electric fields (< 0.1 V/μm, therefore allowing exploration of the charge transport at various field values.

In summary, the initial analysis of TCT signals has provided many insights into the properties of charge transport during carrier drift. This technique enables the establishment of a link between signal properties resolved in the sub-nanosecond scale and effects at the microscopic level that influence charge carrier drift in a crystal lattice. From these insights the model of the polarization effect was presented and offered as a possible explanation for the trends observed from the time evolution of the hole-induced signals.

Taking a step back, a few more words need to be said about polarization in diamond radiation detectors. In a 2019 paper, Naaranoja et al. [94] modeled TCT signals in scCVD diamond, taking into account the effects of charge trapping and space charge buildup. The model was compared with TCT signals induced by alpha radiation, and good agreement was found. The main conclusions of the authors were that space charge effects cannot be associated with only one trapping center in diamond, but that multiple defects must be active. Lohstroh et al. [129] found that nitrogen related trapping affects both electron and hole transport properties. In this work, a hole trap with an activation energy of 0.29 eV was also studied and found to be responsible for the polarization effect and carrier velocity reduction. Hole trapping appears to be more prominent (or more commonly reported in the literature) for CVD diamond, when polarization effect is being studied [129, 130, 131]. Methods for depolarization are also widely reported in the literature and include bias-switching, priming (exposure to penetrating radiation to fill the traps uniformly), photon illumination, and heating [20, 82, 132, 133]. The use of thin detectors, where the charge carriers travel a shorter distance to the electrodes and therefore trapping- and polarization-related lifetime limitations become negligible, is another good strategy to combat space charge [97]. This was also demonstrated in our work, as only the thick D2 detector suffered from a significant signal degradation during hole drift. And although charge transport in the space-charge-free regime can be achieved in radiation detection with diamonds, many of the reported results suffer from the space-charge-limiting effects.

Mitigation of polarization related phenomena remains one of the key factors for across the board

improvements in diamond-based radiation detection: from crystal quality and device design to performance and new applications.

6. Influence of radiation damage on charge transport properties in diamond

6.1 Ion microscopy for radiation hardness studies

In a typical radiation hardness study, an entire semiconductor detector is exposed to damaging particles - ions, neutrons, electrons, etc. After a desired fluence is reached, the device is electrically characterized to quantify the effect of radiation damage. In order to change fluence, or other parameters related to the irradiation with damaging particles, new samples have to be used. This induces possible sample to sample variations as a variable in the study, which is not desirable, especially for CVD diamond, a relatively novel and expensive semiconductor material, where the technology of sample production by synthetic reactor growth has an impact on crystal quality that can not be completely predicted and therefore neglected.

By using the ion microprobe, we can exploit selective irradiation of small detector regions (of the order of tens of micrometers in size) to expose the same device to different fluences and/or ion energies and species.

During the irradiation campaigns used to induce radiation damage by the ion microprobe, beam current on the diamond detector was much higher ($\sim 10\,\mathrm{pA}-\sim 1\,\mathrm{nA}$) than during the IBIC probing experiments ($\sim\mathrm{fA}$ current). The main parameters that have to be determined during the exposure to damaging ion beam are: accumulated ion dose (number of ions during the irradiation time) and the irradiation area on the sample (to calculate the ion fluence).

The ion beam current and the cumulative fluence is determined with the use of the ion beam chopping system, represented in Figure 6.1.

Number of ions in a certain time window is determined from the backscattered spectra collected from the gold-plated Al sheet chopper, positioned at the entrance of the microbeam chamber. The chopper was set to periodically intercept the beam, in intervals of one second. Initially, to calibrate the chopper, the beam was terminated in the microprobe Faraday cup, where the accumulated charge was measured by the ultra-sensitive charge digitizer,(*Oxford Microbeams* model OM35e [134]). With this calibration procedure, the relation between the counts from the charge digitizer and counts from the backscattering spectra was established. Consequently, the
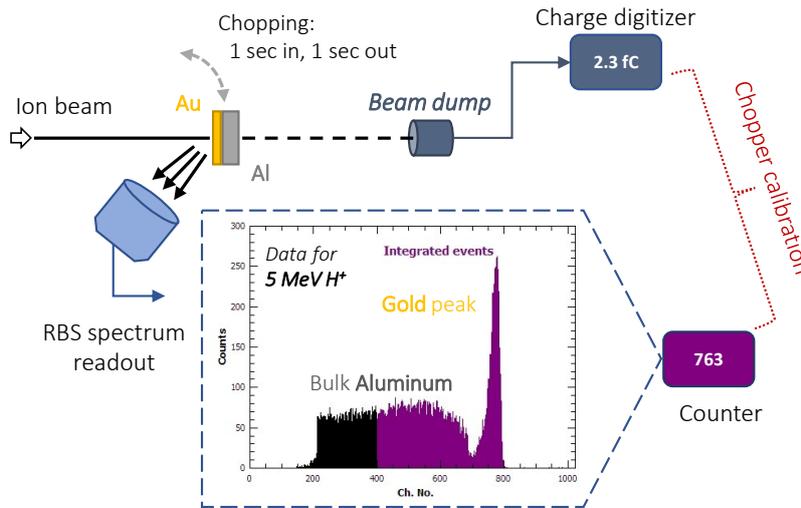
Figure 6.1: Beam chopper is positioned before the entrance to the microprobe chamber. Gold-plated aluminum sheet was used to cut the beam periodically. Backscattered ion spectrum is collected and event integral is compared to the charge read out in the Faraday cup (used as beam dump) in the chamber, obtained throughout the same time window. RBS spectrum for 5 MeV protons is displayed as an example.

total number of impinging particles during the irradiation steps were determined only from the chopper counts. The corresponding statistical uncertainty was obtained from the counts square root, which was in all cases better than 5%.

To define the ion beam irradiation area, two options can be used: 1) to focus the beam to a micrometer spot size and raster scan over the desired area, or 2) to expose the device to unfocused ion beam with well defined spatial shape. Beam spot in the second case is defined by reducing the ion beam profile physically, during the beam passage towards the vacuum chamber position. Two sets of (x,y) apertures with micropositioners were employed for this. This (second) method was used for irradiation runs in this work. It has an advantage over the focused beam setup (the first method), as there is no scanning action of the beam. During the raster scanning, local flux is moving in space-time with the beam position. On the other hand, when the beam shape is only defined by collimating action, local flux during exposure is uniform across the irradiated region. Since there is evidence* that dynamics of radiation induced defects differs during and after irradiation, local flux variation should be avoided.

6.1.1 Induction of radiation damage in a thin (D1) diamond detector

For the purposes of this work, properties of thin (D1) diamond detector were investigated after induction of radiation damage by 5 MeV protons. Both charge transport and charge collection efficiency were subsequently characterized using the IBIC probing. During the irradiation runs, detector was placed in a ion microprobe chamber together with a radiation dosimetry film

---

*As it was already mentioned (see section 3.3), intersititials in diamond appear to exist in alternative, high-mobility state during irradiation, and return to base, low-mobility state after new interstitial production is stopped.

(GAFChromic EBT-3 [135]) that promptly changes color under radiation. The film is useful, as it enables instantaneous estimate of the beam shape area in the microprobe chamber.
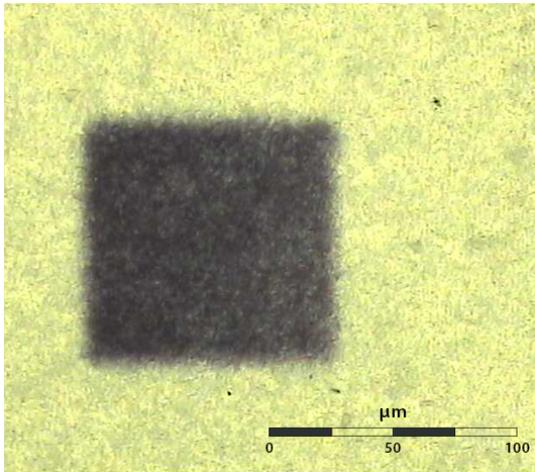

Figure 6.2: 5 MeV proton beam spot shaped in a $100 \times 100\,\mu m^2$ square area. Beam is visualized on the radiation dosimetry film placed on the sample holder in ion microbeam chamber, and viewed under microscope. The film changes color under irradiation.
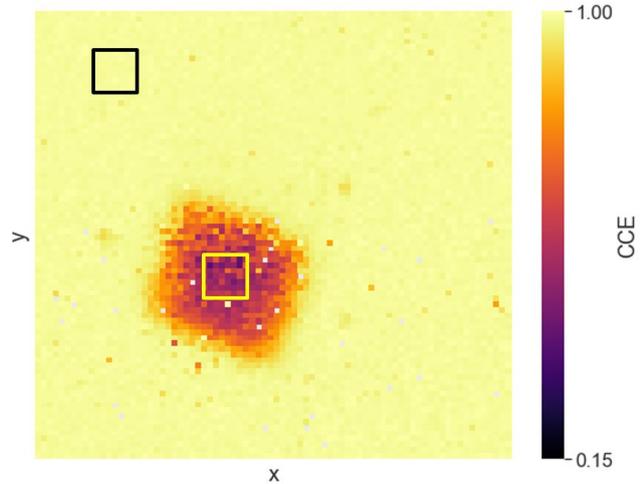

Figure 6.3: Region exposed to radiation damage is visible in IBIC map (lower CCE region), obtained by probing diamond detector with 3 MeV He$^+$ focused ions. Yellow and black squares mark the edges of regions from which data was extracted to characterize either damaged or pristine diamond signal properties.

Figure 6.2 shows the result of irradiation of a dosimetry film with 5 MeV proton beam, cut to 100×100 µm^2 area by collimating action. This size was chosen as it is small enough to cover only a minor portion of the total detector area (9 mm^2), yet large enough so that: a) the beam current remained reasonably high (smaller area = less current) and b) it is easily identified during later IBIC mapping. Detector was exposed to radiation damage in seven such regions, with varying fluences in the $10^{12} - 10^{13}\,cm^{-2}$ range. Irradiation times lasted from tens of minutes to one hour. One of these regions is displayed also in an IBIC map, plotted in Figure 6.3. The irradiation zone has lower CCE, as compared to undamaged diamond. More details on the differences between irradiation regions will be given in the following two sections.

Let us now explain why 5 MeV protons were used as damaging ions. Protons of this energy penetrate the full thickness of the detector and deposit an almost uniform profile of point defects in the crystal lattice. Vacancy profile induced by 5 MeV protons in $65\,\mu m$ thick diamond is displayed in the lower panel of Figure 6.4 (as calculated by SRIM). In the upper panel of the same figure one can see a schematic representation of charge carriers travelling through the damaged region during shallow IBIC probing (when only one type of carriers is responsible for induction of detector's response). Damaged volume can be visualized as uniformly filled with radiation induced traps, and trapping can occur during the whole travel of electrons or holes to the back electrode.

In a broader context of defect formation mechanisms, it is also important to note that MeV proton radiation is known to produce both point defects and defect clusters in semiconductor materials [136, 137]. Therefore, it is a more suitable and versatile damage-inducing particle for radiation hardness studies than neutrons, that mainly produce cluster defects; or gamma radiation, that dominantly produces point defects.
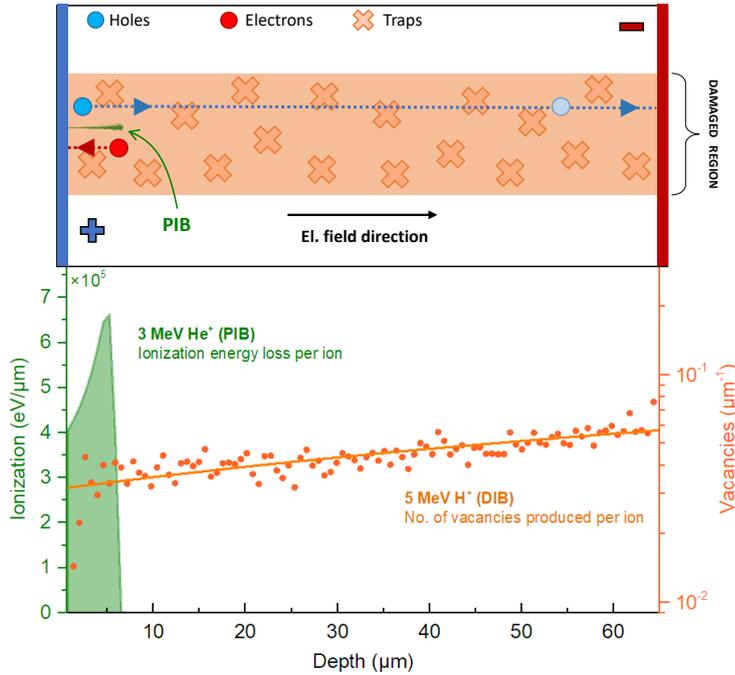

Figure 6.4: *Lower panel:* Ionization profile of 3 MeV He$^+$ ions, used as probes for inducing charge signal in the detector (Probing Ion Beam = PIB), and vacancy profile (together with linear fit - solid orange line) for 5 MeV H$^+$ ion beam used to for radiation damage introduction (Damaging Ion Beam = DIB). *Upper panel:* Schematic depiction of the detector volume exposed to radiation damage, as seen from the side, between electrodes. After irradiation with the DIB, traps are formed in the damaged region. Charge created afterwards with the PIB, can be trapped during drift in the electric field applied through electrodes.

6.2 Charge transient spectroscopy (QTS)

Parts of this section have been previously published in author's research paper in 2021. [125]

In this section, diamond detector D1 will be studied, using the QTS ion-beam technique, after it has been exposed to high fluence of 5 MeV protons.

Only one selected region of the detector was damaged, with deposited fluence of $1.5 \times 10^{13}\,\mathrm{cm}^{-2}$ and induced vacancy density $4.4 \times 10^{13}\,\mathrm{cm}^{-3}$. After the deposition of radiation damage, detector was exposed to a low current probing ion beam for the characterization using IBIC technique. IBIC mapping was first employed to localize this damaged region, which can be seen in Figure 6.3. Next, the probing ion beam was constrained to scan only either inside the central region of the damaged zone (yellow square mark on the map), or in a random pristine region (black square mark). Instead of the classical IBIC PHA, time-structure of the signal was monitored directly from the charge-sensitive preamplifier output, to distinguish signal properties between the irradiated and the pristine diamond regions. Short range 3 MeV He$^+$ ions were used for
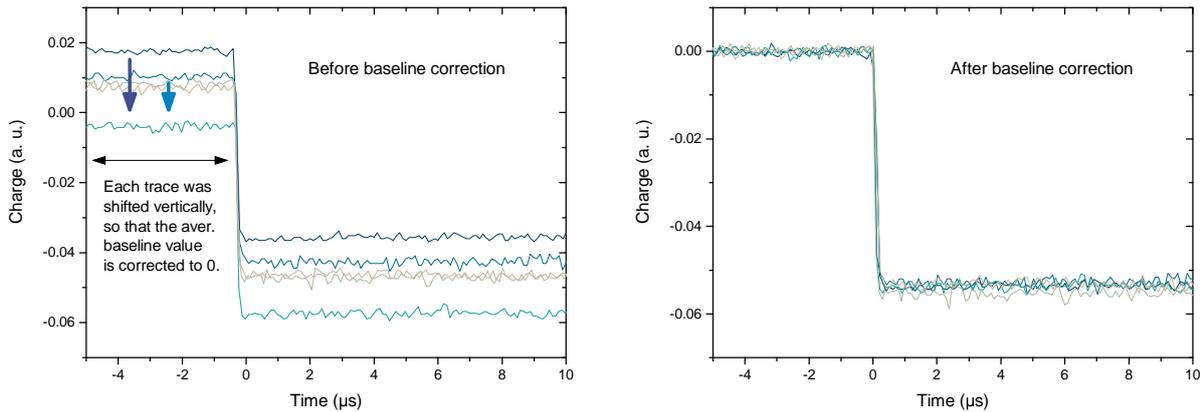
Figure 6.5: Set of five single traces induced by 3 MeV He$^+$ions, and recorded on the fast oscilloscope. Detector was kept at $150\,^\circ$C, and $-15\,$V bias was applied at the top electrode. Example is used to demonstrate baseline correction. *(Left)* Original traces are displayed before baseline correction. Due to baseline oscillations each signal is has significant offset in the vertical axis. Every trace was shifted vertically so that average value of data points before onset of the rising edge (at the $t = 0$ time point) becomes zero. *(Right)* Same traces displayed after baseline correction. These steps assure proper preparation of the dataset for averaging.

the signal probing. Ionization profile for these ions in $65\,\mu$m diamond target is displayed in the lower panel of Figure 6.4. All the charge is induced in the first $5.8\,\mu$m of depth, which is less than 10% of total the distance between detector electrodes.

6.2.1 Collection and analysis of time structure of induced charge signals

In Figure 5.3, the blue line indicates signal processing chain for the analysis of charge traces using the QTS technique which was utilized to quantify the effect of radiation damage on signal properties. CSP used in this case was Amptek CoolFET A250CF preamplifier, due to it's better signal to noise behavior as compared to ORTEC 142A CSP. More details and comparison between signals processed with these two CSPs can be found in Appendix. Signal was further sent to a fast digital oscilloscope, LeCroy WaveMaster 8500A [138] with 20 GS/s sample rate and 5 GHz bandwidth. CSP output and oscilloscope input has $50\,\Omega$ impedance. Signals were stored in an internal memory of the device and analyzed offline.

Figure 6.5 displays a set of 5 traces induced by ions. On the left side, original, unprocessed signals are displayed. Due to the baseline oscillations, signals have vertical offset. Baseline correction was preformed (as explained in the description of the same figure) to restore the average baseline value to zero. Corrected traces are displayed on the right side of the Figure 6.5. After this step, data sets containing multiple traces are prepared for averaging. Usually 20-40 traces were selected from each set, and averaged. Averaging preserved the fidelity of the original transient behavior.

6.2.2 Thermal activation of the trap - detrapping constant and energy level

Signals from the damaged and pristine diamond were directly compared in order to detect and distinguish between possible differences in charge transport influenced by the radiation damage.

It was noticed that some of the signals induced at elevated temperatures in the damaged region exhibited a slow component during the temporal evolution of the induced charge. This behavior appeared similar to the scheme shown in Figure 4.7-(b) in section 4, which can be attributed to detrapping behavior. Examples of traces induced by hole drift, with and without a slow component, are plotted in Figure 6.6. Discussion about the two types of signals shown in this plot will be given later.

The slow component in the hole transient charge signal was recorded for all temperatures above 473 K (200 °C). This would suggest that the thermal energy supplied to the holes enabled their detrapping from, for now unknown, deep capture level in the diamond. In other words, charge transient behavior enabled us to observe a thermal activation of a trapping center. It seems that this center only captures and releases holes, as there was no slow component visible in the time structure of the electron-induced charge signals in the same temperature range! However, the absolute charge amplitude induced by electron drift in the damaged region was lower than in pristine region, indicating incomplete charge collection. This can be seen in Figure 6.10 (displayed in the next section on radiation damage study). From the loss of electron signal, it can be concluded that electrons are also being trapped during drift in the damaged region, and higher temperatures are likely required to achieve thermal detrapping for this charge carrier type, which would lead to amplitude recovery.

Going back to the analysis of charge transport of holes in the region exposed to radiation damage - the next goal in the experimental process was to record the charge transients for several elevated temperatures and to extract detrapping time for each temperature. However, as mentioned earlier, not all of the hole transients exhibit delayed charge transport behavior, which has to be discussed in more detail.

Two waveforms that were selected and plotted in Figure 6.6 represent two classes of collected signals: with and without the slow component. Both types of waveforms, with and without the slow component, were present in all data sets for hole transport at various elevated temperatures. However, the signals with the slow component were dominant. The persistence of two types of transients could be due to the microscopic spatial inhomogeneity of the defect responsible for trapping within the damaged region. For example, this defect could be an aggregate of point defects induced during irradiation. During probing, the focused ion beam scans over the finite-sized central part of the damaged region. Therefore, carriers induced at nearby scanning locations drift along different trajectories, and some might not encounter the
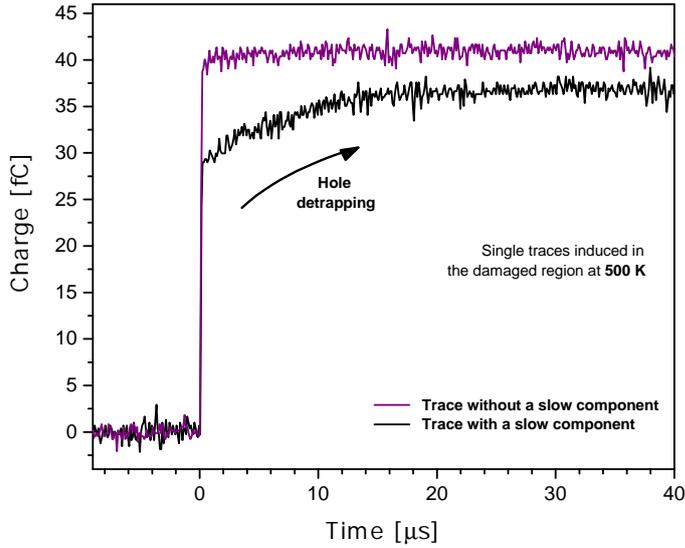
Figure 6.6: Two single transients induced by the hole drift in the radiation damaged diamond region at 500 °K. One of the signals features delayed charge transport component (slow component), while in the other one, there is no slow component. Similarly, in all datasets (for different temperatures) both types of transients were present.

defect during the drift. Alternatively, some of the probing ions might impact on the area outside the focal spot of the beam (scattered ions), and thus induce signal in the undamaged volume. However, these hypothetical scenarios cannot be confirmed, and one can only conclude that the explanation for the signals without the slow component is unclear, but they probably originate from defect-free diamond zones. For further analysis, only the waveforms containing the characteristic slow component were selected and averaged!

Interestingly, an equivalent behavior has been reported before in a work where charge traces induced by alpha source irradiation of the sc-CVD diamond detector were monitored at different temperatures [129]. Thermal activation of a trapping level was achieved, but some of the induced traces did not exhibit a slow component, which is a very similar scenario to this one.

To extract the detrapping time, we needed to model the transient behavior with the appropriate function that can be fitted to the measured data. Let's first consider the current signal response. If there are not traps in the crystal lattice, the transient current induced by the carrier drift would have a flat amplitude $I \sim const$. Now, if trapping effect is added, current signal experiences an exponential decay $I \sim \exp(-t/\tau_D)$, where τ_D is a detrapping time constant [139]. Without trapping, all charge is collected during the drift transit time window. Charge amplitude during transit time will gradually rise as the charge signal is induced at the electrodes. This component in the time structure of the charge transient will be referred to as the fast component. It can be demonstrated [128, pages: 14, 46-48] that the charge response of the detector can always be separated in two components: fast and slow. Detrapping effect is contained in

the slow component. So one can write:

$$Q(t) = \begin{cases} 0 & \text{for } t < 0 \\ \frac{Q_{\text{fast}}}{t_{tr}} \cdot t & \text{for } 0 < t < t_{tr} \\ Q_{\text{fast}} + Q_{\text{slow}} \cdot (1 - exp(-t/\tau_D)) & \text{for } t > t_{tr} \end{cases} \tag{6.1}$$

This time structure is displayed in Figure 6.7, with all relevant features of the charge signal schematic marked in the plot.
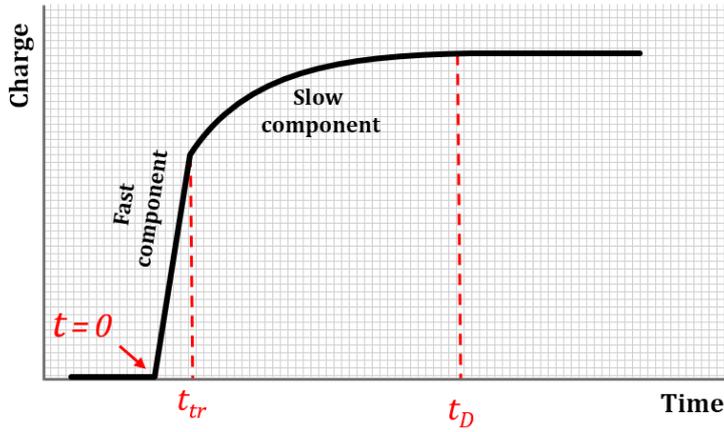

Figure 6.7: Induced transient charge pulse in diamond, displayed schematically, with fast and slow components. Fast component is active from $t = 0$ to $t = t_{\text{tr}}$ (transit time). After time t_D charge signal practically reaches amplitude value as detrapping effect is finished.

After enough time ($t \gg \tau_D$) all the carriers are detrapped and the charge amplitude has reached the constant value: $Q(t \gg \tau_D) = Q_{\text{fast}} + Q_{\text{slow}}$. By calculating the difference of $Q(t \gg \tau_D) - Q(t)$ we get:

$$Q(t \gg \tau_D) - Q(t) = Q_{\text{slow}} exp(-t/\tau_D). \tag{6.2}$$

Therefore, original transients need to be prepared in the form of the last equation, so that the exponential fit can be applied to retrieve the detrapping coefficient. Appropriate charge transients were calculated and are plotted in Figure 6.8 for temperatures from 500 K (first temperature at which detrapping was observed) to 730 K (highest temperature recorded in the experiment). Evolution of the detrapping time with temperature can be observed.

One trace is displayed in the inset of the plot, together with the fitting function according to equation 6.2. This example shows that the measured temporal evolution of the charge transient is approximated excellently by the used theoretical function. Before analysing the detrapping time, additional plot can be produced to estimate rate of change of detrapping time with temperature. Figure 6.9-(a) plots the difference in charge amplitude value at two different time points, for example at 1 μs and 10 μs (explained in the inset of the plot in Figure 6.8), at different temperatures. The plot of $\Delta Q(T)$ is sometimes referred to as a QTS spectrum. The plotted behavior exhibits a maximum of detrapping rate at around 550 K temperature. Plot-
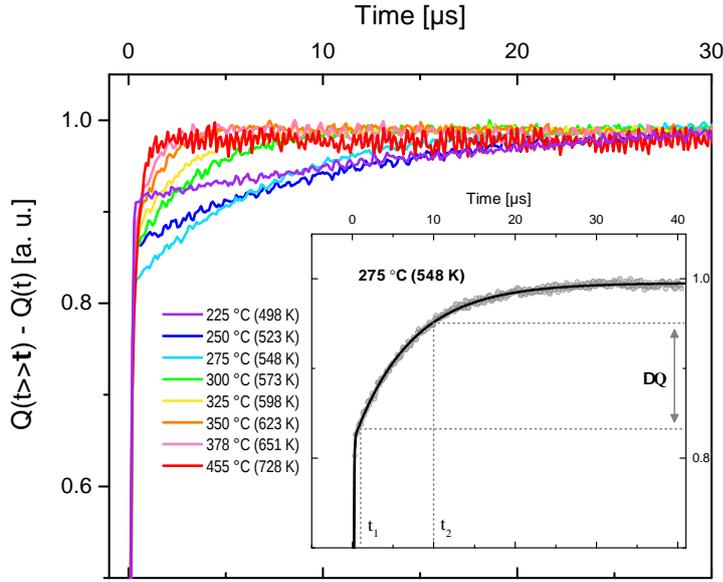
Figure 6.8: Averaged charge signals, induced by hole drift at various elevated temperatures. Signals are recorded in the diamond detector previously exposed to radiation damage. Vertical data range is normalized to a $[0, 1]$ range. Slow rise of the charge amplitude is due to the thermal activation of the trapping level in the crystal lattice. In the inset, one signal is isolated and displayed together with the fitting function according to the equation 6.2. Also, in the inset, procedure for extracting the ΔQ value is indicated, as a charge amplitude difference in the time window from t_1 to t_2.

ting QTS spectra for different time windows to analyse the peak position shift is an alternate method for extraction of detrapping time. This method has been applied before for deep levels in diamond [140, 141], and is similar to the analysis of transient capacitance response of the detector in Deep Level Transient Spectroscopy (DLTS) method. Even though in this work we have employed direct fitting of the transient to the non-linear function 6.2 to extract detrapping time constant, it is important to be considered that the underlying physics is based on the trapping-detrapping statistics which DLTS uses, so that the QTS, or Charge-DLTS (Q-DLTS) is analog to the well-established capacitance-based DLTS for analysis of parameters of deep traps in semiconductors. However, when the ion microbeam is used for irradiation and QTS analysis, probing of both irradiated and un-irradiated regions of the same sample can be made, as it was demonstrated here. This is not possible in classical DLTS, as spatially resolved probing is not available, and the whole device has to be exposed to radiation damage previous to investigation.

In section 4.3, we have derived the theoretical expression for detrapping time of a hole trap:

$$\tau_D^h = \frac{1}{T^2} \frac{\exp\left((E_t - E_v)/k_B T\right)}{\gamma_p \sigma_p}.$$ (6.3)

This equation can be rearranged for linear approximation:

$$\ln\left(\frac{1}{\tau T^2}\right) = -E_a \frac{1}{k_B T} + \ln(\gamma_p \sigma_p),$$ (6.4)

where we have substituted trap's activation energy in the expression as: $E_t - E_v = E_a$. Arrhenius plot of logarithm of $1/\tau T^2$ as a function of the $1/T$ is displayed in Figure 6.9-(b). Slope of the linear approximation yields activation energy, while the free parameter is used to calculate trap's
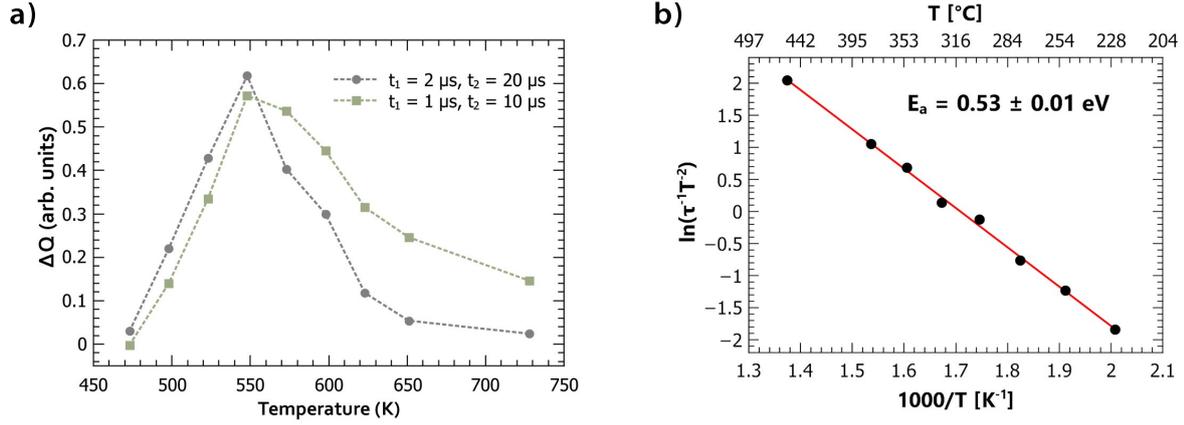
a)

b)

Figure 6.9: a) Difference of the charge pulse amplitude measured for two different time windows with the same t_2/t_1 ratio. $\Delta Q(T)$ plot is sometimes referred to as a QTS spectrum. Maximum charge difference for our measurement is observed at 550 K temperature. **b)** Arrhenius plot extracted from the temperature dependence of the detrapping time constant. Red line represents the result of the approximation according to the function 6.4. Slope of the resulting line yields $-E_a/k_B$ of the trap.

capture cross-section σ.

The results are:

$$E_a = 0.53 \pm 0.01 \, \text{eV} \tag{6.5}$$

$$\sigma = (2.42 \pm 0.05) \times 10^{-17} \, \text{cm}^2 . \tag{6.6}$$

For cross-section calculation evaluation of the factor γ_p, which depends on the hole effective mass m_h, was made:

$$\gamma_p = 3.25 \times 10^{21} (m_h/m_0) \, \left[\text{cm}^{-2} \text{s}^{-1} \text{K}^{-2} \right] . \tag{6.7}$$

Effective hole mass was assumed to be $m_h^* = 0.46 \, m_0$, which is a conductivity mass derived from the Hall measurements [2, p. 251.]. However, the exact value of hole effective mass in diamond is ambiguous. For more information, discussion, and recent experimental results, see [18]. Due to this ambiguity, cross-section value that was reported here should be taken with caution, and only as an order of magnitude indicator.

In section 4.3, expected detrapping time value for different trap levels was calculated and plotted in Figure 4.6. For a deep level with activation energy 0.5 eV, cross-section of the order of $\sigma \sim 10^{-17} \, \text{cm}^2$, and at temperature 500 K, expected detrapping time is $\tau \sim 10^{-5}$ seconds. This quick estimate agrees well with our experimental results in which a detrapping time constants were in the range of 10 µs for temperatures around 500 K, and decreased to the values of few µs at higher temperatures. This agreement indicates that the used theoretical framework, based on SRH statistics, successfully describes the observed trapping/detrapping dynamics.

The explained method was used to extract the activation energy of the deep trap, however, further identification of the actual crystalline nature of the defect can not be obtained using ion beam based techniques. The best that can be done is to compare with previously published results for deep levels in diamond with similar activation energy: 1) Thermal activation of a trap at 0.52 eV was noticed in HPHT type IIa and Ib diamond samples (unintentionally-doped) [142]. Samples differed greatly in nitrogen content, as IIa quality diamond was considered as "nitrogen-free". 2) Hole trap level at 0.53 eV was identified by Laplace-DLTS (LDLTS) and Thermal Admittance Spectroscopy (TAS) in B-doped polycrystalline CVD diamonds samples [143]. 3) Thermal activation of a deep level at 0.56 eV was noticed in leakage current analysis of a neutron irradiated sc-CVD diamond. [36, p. 111] It was attributed to the compensation of the residual boron impurity by mono-vacancies induced during radiation, due to the fact that the boron acceptor level at 0.37 eV noticed before radiation was not visible after it.

It seems that the crystalline origin of the trap cannot be determined with absolute confidence based on the previously reported results. Diamonds used in different works have different purity ratings, and only the sample used in the third work was of a similar quality to ours. There, this defect was also only noticed after introduction of radiation damage. Somewhat reasonable conclusion would be that this is a boron-related defect, whose existence is relevant to diamond based detectors exposed to high levels of radiation. Further work is needed to independently confirm the crystalline nature of the defect.

6.3 CCE performance in damaged regions

Parts of this section have been previously published in author's research paper in 2020. [122]

In the previous section, the focus was on the investigation of thermally induced release of trapped charge from defects created by the proton beam irradiation. The conducted study of the charge transport provided insight into the trapping/detrapping processes that occur at the microscopic level in the crystal lattice of diamond at elevated temperatures after exposure to radiation damage. Now the focus will be placed on the macroscopic consequences of radiation-induced defects on the performance of the detector. Namely, we will study the radiation hardness of the same diamond detector by monitoring the charge collection efficiency in the regions exposed to different fluences of a damaging 5 MeV proton beam. We again use the same type and energy of the damaging ions as in the previous section, since we have already investigated trapping/detrapping dynamics of charge transport for this irradiation type.

Let us take another look at the transient charge signals induced for the QTS investigation from the previous section. However, here we will plot together traces induced both by holes
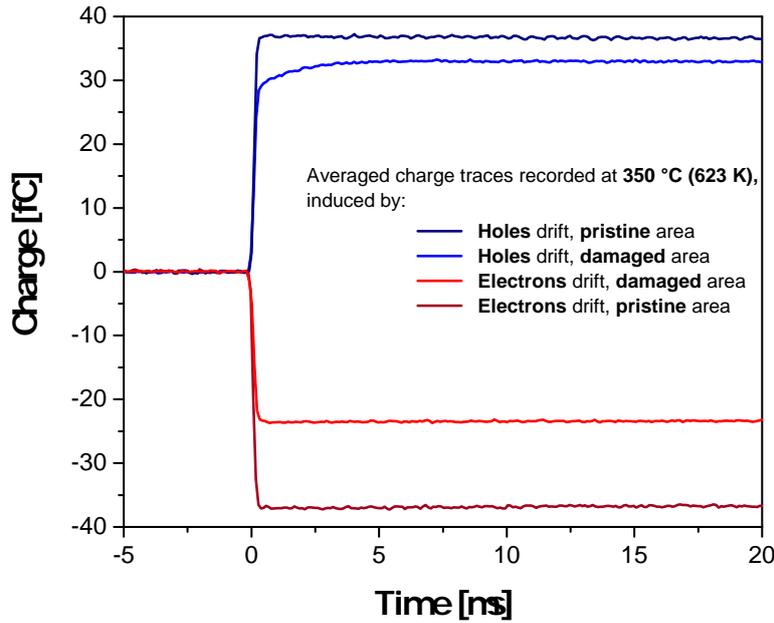
Figure 6.10: Averaged waveforms recorded at 350 °C, induced due to hole or electron drift in damaged and undamaged detector areas. Charge deficiency is observed in damaged regions for both types of charge carriers. Hole detrapping is also visible for the signal induced in the damaged region.

and electrons, either in damaged or pristine diamond regions, at a single elevated temperature of 523 K. Traces are plotted in Figure 6.10. It can be observed that the hole transient exhibits detrapping behavior, but the amplitude does not recover to the same value as in the undamaged region. The electron signal amplitude from the damaged region is also lower than the signal induced in the pristine region. Therefore, a charge deficiency is observed in signals induced by both types of charge carriers, probably due to the capture of electrons and holes by unknown defects. These defects are not thermally activated at the temperature range covered in our experiment. From this short analysis it can be concluded that radiation induced damage will impact the overall charge collection of the detector in an undetermined way that deserves more attention. To expand on the previous study, different fluences will be deposited in small detector regions to further evaluate the effects of radiation damage dose.

Irradiations were performed in two cycles, in each cycle a set of 3 regions of $100 \times 100\,\mu m^2$ size were irradiated with low, medium or high dose. Details are listed in the table 6.1.

Table 6.1: Introduction of radiation damage by ion beam in diamond detector: list of deposited fluences and corresponding vacancy densities by 5 MeV protons. SRIM was used for vacancy production estimate.

	Low damage	Medium damage	High damage	
Fluence [cm^{-2}]	8.0×10^{12}	1.1×10^{13}	2.2×10^{13}	Cycle 1
Vacancy density [cm^{-3}]	6.2×10^{13}	8.6×10^{13}	1.7×10^{14}	regions
Fluence [cm^{-2}]	3.8×10^{12}	8.3×10^{12}	1.6×10^{13}	Cycle 2
Vacancy density [cm^{-3}]	3.0×10^{13}	6.5×10^{13}	1.2×10^{14}	regions

Cycle 1 and 2 regions differ in the following way:

- After irradiation of the first set of the fluences (Cycle 1 regions), the detector was heated to 725 K. High temperature was kept for around half an hour. After this, detector was left to cool to room temperature.

- Next, similar fluences were irradiated in the second set of regions (Cycle 2 regions). No heating was performed after the irradiation step.

Such irradiation sequence was performed so that we have two sets of comparable fluences (Cycle 1 low dose matches Cycle 2 low dose, etc.). However, Cycle 1 set was annealed after irradiation, and Cycle 2 was not, which can affect defect dynamics. Low, medium and high fluence level range roughly from $10^{12}\,\mathrm{cm}^{-2}$ to $10^{13}\,\mathrm{cm}^{-2}$.

After irradiation, IBIC probing with 2 MeV protons was performed at different elevated temperatures. As it was already discussed, protons of this energy are a deep probe for $65\,\mu\mathrm{m}$ thick diamond detector - meaning that both electron and hole drift contributes to the collected charge signal. Therefore trapping of both charge carrier species will affect collection efficiency. Classical electronic chain, that is used for IBIC probing, has been explained in section 5.2. Short recapitulation is given here. Signal is processed with charge preamplifier and shaping amplifier. Amplifier outputs gaussian-like function, whose maximum corresponds to the amplitude of the preamplifier charge signal, within the shaping time window (1 µs). After this, pulse height analysis is performed by the ADC, and the signal is fed to the DAQ system integrated in software that connects the amplitude with the beam position. The software produces IBIC pulse height spectrum. Charge amplitude can be recalibrated to the units of collection efficiency (0-1) or collected energy (MeV). Since irradiation regions are created in close vicinity to each other, single IBIC scan covers all six regions, thus enabling mapping of charge amplitude for all of them simultaneously. Therefore, information for elevated temperatures was obtained in a single heating run, minimizing discrepancies in the experimental procedure. IBIC map of the regions at two selected elevated temperatures is displayed in Figure 6.11-(a),(c). Color scale signifies CCE.

Corresponding PHS extracted from the Cycle 2 regions, for these two temperatures, are plotted in Figure 6.11-(b),(d). The data for the Cycle 1 regions is not shown in the plots for visual clarity (avoiding data points cluttering), but they also exhibit gaussian-like behavior. It can be seen that the peak position shifts toward lower CCE at higher temperature. Overall, IBIC maps were collected for 16 different temperatures, ranging from RT to 725 K. All CCE data extracted from the IBIC maps are plotted in Figure 6.12 (both for damaged regions and pristine diamond). It can be seen that the CCE exhibits an overall decrease with increasing temperature for all irradiated regions.

Before a deeper analysis, it is necessary to recapitulate two facts that we have already learned from the charge transient analysis about the effects of radiation damage: 1) Thermally
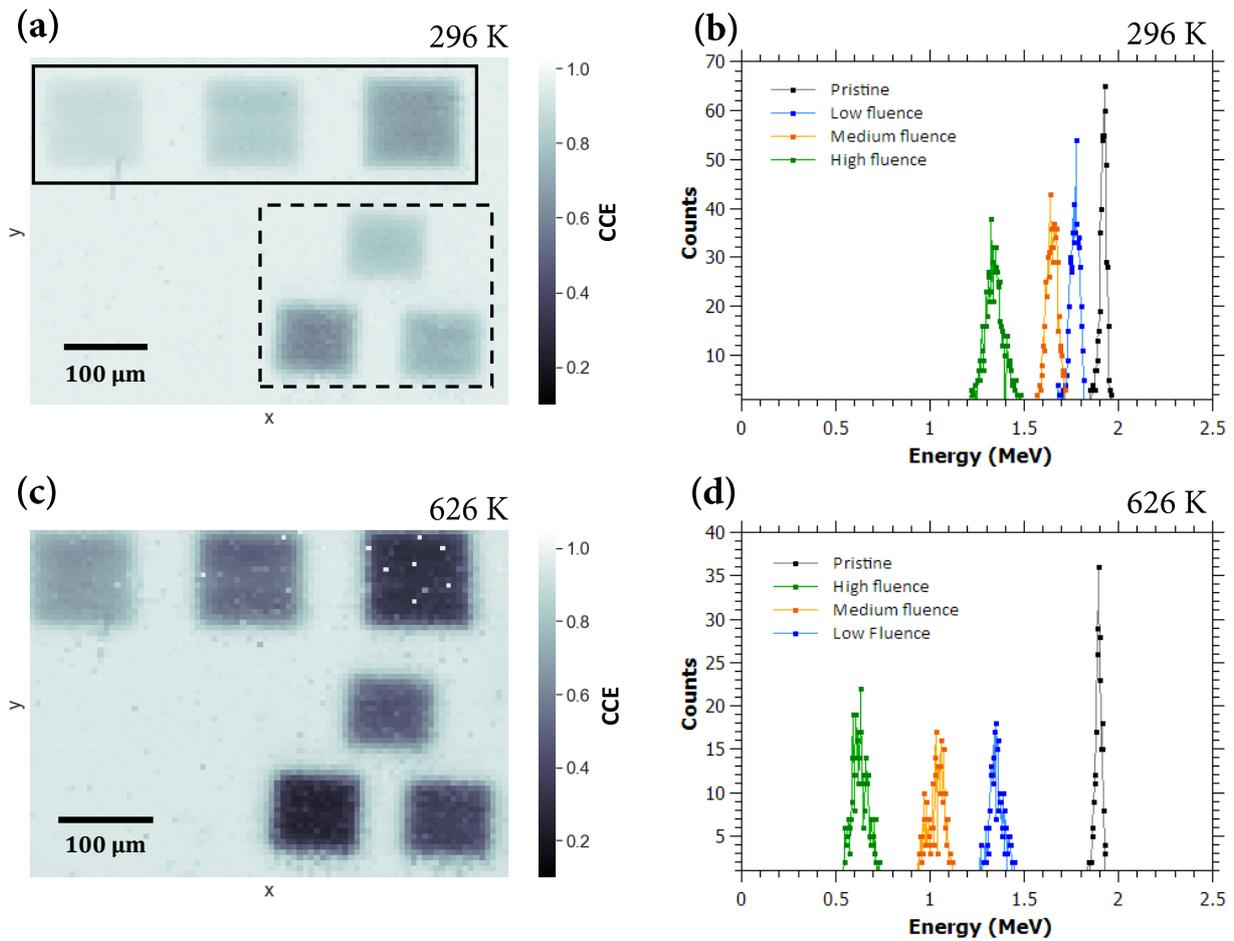
Figure 6.11: (a) IBIC map of the detector recorded at an operating temperature of 296 K. Cycle 1 regions are marked with a dashed line frame, and Cycle 2 regions are marked with a solid line frame. The applied electric field is 0.092 V/µm; **(b)** IBIC PHS obtained in the Cycle 2 damaged regions and in the pristine diamond area, recorded at 296 K (Cycle 1 regions have been omitted for clarity of the plotted data); **(c)** IBIC map recorded at 626 K; **(d)** Same IBIC PHS as in (b), recorded at 626 K. Reproduced from [122].
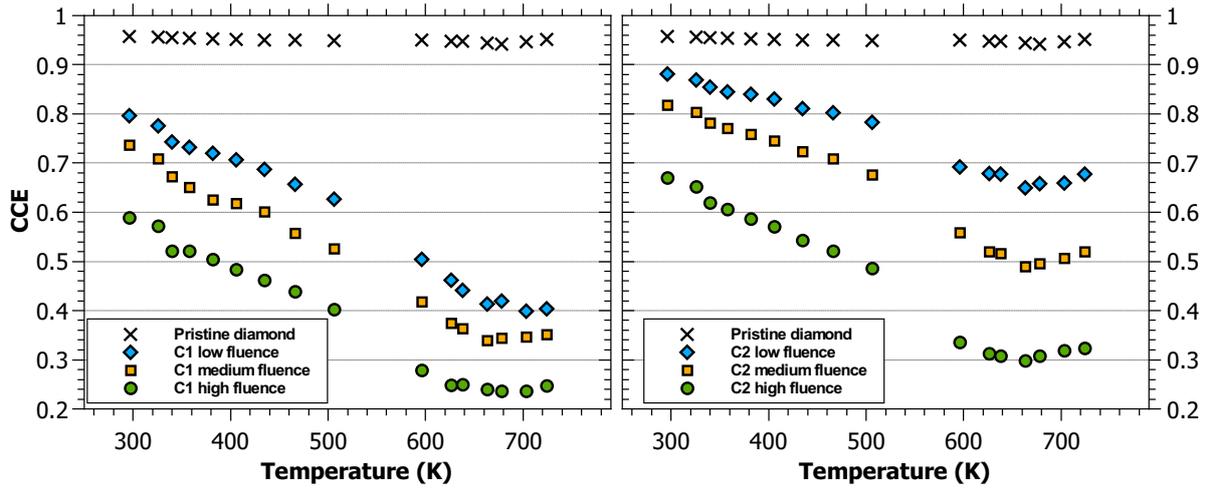
Figure 6.12: CCE as a function of temperature, obtained from IBIC probing in six regions exposed to different levels of radiation damage as well as undamaged (pristine) region of diamond detector. Results in the *left panel* are for Cycle 1 regions, in the *right panel* for Cycle 2 regions.

induced hole detrapping is active at temperatures above 500 K. This affects the amplitude of the charge signal. 2) By looking back at the time structure of the charge signal in Figure 6.10 - both hole and electron collection are affected by defects induced by radiation damage, as they are lower compared to the signals induced in the pristine region. That indicates that holes are trapped by other deep trapping levels, besides the one that was already activated, and charge is being lost due to capture on these defects. For electron induced signal, amplitude does not exhibit any detrapping recovery, and remains below the respected pristine value. Therefore, electrons are also trapped by radiation induced defects in irradiatied regions.

Going back to the analysis of CCE results: the amount of trapped charge will depend on temperature, since the mobility of electrons and holes decreases with temperature, and slower charge carriers are more likely to be captured by a trap. In other words, capture cross section increases with the temperature. Therefore, the decrease in CCE, due to this effect, is expected with rising temperature!

However, the CCE decrease appears to saturate at around 660 K, where the minimum value is reached. Above this temperature, even a small recovery of the charge amplitude is observed. This effect is probably related to the already investigated detrapping of holes from the deep level with $E_a = 0.53 \, \text{eV}$, as detrapped holes can contribute again to the collected charge. Two differences between the Cycle 1 and 2 regions can be discussed. First, the observed recovery is stronger for Cycle 2 regions. Second, at higher temperatures, the Cycle 2 regions tend to separate from the previous mutual CCE ratio, while the Cycle 1 regions retain approximately the same CCE ratio for all the temperatures. This could indicate that new defects are formed during heating (with the influence of the initial defect concentration on the progression of this process); and that the pre-annealed Cycle 1 regions are more stable as they have already undergone that

phase of lattice defect dynamics. However, this argument cannot be supported with substantial evidence in our data, but only serves to discuss the underlying defect physics.

From the IBIC results, it can be concluded that a combined influence of radiation damage and high temperatures on macroscopic detector performance is extensive and complex, as it requires a deep understanding of the interplay between charge transport and defect dynamics. The use of MeV protons as damaging and probing particles in the conducted radiation hardness study serves as an experimental scenario whose results are representative of many environments in nuclear and particle physics where detectors are exposed to elevated radiation levels. It was found that radiation induced defects significantly limit the charge transport in diamond. However, this effect does not render the detector inoperable, as the IBIC spectra collected in the damaged regions retains gaussian-like structure with well defined peak. High temperatures additionally decrease CCE, due to decreased mobility of charge carriers, and possibly other unknown mechanisms related to charge trapping; however, beneficial annealing effect was also observed, which is a promising feature, likely related to hole detrapping. This recovery of charge amplitude was not strong enough to significantly reverse and restore the CCE values, which indicates that other deep levels are still active, and electrons and holes are being trapped on them. Investigation at even higher temperatures is required to test whether charge transport would continue recovering under such conditions. Therefore, a broad conclusion about radiation tolerance of diamond in high-temperature and high-radiation environment can not be made without a more comprehensive study. Influence of radiation damage induced by different radiation types, such as various heavy ion species, neutrons or electrons, should be conducted. More importantly, based on the experience gained in this work, further experiments should attempt to achieve, and test diamond properties, at even higher temperatures, by using detectors made from thin, high quality, CVD diamond. Some research activities are already planned in this direction, aiming to extend the work presented in this thesis.

7. Conclusions

Summary

The hypothesis tested in this work was that the electronic properties of diamond, that arise from its ultra-wide band-gap, enable the use of diamond radiation detectors in harsh environments. Two detectors, prepared from single-crystal, artificially grown CVD diamonds were used, with custom-made detector housing and mounting equipment for testing under simultaneous exposure to high-temperatures and radiation in vacuum conditions. The main experimental work was performed using ion beam techniques with an ion microprobe. The employed techniques allowed the extraction of important parameters related both to the macroscopic detector performance and to the fundamental semiconductor properties of the diamond material used.

One of the goals set was to achieve as high as possible maximum operating temperature for radiation detection. In terms of energy spectroscopy, this is defined as a temperature at which the pulse-height spectrum of the induced charge signal is well-defined (resolved from the background) and can be used to identify the energy or species of the radiation particles. Using 2 MeV protons, and a 65 μm thick detector, a temperature of 725 K was achieved, with a charge collection efficiency of about 95% and an energy resolution of 2 % (40 keV). An increase in electronic noise was recorded at temperatures above 700 K, which prevented testing at even higher temperatures. This only affected the resolution and not the peak position in energy. The previous highest spectroscopic temperature achieved with diamond radiation detectors was considerably lower than the one reported here.

A significant difference in the performance of the other, thicker, 500 μm detector was observed when it was tested under similar conditions at elevated temperatures. Only a temperature of 500 K was reached before significant degradation of the signal properties, that prevented further testing. And even before that, at lower temperatures, polarization effects started to occur. Other research groups have reported similar results, with temperature systematically having a greater impact on detectors based on thicker crystals. Such behavior, where a maximum achievable temperature and diamond thickness are inversely proportional, cannot be fully explained. However, the most likely explanation is related to the unintended presence of defects, whose disadvantageous effect becomes pronounced in devices with larger separation between elec-

trodes, as this corresponds to longer drift times of electrons and holes. A more systematic study of the effect of crystal quality and detector thickness is needed to understand and mitigate space-charge-limited charge transport effects in diamond.

In this work, additional focus was placed on the investigation of the effect of temperature on polarization. In a thick (D2) crystal, hole drift was significantly affected by space-charge effects. This was initially observed through the degradation of the charge amplitude with the absorbed ion dose, which occurred due to the accumulation of positive space charge throughout the diamond bulk between the electrodes (volume polarization). This conclusion was reached from the comparison of a theoretical model with the experimentally observed evolution of transient current signals induced by hole drift. At room temperature, the current transients exhibited a shape consistent with volume polarization, while at a (relatively low) elevated temperature of 370 K, the profile corrected to a space-charge-free shape. Thermally induced detrapping of holes was identified as a probable cause.

The charge transport properties of pristine CVD diamond at high temperatures were further characterized by evaluating the mobility-lifetime product and drift time for both electrons and holes. $\mu\tau$ was extracted by fitting the Hecht equation to the measured dependence of the induced charge on the electric field in the detector. Charge was injected by short penetrating ions, to satisfy the conditions required by the Hecht approximation. It was expected that $\mu\tau$ would deteriorate with increasing temperature, which was observed only for holes and not for electrons. This is a first time that the $\mu\tau$ performance has been reported for single-crystal CVD diamond at high temperatures.

Drift time for charge carriers at elevated temperatures was obtained from transient current waveforms. The "time-of-flight" of electron and hole drift is well defined in diamond detectors with electrodes in parallel-plate geometry (ionization chamber). Effective mobility at 1 V/µm electric field was derived from drift time data, and was found to decrease from RT to 550 K. The mobility scales down with temperature due to increased scattering on phonons and impurities in the crystal lattice.

Next, a damaging dose of MeV ions was deposited in a detector to induce radiation damage and subsequently compare the charge transport in pristine and damaged diamond. Radiation damage was introduced selectively, in small areas of the diamond volume by high-fluence irradiation with 5 MeV protons, that penetrated the entire thickness of the device. The irradiated regions were sufficiently small so that they do not impact the overall performance of the detector. This was confirmed by IBIC microscopy, which provided spatially resolved information (IBIC maps) in which the pristine and irradiated regions were clearly resolved, and it was visible that the charge transport properties in pristine diamond were not affected. Probing and directly

comparing charge signal properties in irradiated and pristine regions of the same diamond detector offered a unique advantage over conventional radiation hardness studies, where different samples have to be used for comparison. Here, possible effects coming due to differences in sample were avoided.

Charge transport in damaged regions was first evaluated by monitoring charge transient signals. A deep hole trapping level, positioned 0.53 eV above the valence band, was identified using thermally induced detrapping activated at temperatures above 470 K. The trap was not present in the pristine regions, and it did not capture electrons. Detrapping time constant was extracted from transient charge signals induced at different elevated temperatures. Energy level and capture cross-section of a trap were calculated from the temperature dependence of detrapping time, with the use of Shockley-Read-Hall theory. The used technique, referred to as Q-DLTS (charge-DLTS) is comparable to classical DLTS, which is widely used for deep level identification in semiconductors. However, it offers an advantageous possibility of spatially resolved information when used in conjunction with an ion microbeam setup, like in this experiment.

Finally, the influence of ion dose was estimated using standard analysis of IBIC pulse-height spectrum. Irradiation was performed in two cycles, where in each cycle, 3 regions were irradiated with different ion fluences. After irradiation, only one group of regions was annealed, and the other was not. This can be understand as pre-annealing, as the detector is exposed to heat again during IBIC probing, where the CCE value was extracted from all the regions at various temperatures, up to 725 K. At each temperature, a region exposed to higher damaging radiation exhibits a lower collection efficiency, which was expected. The CCE exhibited an overall decrease with increasing temperature for all irradiated regions, with the rate of decrease for the Cycle 1 regions being somewhat higher than that for the Cycle 2 regions. Saturation of the charge collection decrease was reached at around 660 K, after which even small recovery of signal amplitude was observed. The results were not completely comparable for two cycles, indicating that pre-annealing plays a role. Recovery trend was associated to the already discussed hole detrapping effect. Altogether, our study suggests that the radiation hardness of diamond detectors deteriorates at elevated temperatures, due to radiation damage induced by MeV protons. Promising charge transport recovery indicates good prospect for operation at even higher temperatures. These findings could be relevant for future studies of diamond detectors performance in both high-radiation and high-temperature conditions.

Outlook

Ion microprobe has been demonstrated as a very powerful tool for investigation of charge transport properties in semiconductor detectors. After charge injection with probing ions, a well

defined geometry of the ionization process and the drift path of the charge carriers, enabled us to extract useful information about the dynamics of charge drift and trapping both at nanosecond and microsecond time scales. Still, some of the recorded effects could not be fully explained or accounted for using the available data. Specifically, after induction of radiation damage, charge transport deteriorated due to trapping on created defects. Thermally stimulated detrapping was used to pinpoint the responsible trapping level. However, the induced signal did not recover fully after charge release was achieved, indicating that other (deeper) levels were also created, and continued to limit the charge collection. These defects are probably activated at higher temperatures, so an investigation in trapping/detrapping dynamics at even more elevated temperatures is desirable to support further conclusions in this direction.

Another important outlook is the need for a better understanding of the constraints that crystal quality and diamond geometry (especially thickness) pose on the properties of charge transport at elevated temperatures. It is expected that thin diamond detectors, fabricated from high purity CVD material, should exceed the limits reported in this work. Producing and testing such devices could be the next crucial step in understanding the true limits of diamond electronic performance under high-radiation and high-temperature conditions.

Presented work is hoped to have broadened a knowledge base on diamond as an electronic material, which in turn will inspire and enable new experiments and applications.

Additional notes

Noise performance for *ORTEC 142A* and *Amptek A250CF*

Two charge-sensitive preamplifiers have been used for the signal processing in this work: OR-TEC 142A and Amptek A250CF CoolFET. Both devices offer fast rise time of the amplified signal, $< 10\,\mathrm{ns}$ nominally for an input capacitance $< 100\,\mathrm{pF}$ (in which the D1 and D2 detectors are positioned). To keep the noise as low as possible, A250CF has a jumper at input stage that permits switching between 3 FETs of different capacitance. Minimum noise is achieved for well matched capacitance at the input. Also, the active component of the amplifier, the FET transistor, is thermoelectrically cooled to $-50\,^{\circ}\mathrm{C}$ to further improve noise performance.
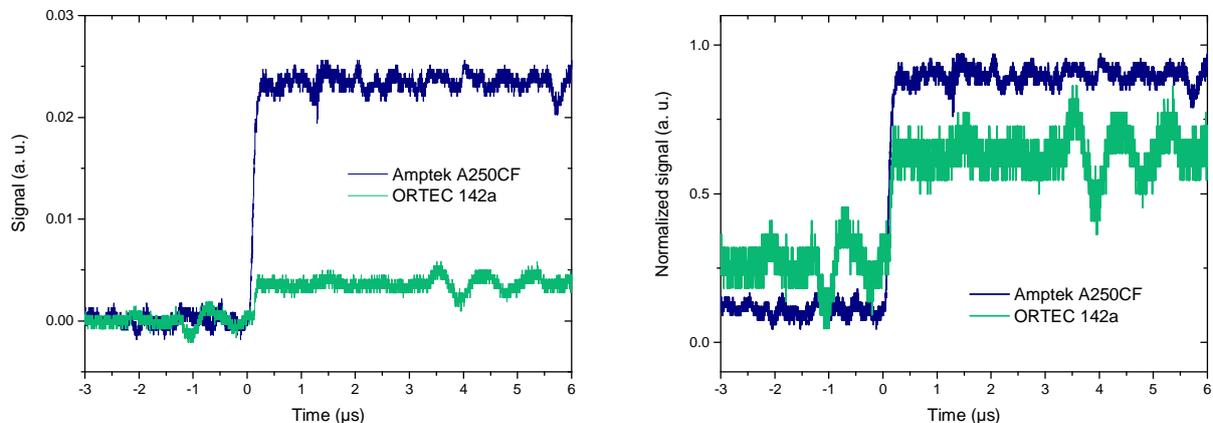
Figure 7.1: *Left panel:* Output signal of ORTEC 142A and Amptek A250CF charge-sensitive preamplifiers, recorded after induction by 2 MeV H$^+$ single ions. *Right panel:* same signals, normalized to [0,1] domain in y-axis.

Direct comparison of signal-to-noise performance for two CSPs is given in Figure 7.1, where the charge signal is recorded directly after the preamplification stage on a fast oscilloscope. Signal was induced by 2 MeV protons, and the waveforms were recorded consequently by connecting the detector to either ORTEC or CoolFET CSP, so that all other experimental conditions remain equal. Left panel of the Figure displays two single waveforms, where it can

be seen that the signal-to-noise for CoolFET is around 5 times more favorable. Right panel displays the same waveforms normalized to [0,1] amplitude interval.

The improvement of the noise sensitivity offered by CoolFET was necessary for recording charge transients in the charge transient spectroscopy (QTS) technique, where the detrapping effect in the (sub)-μs time domain was extracted from the waveforms. For a standard charge pulse-height-analysis in IBIC based measurements, ORTEC 142A was used, as it was determined that the noise performance was sufficient. Also, this preamplifier is most commonly used in signal processing for nuclear applications, so it's use represents more closely the standard conditions that can be reproduced.

Bibliography

[1] M. Pomorski et al. Development of single-crystal CVD-diamond detectors for spectroscopy and timing. *physica status solidi (a)*, 203(12):3152–3160, 2006.

[2] L. S. Pan and D. R. Kania, editors. *Diamond: Electronic Properties and Applications.* Springer US, Boston, MA, 1995.

[3] S. Koizumi et al., editors. *Power electronics device applications of diamond semiconductors.* Woodhead Publishing series in electronic and optical materials. Woodhead Publishing, Duxford [England] ; Cambridge, MA, 2018.

[4] J. M. Soler et al. The SIESTA method for *ab initio* order-*N* materials simulation. *Journal of Physics: Condensed Matter*, 14(11):2745–2779, 2002.

[5] Y. P. Varshni. Temperature dependence of the energy gap in semiconductors. *Physica*, 34(1):149–154, 1967.

[6] Butković et al. Elektronika 1 - Prvi dio. In *Elektronika 1*. FER.

[7] C. D. Clark et al. Intrinsic edge absorption in diamond. *Proceedings of the Royal Society of London. Series A. Mathematical and Physical Sciences*, 277(1370):312–329, 1964.

[8] A. Owens and A. Peacock. Compound semiconductor radiation detectors. *Nuclear Instruments and Methods in Physics Research Section A: Accelerators, Spectrometers, Detectors and Associated Equipment*, 531(1-2):18–37, 2004.

[9] C. A. Klein. Bandgap Dependence and Related Features of Radiation Ionization Energies in Semiconductors. *Journal of Applied Physics*, 39(4):2029–2038, 1968.

[10] W. Shockley. Problems related to p-n junctions in silicon. *Solid-State Electronics*, 2(1):35–67, 1961.

[11] U. Fano. Ionization Yield of Radiations. II. The Fluctuations of the Number of Ions. *Physical Review*, 72(1):26–29, 1947.

[12] T. Shimaoka et al. Fano factor evaluation of diamond detectors for alpha particles: Fano factor evaluation of diamond detectors for alpha particles. *physica status solidi (a)*, 213(10):2629–2633, 2016.

[13] F. Nava et al. Transport Properties of Natural Diamond Used as Nuclear Particle Detector for a Wide Temperatue Range. *IEEE Transactions on Nuclear Science*, 26(1):308–315, 1979.

[14] J. Kaneko et al. Radiation detector made of a diamond single crystal grown by a chemical vapor deposition method. *Nuclear Instruments and Methods in Physics Research Section A: Accelerators, Spectrometers, Detectors and Associated Equipment*, 505(1-2):187–190, 2003.

[15] H. Pernegger et al. Charge-carrier properties in synthetic single-crystal diamond measured with the transient-current technique. *Journal of Applied Physics*, 97(7):073704, 2005.

[16] R. C. Alig et al. Scattering by ionization and phonon emission in semiconductors. *Physical Review B*, 22(12):5565–5582, 1980.

[17] D. A. Neamen. *Semiconductor physics and devices: basic principles*. McGraw-Hill, New York, NY, 4th ed edition, 2012. OCLC: ocn681739179.

[18] N. Naka et al. Direct measurement via cyclotron resonance of the carrier effective masses in pristine diamond. *Physical Review B*, 88(3):035205, 2013.

[19] M. Tsubota et al. High-temperature characteristics of charge collection efficiency using single CVD diamond detectors. *Nuclear Instruments and Methods in Physics Research Section A: Accelerators, Spectrometers, Detectors and Associated Equipment*, 789:50–56, 2015.

[20] D. Tromson et al. Influence of temperature on the response of diamond radiation detectors. *Journal of Applied Physics*, 90(3):1608–1611, 2001.

[21] M. Angelone et al. Systematic study of the response of single crystal diamond neutron detectors at high temperature. *Journal of Instrumentation*, 15(03):P03031–P03031, 2020.

[22] A. V. Inyushkin et al. Thermal conductivity of high purity synthetic single crystal diamonds. *Physical Review B*, 97(14):144305, 2018.

[23] G. Slack. Nonmetallic crystals with high thermal conductivity. *Journal of Physics and Chemistry of Solids*, 34(2):321–335, 1973.

[24] L. Wei et al. Thermal conductivity of isotopically modified single crystal diamond. *Physical Review Letters*, 70(24):3764–3767, 1993.

[25] J. E. Graebner. Thermal Conductivity of Diamond. In L. S. Pan and D. R. Kania, editors, *Diamond: Electronic Properties and Applications*, pp. 285–318. Springer US, Boston, MA, 1995.

[26] F. Faili et al. Disturbed and scattered: The Path of thermal conduction through diamond lattice. In *2016 15th IEEE Intersociety Conference on Thermal and Thermomechanical Phenomena in Electronic Systems (ITherm)*, pp. 1133–1138, Las Vegas, NV, USA, 2016. IEEE.

[27] S. Kidalov and F. Shakhov. Thermal Conductivity of Diamond Composites. *Materials*, 2(4):2467–2495, 2009.

[28] E. K. Sichel et al. Heat capacity and thermal conductivity of hexagonal pyrolytic boron nitride. *Physical Review B*, 13(10):4607–4611, 1976.

[29] NSM Archive - Boron Nitride (BN) - Thermal properties: `http://www.ioffe.ru/SVA/NSM/Semicond/BN/thermal.html#Thermal%20conductivity`.

[30] G. Cassabois et al. Hexagonal boron nitride is an indirect bandgap semiconductor. *Nature Photonics*, 10(4):262–266, 2016.

[31] T. Iwasaki et al. High-Temperature Operation of Diamond Junction Field-Effect Transistors With Lateral p-n Junctions. *IEEE Electron Device Letters*, 34(9):1175–1177, 2013.

[32] D. E. Wooldridge et al. Conductivity Pulses Induced in Diamond by Alpha-Particles. *Physical Review*, 71(12):913–913, 1947.

[33] K. G. Mckay. Electron Bombardment Conductivity in Diamond. *Physical Review*, 74(11):1606–1621, 1948.

[34] G. Freeman and H. Van Der Velden. Photo-electric properties of diamond, measured with a crystal counter. *Physica*, 16(5):486–492, 1950.

[35] M. N. R. Ashfold et al. Nitrogen in diamond. *Chemical Reviews*, 120(12):5745–5794, 2020.

[36] M. Pomorski. *Electronic properties of single crystal CVD diamond and its suitability for particle detection in hadron physics experiments*. PhD thesis, 2008. Available from INIS: http://inis.iaea.org/search/search.aspx?orig_q=RN:40093695 INIS Reference Number: 40093695.

[37] H. P. BOVENKERK et al. Preparation of diamond. *Nature*, 184(4693):1094–1098, 1959.

[38] K. E. Spear et al., editors. *Synthetic diamond: emerging CVD science and technology.* The Electrochemical Society series. Wiley, New York, 1994.

[39] J. C. Angus et al. Growth of diamond seed crystals by vapor deposition. *Journal of Applied Physics*, 39(6):2915–2922, 1968.

[40] A. Chayahara et al. The effect of nitrogen addition during high-rate homoepitaxial growth of diamond by microwave plasma cvd. *Diamond and Related Materials*, 13(11-12):1954–1958, 2004.

[41] T. Chunjiu et al. Role of nitrogen additive and temperature on growth of diamond films from nanocrystalline to polycrystalline. *Journal of Nanoscience and Nanotechnology*, 10(4):2722–2730, 2010.

[42] T. Suto et al. Highly oriented diamond (111) films synthesized by pulse bias-enhanced nucleation and epitaxial grain selection on a 3C-SiC/Si (111) substrate. *Applied Physics Letters*, 110(6):062102, 2017.

[43] A. Tallaire et al. Growth of large size diamond single crystals by plasma assisted chemical vapour deposition: Recent achievements and remaining challenges. *Comptes Rendus Physique*, 14(2):169–184, 2013. Crystal growth / Croissance cristalline.

[44] H. Bethe. Zur Theorie des Durchgangs schneller Korpuskularstrahlen durch Materie. *Annalen der Physik*, 397(3):325–400, 1930.

[45] F. Bloch. Zur Bremsung rasch bewegter Teilchen beim Durchgang durch Materie. *Annalen der Physik*, 408(3):285–320, 1933.

[46] W. Reitz. Materials Analysis Using a Nuclear Microprobe M. B. H. Breese, D. N. Jamieson, and P. I. C. King. *Materials and Manufacturing Processes*, 13(1):159–160, 1998.

[47] J. Lindhard and A. H. So/rensen. Relativistic theory of stopping for heavy ions. *Physical Review A*, 53(4):2443–2456, 1996.

[48] J. F. Ziegler et al. SRIM – The stopping and range of ions in matter (2010). *Nuclear Instruments and Methods in Physics Research Section B: Beam Interactions with Materials and Atoms*, 268(11-12):1818–1823, 2010.

[49] C. Montanari and P. Dimitriou. The IAEA stopping power database, following the trends in stopping power of ions in matter. *Nuclear Instruments and Methods in Physics Research Section B: Beam Interactions with Materials and Atoms*, 408:50–55, 2017.

[50] Electronic Stopping Power - database: `https://www-nds.iaea.org/stopping/stopping_about.html`.

[51] J. F. Ziegler et al. *SRIM - the stopping and range of ions in matter*. SRIM, Chester, Maryland, 2015.

[52] S. M. Sze and K. K. Ng. *Physics of semiconductor devices*. Wiley-Interscience, Hoboken, NJ, third edition edition, 2007.

[53] R. F. Pierret. *Advanced semiconductor fundamentals*. Number v. 6 in Modular series on solid state devices. Prentice Hall, Upper Saddle River, N.J, 2nd ed edition, 2003.

[54] Z. Li and H. W. Kraner. Modeling and simulation of charge collection properties for neutron irradiated silicon detectors. *Nuclear Physics B - Proceedings Supplements*, 32:398–409, 1993.

[55] L. Reggiani et al. Hole-drift velocity in natural diamond. *Physical Review B*, 23(6):3050–3057, 1981.

[56] J. Isberg. High Carrier Mobility in Single-Crystal Plasma-Deposited Diamond. *Science*, 297(5587):1670–1672, 2002.

[57] J. Pernot et al. Electrical transport in n-type 4H silicon carbide. *Journal of Applied Physics*, 90(4):1869–1878, 2001. Publisher: American Institute of Physics.

[58] J. Pernot et al. Hall hole mobility in boron-doped homoepitaxial diamond. *Physical Review B*, 81(20):205203, 2010.

[59] W. Shockley. Currents to Conductors Induced by a Moving Point Charge. *Journal of Applied Physics*, 9(10):635–636, 1938.

[60] S. Ramo. Currents Induced by Electron Motion. *Proceedings of the IRE*, 27(9):584–585, 1939.

[61] W. Dabrowski. Transport equations and Ramo's theorem. *Progress in Quantum Electronics*, 13(3):233–266, 1989.

[62] Z. He. Review of the Shockley–Ramo theorem and its application in semiconductor gamma-ray detectors. *Nuclear Instruments and Methods in Physics Research Section A: Accelerators, Spectrometers, Detectors and Associated Equipment*, 463(1-2):250–267, 2001.

[63] W. Schottky. Halbleitertheorie der Sperrschicht. *Die Naturwissenschaften*, 26(52):843–843, 1938.

[64] W. Schottky. Zur Halbleitertheorie der Sperrschicht- und Spitzengleichrichter. *Zeitschrift fr Physik*, 113(5-6):367–414, 1939.

[65] W. Schottky. Vereinfachte und erweiterte Theorie der Randschicht-gleichrichter. *Zeitschrift fr Physik*, 118(9-10):539–592, 1942.

[66] J. Koike et al. Displacement threshold energy for type IIa diamond. *Applied Physics Letters*, 60(12):1450–1452, 1992. Publisher: American Institute of Physics.

[67] G. Lutz. *Semiconductor radiation detectors: device physics*. Springer, Berlin, 2007.

[68] J. L. Hastings et al. Vacancy aggregates in silicon. *Physical Review B*, 56(16):10215–10220, 1997. Publisher: American Physical Society.

[69] R. C. Newman. Oxygen diffusion and precipitation in Czochralski silicon. *Journal of Physics: Condensed Matter*, 12(25):R335–R365, 2000. Publisher: IOP Publishing.

[70] D. B. Holt and B. G. Yacobi. *Extended defects in semiconductors: electronic properties, device effects and structures*. Cambridge University Press, New York, 2007. OCLC: 890536995.

[71] R. S. Sussmann, editor. *CVD diamond for electronic devices and sensors*. Wiley series in materials for electronic and optoelectronic applications. J. Wiley, Chichester, U.K, 2009. OCLC: ocn241304437.

[72] J. F. Prins and T. E. Derry. Radiation defects and their annealing behaviour in ion-implanted diamonds. *Nuclear Instruments and Methods in Physics Research Section B: Beam Interactions with Materials and Atoms*, 166-167:364–373, 2000.

[73] J. Achard et al. Chemical vapour deposition diamond single crystals with nitrogen-vacancy centres: a review of material synthesis and technology for quantum sensing applications. *Journal of Physics D: Applied Physics*, 53(31):313001, 2020.

[74] D. Twitchen et al. The production and annealing stages of the self-interstitial (R2) defect in diamond. *Physica B: Condensed Matter*, 273-274:644–646, 1999.

[75] M. Newton et al. Recombination-enhanced diffusion of self-interstitial atoms and vacancy–interstitial recombination in diamond. *Diamond and Related Materials*, 11(3-6):618–622, 2002.

[76] D. C. Hunt et al. Identification of the neutral carbon 100-split interstitial in diamond. *Physical Review B*, 61(6):3863–3876, 2000.

[77] I. Kiflawi et al. Electron irradiation and the formation of vacancy–interstitial pairs in diamond. *Journal of Physics: Condensed Matter*, 19(4):046216, 2007.

[78] W. Shockley and W. T. Read. Statistics of the Recombinations of Holes and Electrons, 1952.

[79] R. N. Hall. Electron-Hole Recombination in Germanium, 1952.

[80] P.-N. Volpe et al. Extreme dielectric strength in boron doped homoepitaxial diamond. *Applied Physics Letters*, 97(22):223501, 2010.

[81] G. Perez et al. Diamond semiconductor performances in power electronics applications. *Diamond and Related Materials*, 110:108154, 2020.

[82] M. R. Ramos et al. Ion Microprobe Study of the Polarization Quenching Techniques in Single Crystal Diamond Radiation Detectors. *Materials*, 15(1):388, 2022.

[83] I. A. Zahradnik et al. scCVD Diamond Membrane based Microdosimeter for Hadron Therapy. *physica status solidi (a)*, 215(22):1800383, 2018.

[84] C. Verona et al. Toward the use of single crystal diamond based detector for ion-beam therapy microdosimetry. *Radiation Measurements*, 110:25–31, 2018.

[85] M. Angelone et al. Calibration and test of a 6LiF-diamond detector for the HCPB mock-up experiment at JET. *Fusion Engineering and Design*, 146:1755–1758, 2019.

[86] S. Kamio et al. Neutron-induced signal on the single crystal chemical vapor deposition diamond-based neutral particle analyzer. *Review of Scientific Instruments*, 91(11):113304, 2020.

[87] P. Kavrigin et al. 13C(n, α_0)10Be cross section measurement with sCVD diamond detector. *The European Physical Journal A*, 52(6):179, 2016.

[88] M. Cristinziani. Diamond prototypes for the ATLAS SLHC pixel detector. *Nuclear Instruments and Methods in Physics Research Section A: Accelerators, Spectrometers, Detectors and Associated Equipment*, 623(1):174–176, 2010.

[89] J. W. Tsung et al. Signal and noise of diamond pixel detectors at high radiation fluences. *Journal of Instrumentation*, 7(09):P09009–P09009, 2012.

[90] S. Lagomarsino et al. Radiation hardness of three-dimensional polycrystalline diamond detectors. *Applied Physics Letters*, 106(19):193509, 2015.

[91] J. Morse et al. Diamond X-ray beam-position monitoring using signal readout at the synchrotron radiofrequency. *Journal of Synchrotron Radiation*, 17(4):456–464, 2010.

[92] C. Talamonti et al. Diamond Detectors for Radiotherapy X-Ray Small Beam Dosimetry. *Frontiers in Physics*, 9:632299, 2021.

[93] M. Guthoff et al. Simulation of beam induced lattice defects of diamond detectors using FLUKA. *Nuclear Instruments and Methods in Physics Research Section A: Accelerators, Spectrometers, Detectors and Associated Equipment*, 735:223–228, 2014.

[94] T. Naaranoja et al. Space charge polarization in irradiated single crystal CVD diamond. *Diamond and Related Materials*, 96:167–175, 2019.

[95] M. Pomorski et al. Super-thin single crystal diamond membrane radiation detectors. *Applied Physics Letters*, 103(11):112106, 2013.

[96] N. Skukan et al. Charge multiplication effect in thin diamond films. *Applied Physics Letters*, 109(4):043502, 2016.

[97] N. Skukan et al. Enhanced radiation hardness and signal recovery in thin diamond detectors. *AIP Advances*, 9(2):025027, 2019.

[98] I. Bogdanović Radović. Ruđer Bošković Institute Accelerator Facility. *Nuclear Physics News*, 30(2):4–9, 2020.

[99] D. Cosic et al. Data acquisition and control system for an evolving nuclear microprobe. *Nuclear Instruments and Methods in Physics Research Section B: Beam Interactions with Materials and Atoms*, 451:122–126, 2019.

[100] M. B. H. Breese. A theory of ion beam induced charge collection. *Journal of Applied Physics*, 74(6):3789–3799, 1993.

[101] E. Vittone. Semiconductor Characterization by Scanning Ion Beam Induced Charge (IBIC) Microscopy. *ISRN Materials Science*, 2013:1–17, 2013.

[102] M. D. McCluskey and E. E. Haller. *Dopants and defects in semiconductors*. Taylor & Francis, Boca Raton, FL, 2012.

[103] K. Hecht. Zum Mechanismus des lichtelektrischen Primärstromes in isolierenden Kristallen. *Zeitschrift für Physik*, 77(3):235–245, 1932.

[104] D. K. Schroder. *Semiconductor material and device characterization*. IEEE Press ; Wiley, [Piscataway, NJ] : Hoboken, N.J, 3rd ed edition, 2006. OCLC: ocm59360243.

[105] A. F. Tasch and C. T. Sah. Recombination-generation and optical properties of gold acceptor in silicon. *Phys. Rev. B*, 1:800–809, 1970.

[106] M. B. H. Breese et al. *Materials analysis using a nuclear microprobe*. John Wiley, New York, 1996.

[107] Broadband amplifier | Micron Semiconductor Ltd: `http://www.micronsemiconductor.co.uk/diamond-alternative/#amplifer`.

[108] F. Nava et al. Electron effective masses and lattice scattering in natural diamond. *Solid State Communications*, 33(4):475–477, 1980.

[109] Y. Tanimura et al. High-temperature operation of a radiation detector made of a type IIa diamond single crystal synthesized by a HP/HT method. *Nuclear Instruments and Methods in Physics Research Section A: Accelerators, Spectrometers, Detectors and Associated Equipment*, 443(2-3):325–330, 2000.

[110] P. Steinegger et al. Diamond detectors for high-temperature transactinide chemistry experiments. *Nuclear Instruments and Methods in Physics Research Section A: Accelerators, Spectrometers, Detectors and Associated Equipment*, 850:61–67, 2017.

[111] A. Kumar et al. Prototyping and performance study of a single crystal diamond detector for operation at high temperatures. *Nuclear Instruments and Methods in Physics Research Section A: Accelerators, Spectrometers, Detectors and Associated Equipment*, 858:12–17, 2017.

[112] M. Angelone et al. High temperature response of a single crystal CVD diamond detector operated in current mode. *Nuclear Instruments and Methods in Physics Research Section A: Accelerators, Spectrometers, Detectors and Associated Equipment*, 943:162493, 2019.

[113] B. Kraus et al. Charge carrier properties of single-crystal CVD diamond up to 473 K. *Nuclear Instruments and Methods in Physics Research Section A: Accelerators, Spectrometers, Detectors and Associated Equipment*, 989:164947, 2021.

[114] M. Angelone and C. Verona. Properties of Diamond-Based Neutron Detectors Operated in Harsh Environments. *Journal of Nuclear Engineering*, 2(4):422–470, 2021.

[115] P. Muret et al. Electrically active defects in boron doped diamond homoepitaxial layers studied from deep level transient spectroscopies and other techniques: Electrically active defects in boron doped diamond homoepitaxial layers. *physica status solidi (a)*, 206(9):2016–2021, 2009.

[116] Element Six CVD diamond handbook: `https://e6cvd.com/media/wysiwyg/pdf/E6_CVD_Diamond_Handbook_A5_v10X.pdf`.

[117] M. Pomorski et al. Charge transport properties of single crystal CVD-diamond particle detectors. *Diamond and Related Materials*, 16(4-7):1066–1069, 2007.

[118] H. Pernegger. High mobility diamonds and particle detectors. *physica status solidi (a)*, 203(13):3299–3314, 2006.

[119] W. de Boer et al. Radiation hardness of diamond and silicon sensors compared. *physica status solidi (a)*, 204(9):3004–3010, 2007.

[120] M. Gabrysch et al. Electron and hole drift velocity in chemical vapor deposition diamond. *Journal of Applied Physics*, 109(6):063719, 2011.

[121] optris PI 640i: `https://www.optris.global/thermal-imager-optris-pi-640`.

[122] A. Crnjac et al. Electronic Properties of a Synthetic Single-Crystal Diamond Exposed to High Temperature and High Radiation. *Materials*, 13(11):2473, 2020.

[123] F. Bachmair. Diamond sensors for future high energy experiments. *Nuclear Instruments and Methods in Physics Research Section A: Accelerators, Spectrometers, Detectors and Associated Equipment*, 831:370–377, 2016.

[124] Alpha spectroscopy sources: `https://www.ezag.com/home/products/isotope_products/isotrak_calibration_sources/reference_sources/alpha_spectroscopy_sources/`.

[125] A. Crnjac et al. Charge transport in single crystal CVD diamond studied at high temperatures. *Journal of Physics D: Applied Physics*, 54(46):465103, 2021.

[126] E. Vittone et al. Theory of ion beam induced charge collection in detectors based on the extended Shockley–Ramo theorem. *Nuclear Instruments and Methods in Physics Research Section B: Beam Interactions with Materials and Atoms*, 161-163:446–451, 2000.

[127] M. Zanichelli et al. Charge collection in semi-insulator radiation detectors in the presence of a linear decreasing electric field. *Journal of Physics D: Applied Physics*, 46(36):365103, 2013.

[128] A. Lohstroh. *Temperature Dependent Charge Transport Studies in Polycrystalline and Single Crystal CVD Diamond Detectors.* PhD thesis, University of Surrey (United Kingdom)., Guildford, 2006.

[129] A. Lohstroh et al. Mapping of polarization and detrapping effects in synthetic single crystal chemical vapor deposited diamond by ion beam induced charge imaging. *Journal of Applied Physics*, 101(6):063711, 2007.

[130] W. Kada et al. Continuous observation of polarization effects in thin SC-CVD diamond detector designed for heavy ion microbeam measurement. *Nuclear Instruments and Methods in Physics Research Section B: Beam Interactions with Materials and Atoms*, 331:113–116, 2014.

[131] M. Ramos et al. Characterization of ion beam induced polarization in scCVD diamond detectors using a microbeam probe. *Nuclear Instruments and Methods in Physics Research Section B: Beam Interactions with Materials and Atoms*, 504:21–32, 2021.

[132] Y. Sato et al. Radiation hardness of a single crystal CVD diamond detector for MeV energy protons. *Nuclear Instruments and Methods in Physics Research Section A: Accelerators, Spectrometers, Detectors and Associated Equipment*, 784:147–150, 2015.

[133] C. Manfredotti et al. Blue light sensitization of CVD diamond detectors. *Diamond and Related Materials*, 12(3-7):662–666, 2003.

[134] OM35e - Oxford Microbeams: `http://www.microbeams.co.uk/Products.html#om35e`.

[135] EBT3 specifications and user guide: `http://www.gafchromic.com/documents/EBT3_Specifications.pdf`.

[136] M. Huhtinen. Simulation of non-ionising energy loss and defect formation in silicon. *Nuclear Instruments and Methods in Physics Research Section A: Accelerators, Spectrometers, Detectors and Associated Equipment*, 491(1-2):194–215, 2002.

[137] I. Pintilie et al. Radiation-induced point- and cluster-related defects with strong impact on damage properties of silicon detectors. *Nuclear Instruments and Methods in Physics Research Section A: Accelerators, Spectrometers, Detectors and Associated Equipment*, 611(1):52–68, 2009.

[138] WaveMaster 8500A datasheet: `https://teledynelecroy.com/japan/pdf/wm8000a_series_ds.pdf`.

[139] A. Balducci et al. Trapping-detrapping defects in single crystal diamond films grown by chemical vapor deposition. *Applied Physics Letters*, 87(22):222101, 2005.

[140] W. Kada et al. Development of diagnostic method for deep levels in semiconductors using charge induced by heavy ion microbeams. *Nuclear Instruments and Methods in*

Physics Research Section B: Beam Interactions with Materials and Atoms, 348:240–245, 2015.

[141] W. Kada et al. Investigation of electrically-active deep levels in single-crystalline diamond by particle-induced charge transient spectroscopy. *Nuclear Instruments and Methods in Physics Research Section B: Beam Interactions with Materials and Atoms*, 372:151–155, 2016.

[142] P. Ščajev et al. Nonequilibrium carrier dynamics in bulk HPHT diamond at two-photon carrier generation: Nonequilibrium carrier dynamics in bulk HPHT diamond. *physica status solidi (a)*, 208(9):2067–2072, 2011.

[143] O. S. Elsherif et al. Effect of doping on electronic states in B-doped polycrystalline CVD diamond films. *Semiconductor Science and Technology*, 27(6):065019, 2012.

Biography

Andreo Crnjac was born on July 6, 1994 in Mostar, Bosnia and Herzegovina, where he finished primary school and graduated from "Gimnazija fra Grga Martić" in 2013. In 2018, he received his Master in Physics degree from the Faculty of Science, University of Zagreb. In the same year he was employed as a research assistant at the "Laboratory for Ion Beam Interactions" of the Ruđer Bošković Institute in Zagreb and enrolled in a PhD programme under the supervision of M. Jakšić. His current research focuses on the development of ion microbeam techniques for the characterization of semiconductor detectors and on material modification by ion implantation. He is a teaching assistant at the Department of Physics within the Faculty of Science. To date, he has contributed to seven research articles, two of which as a main author.

List of published works

1. Jakšić, M., Crnjac, A., Kramberger, G., Manojlović, M., Laštovička-Medin, G. & Ramos, M. (2022) *Ion Microbeam Studies of Charge Transport in Semiconductor Radiation Detectors With Three-Dimensional Structures: An Example of LGAD.* Frontiers in Physics, 10.

2. Ramos, M., Crnjac, A., Cosic, D. & Jakšić, M. (2022) *Ion Microprobe Study of the Polarization Quenching Techniques in Single Crystal Diamond Radiation Detectors.* Materials, 15 (1), 388, 21

3. Crnjac, A., Ramos, M., Skukan, N., Pomorski, M. & Jakšić, M. (2021) *Charge transport in single crystal CVD diamond studied at high temperatures.* Journal of physics D, Applied physics, 54 (46), 465103, 9

4. Ramos, M., Crnjac, A., Provatas, G., Grilj, V., Skukan, N., Pomorski, M. & Jakšić, M. (2021) *Characterization of ion beam induced polarization in scCVD diamond detectors using a microbeam probe.* Nuclear instruments & methods in physics research. Section B, Beam interactions with materials and atoms, 504, 21-32

5. Provatas, G., Fazinić, S., Soić, N., Vukman, N., Cosic, D., Krmpotić, M., Vukšić, M., Crnjac, A., Popočovski, R., Palada, L., Čolović, P., Dell'Aquila, D., Gašparić, I., Jelavić Malenica , D., Mijatović, T. & Uroić, M. (2020) *Differential cross section measurements*

of the 9Be(3He,p)11B reaction for NRA applications. Nuclear instruments & methods in physics research. Section B, Beam interactions with materials and atoms, 472, 36-45

6. Ditalia Tchernij, S., Lühmann, T., Corte, E., Sardi, F., Picollo, F., Traina, P., Brajković, M., Crnjac, A., Pezzagna, S., Pastuović, Ž., Degiovanni, I., Moreva, E., Aprà, P., Olivero, P., Siketić, Z., Meijer, J., Genovese, M. & Forneris, J. (2020) *Fluorine-based color centers in diamond.* Scientific reports, 10, 21537, 7

7. Crnjac, A., Skukan, N., Provatas, G., Rodriguez-Ramos, M., Pomorski, M. & Jakšić, M. (2020) *Electronic Properties of a Synthetic Single-Crystal Diamond Exposed to High Temperature and High Radiation.* Materials, 13 (11), 2473, 9

8. Jakšić, M., Cosic, D., Crnjac, A., Fazinić, S., Grilj, V., Kada, W., Provatas, G., Skukan, N. & Vićentijević, M. (2019) *In situ irradiation and IBIC probing using pulsed and dual ion microbeams.* Nuclear Instruments and Methods in Physics Research Section B: Beam Interactions with Materials and Atoms, 456, 49-52